# Versatile application of iron oxide nanoparticles in environmental challenges: from trace sulfur dioxide adsorption to waste glycerol valorisation

Samuel Karki

A thesis submitted in the partial fulfillment of the requirements for the
Master for Applied Science in Chemical Engineering

Department of Chemical and Biological Engineering
Faculty of Engineering
University of Ottawa
February 2025

# Abstract

Nanomaterials and nanoparticles are now largely investigated for various applications due to their unique properties. Iron oxide nanoparticles are increasingly popular due to their non-toxicity, affordability and versatility as well as iron abundance. Their potential magnetism is a valuable property in the field of heterogeneous catalysis as it allows for an easy recovery of the catalyst. In this project, iron oxide nanoparticles were designed and synthesized using green approaches as well as more traditional coprecipitation approaches and investigated for environmental applications. The nanoparticles were used for the adsorption of trace concentration of $SO_2$ and revalorisation of waste glycerol produced from the biodiesel production.

Low concentrations of $SO_2$ are present in industrial gaseous effluents even after flue gas desulfurization. Trace $SO_2$ capture is challenging, and even low concentrations (ppm levels) of $SO_2$ can deactivate or poison catalysts used in processes aiming to revalorise the desulfurized gas. In this work, cellulose-based adsorbents modified with iron oxide nanoparticles are proposed as a solution to remove trace $SO_2$. Cellulose is selected as it is sustainable, abundant, and innocuous, has a high surface area and contains hydroxyl groups on its surface which facilitate nanoparticles deposition. The iron oxide nanoparticles were obtained from a plant-based reduction process using green tea extract. Fourier transform infrared spectroscopy (FTIR), thermogravimetric analysis (TGA), transmission electron microscopy (TEM), scanning transmission electron microscopy (STEM), scanning electron microscopy (SEM) and X-ray diffraction (XRD) were used to assess the nanoparticle deposition and characterize the adsorbents. It was observed that the deposition process was more effective on microcrystalline cellulose than on nanocrystalline cellulose. The amount of reducing agent used had an impact on the chemical speciation of the iron oxide deposited on the cellulose and the degree of particle agglomeration.

Breakthrough capture experiments were conducted at room temperature using an inlet stream containing 25 ppm $SO_2$ in argon. The impact on the adsorption capacity of the adsorbents synthesis parameters, such as the type of cellulose used, the deposition time, the iron loading on the adsorbent and the amount of reducing agent used for the deposition, were evaluated. Microcrystalline cellulose modified with iron oxide nanoparticles showed a significantly higher affinity for the $SO_2$ than modified nanocrystalline cellulose, or both types of pristine cellulose.

The optimal iron oxide nanoparticle deposition time on the microcrystalline cellulose was observed to be 72 hours. The adsorption capacity was directly related to the iron content in the

adsorbent and increased from 0.017 $mg_{SO_2}/g_{adsorbent}$ to 0.45 $mg_{SO_2}/g_{adsorbent}$ when the iron content was increased from 0.16 wt% to 2.71 wt%. The chemical speciation of the iron also had a significant impact on the adsorption with $Fe_3O_4$ nanoparticles performing the best. Future work will focus on including $CO_2$, $O_2$ and $H_2O$ in the inlet gaseous stream and performing other modification to cellulose to increase its adsorption.

Otherwise, biodiesel production has increased significantly over recent years to provide an alternative fuel. 10% w/w of glycerol is produced as a byproduct from the biodiesel production, and this has led to a saturation of the glycerol market, making it a waste material. Glycerol can however be valorized into platform chemicals through various reactions such as oxidation. We therefore propose a $Fe_3O_4$-based catalyst to perform this oxidation in both a Fenton-like system and a photocatalytic system to produce dihydroxyacetone which has a higher economical value. The $Fe_3O_4$ nanoparticles were obtained from two different methods: coprecipitation and steel revalorisation, and further compared to $FeCl_3$ catalytic system. Both were doped with Ag nanoparticles using $NaBH_4$ or green tea extract as reducing agents. The catalysts were characterized by dynamic light scattering (DLS), XRD, TEM and their band gap was measured using diffuse reflectance spectroscopy (DRS) and the Tauc method. Both types of $Fe_3O_4$ showed a nearly identical size distribution, but more nanoparticle agglomeration was observed on the revalorised $Fe_3O_4$. The Ag doping was confirmed by XRD and the bandgaps of all the doped catalysts were smaller than their non-doped counterparts.

The catalysts were compared to a traditional Fenton oxidation of glycerol and the reaction was monitored by $^1H$ NMR. Parameters such as the hydrogen peroxide to glycerol ratio, the doping, the type of $Fe_3O_4$ and the mass of catalyst were investigated. All the $Fe_3O_4$ based catalysts showed a higher dihydroxyacetone selectivity than the $FeCl_3$, but a lower conversion. Dihydroxyacetone selectivity as high as 94% was measured when using $Fe_3O_4$ nanoparticles doped with Ag by using $NaBH_4$. However, the conversions remained between 6% and 19% for the $Fe_3O_4$ catalysts. In the photocatalytic system, the intensity of the light, the pH and the temperature were investigated. Future work will focus on improving the conversion in the Fenton-like system, transitioning to only revalorisation $Fe_3O_4$ and performing more photocatalytic studies

## Keywords:

Sulfur dioxide, glycerol, $Fe_3O_4$, nanoparticles, adsorption, oxidation

# Résumé

Les nanomatériaux et les nanoparticules sont désormais largement étudiées pour diverses applications en raison de leurs propriétés uniques. Les nanoparticules d'oxyde de fer sont de plus en plus populaires en raison de leur non-toxicité, de leur prix abordable et de leur polyvalence en plus de l'abondance de fer. Leur magnétisme potentiel est une propriété attirante dans le domaine de la catalyse hétérogène, car il permet une récupération facile du catalyseur. Dans ce projet, des nanoparticules d'oxyde de fer ont été conçues et synthétisées en utilisant une approche verte et une approche plus traditionnelle de coprécipitation, puis elles ont été étudiées pour deux applications environnementales. Les nanoparticules ont été utilisées pour l'adsorption de faible concentration de $SO_2$ et la revalorisation du glycérol, un déchet généré lors de la production de biodiesel.

De faibles concentrations de $SO_2$ sont présentes dans les effluents gazeux industriels, même après le processus de désulfuration des gaz de combustion. La capture de faibles concentrations de $SO_2$ est un défi et même des concentrations minimes de $SO_2$ (niveaux de ppm) peuvent désactiver les adsorbants ou empoisonner les catalyseurs utilisés dans les processus visant à revaloriser le gaz désulfuré. Dans ce projet, des adsorbants à base de cellulose modifiée avec des nanoparticules d'oxyde de fer sont proposés comme une solution pour capturer le $SO_2$ en faible concentration. La cellulose est choisie parce qu'elle est renouvelable, abondante, non nocive, qu'elle possède une surface spécifique élevée et qu'elle contient des groupes hydroxyles à sa surface qui facilitent le dépôt de nanoparticules. Les nanoparticules d'oxyde de fer ont été obtenues à partir d'un procédé de réduction à base de plantes utilisant de l'extrait de thé vert. La spectroscopie infrarouge à transformée de Fourier (*FTIR*), l'analyse thermogravimétrique (*TGA*), la microscopie électronique à transmission (*TEM*), la microscopie électronique à transmission à balayage (*STEM*), la microscopie électronique à balayage (*SEM*) et la diffraction des rayons X (*XRD*) ont été utilisées pour évaluer le dépôt des nanoparticules et caractériser les adsorbants synthétisés. Il a été observé que le processus de dépôt était plus efficace sur la cellulose microcristalline que sur la cellulose nanocristalline. La quantité d'agent réducteur utilisée a eu un impact sur la spéciation chimique de l'oxyde de fer déposé sur la cellulose et sur le degré d'agglomération des particules.

Des expériences d'adsorption pour obtenir les courbes de percée ont été menées à température ambiante en utilisant un flux d'entrée contenant 25 ppm de $SO_2$ dans de l'argon. L'impact sur la capacité d'adsorption des paramètres de synthèse des adsorbants, tels que le type

de cellulose utilisé, le temps de déposition, la concentration de fer sur l'adsorbant et la quantité d'agent réducteur utilisée pour la déposition a été évalué. La cellulose nanocristalline n'était pas un matériau approprié pour cette application, même lorsque des nanoparticules d'oxyde de fer étaient déposées sur le support. Au contraire, la cellulose microcristalline modifiée avec des nanoparticules d'oxyde de fer a montré une affinité significativement plus élevée pour le $SO_2$ que la cellulose nanocristalline modifiée et que les types de cellulose vierge.

Le temps de déposition optimal des nanoparticules d'oxyde de fer sur la cellulose microcristalline a été évalué à 72 heures. La capacité d'adsorption était directement liée à la teneur en fer de l'adsorbant et augmentait de 0,017 $mg_{SO2}/g_{adsorbant}$ à 0,45 $mg_{SO2}/g_{adsorbant}$ lorsque la teneur en fer était augmentée de 0,16 % massique à 2,71 % massique. La spéciation chimique du fer a également eu un impact significatif sur l'adsorption, les nanoparticules $Fe_3O_4$ étant les plus performantes. Les travaux futurs porteront sur l'inclusion du $CO_2$, de l'$O_2$ et du $H_2O$ dans le flux gazeux d'entrée et sur d'autres modifications de la cellulose afin d'améliorer son adsorption.

D'autre part, la production de biodiesel a considérablement augmenté ces dernières années de répondre à la demande pour ce carburant alternatif. 10 % massique de glycérol est généré comme sous-produit de la production de biodiesel, ce qui a entraîné une saturation du marché du glycérol, le transformant en déchet. Le glycérol peut cependant être valorisé en produits chimiques de plateforme par le biais de diverses réactions telles que l'oxydation. Nous proposons un catalyseur à base de $Fe_3O_4$ pour réaliser cette oxydation à la fois dans un système de type Fenton-like et dans un système photocatalytique afin de produire de la dihydroxyacétone qui a une valeur économique plus élevée. Les nanoparticules de $Fe_3O_4$ ont été obtenues par deux méthodes différentes : la coprécipitation et la revalorisation de l'acier, puis comparées au système catalytique utilisant du $FeCl_3$. Toutes deux ont été dopées avec des nanoparticules d'Ag en utilisant du $NaBH_4$ ou un extrait de thé vert comme agents réducteurs. Les catalyseurs ont été caractérisés par diffusion dynamique de la lumière (*DLS*), par *XRD*, par *TEM* et leur bande interdite a été mesurée en utilisant la spectroscopie de réflectance diffuse (*DRS*) et la méthode de Tauc. Les deux types de $Fe_3O_4$ ont montré une distribution de taille presque identique, mais une plus grande agglomération de nanoparticules a été observée sur le $Fe_3O_4$ obtenu par revalorisation. Le dopage à l'Ag a été confirmé par *XRD* et les bandes interdites de tous les catalyseurs dopés étaient plus petites que celles de leurs homologues non dopés.

Les catalyseurs ont été comparés à une oxydation Fenton traditionnelle du glycérol et la réaction a été suivie par RMN $^{1}H$. Des paramètres tels que le rapport de peroxyde d'hydrogène/glycérol, le dopage du catalyseur, le type de $Fe_3O_4$ et la masse du catalyseur ont été étudiés. Tous les catalyseurs à base de $Fe_3O_4$ ont montré une sélectivité en dihydroxyacétone plus élevée que le $FeCl_3$, au détriment de la conversion. Une sélectivité en dihydroxyacétone atteignant 94% a été mesurée avec l'utilisation de nanoparticules de $Fe_3O_4$ dopé à l'Ag en utilisant le $NaBH_4$. Cependant, les conversions sont restées entre 6% et 19% pour les catalyseurs à base de $Fe_3O_4$. Dans le système photocatalytique, l'intensité de la lumière, le pH et la température ont été étudiés. Les travaux futurs se concentreront sur l'amélioration de la conversion dans le système de type Fenton-like, sur la transition vers l'utilisation de catalyseur à base de $Fe_3O_4$ revalorisé uniquement et sur la réalisation d'autres études dans le système photocatalytique.

## Mots clés

Dioxyde de souffre, glycérol, $Fe_3O_4$, nanoparticules, adsorption, oxydation

## Statement of Contributors or Collaborators and Co-authorship

I declare that I am the first author for all the chapters of this thesis. Prof. Clémence Fauteux-Lefebvre supervised and guided me throughout the research presented in this thesis and provided editorial comments for the written document.

**Chapter 1** is an introduction which provides a brief literature review on the topics covered in this thesis such as iron oxide nanoparticles, sulfur dioxide capture and the challenges related to the overproduction of glycerol. It concludes with a presentation of the research objectives.

**Chapter 2** presents the work conducted to develop an adsorbent for $SO_2$ capture. The total phenolic content measurements were performed with an undergraduate researcher, Carol Morcos. Adsorbents were synthesized and their capture capacity measured with the help of undergraduate (and now graduate) researcher Emma McGurk. The experimental $SO_2$ capture montage was designed and assembled by me with guidance from Prof. Clémence Fauteux-Lefebvre. Franco Ziroldo and Gérard Nina contributed to building certain portions of the montage and modifying the LabView program respectively. TEM and STEM images was taken by Dr. David Liu from McGill University. He also performed the SAED images analysis. SEM images were taken by me with guidance from Glenn Poirier. This chapter will be submitted as an article.

**Chapter 3** presents the work focused on glycerol revalorisation. This project was conducted in collaboration with Prof. Carlos Huerta-Aguilar and his research group in Tecnológico de Monterrey. They developed the method to obtain magnetite from steel shaving residues and provided insights on the doping of magnetite, especially Aranza Fernández-Mendoza who conducted a research stay in Canada. The Fenton and Fenton-like oxidation reactions were conducted with the help of an undergraduate researcher El-Bachir Touré and graduate researcher Emma McGurk. Dr. Volodymyr Semeniuchenko helped with understanding and selecting an appropriate water suppression method to perform NMR measurements. Photocatalytic reactions and their associated HPLC studies were performed by me in Tecnológico de Monterrey campus Puebla with guidance from Prof. Carlos Huerta-Aguilar. This chapter will be part of an article to be submitted.

**Chapter 4** concludes this thesis by providing the key findings and presenting future work to be carried out for both projects.

## Acknowledgements

I would like to express my deepest gratitude to my supervisor prof. Clémence Fauteux-Lefebvre who welcomed me in her group despite my chemistry background. She has guided me in my research and helped me develop as a chemical engineering. Her expertise, support, time and encouragements were crucial in the completion of this work.

I would like to sincerely thank Prof. Carlos Huerta-Aguilar for his contribution and guidance in this project and for welcoming me in his research group in Tecnológico de Monterrey campus Puebla. Thanks to Prof. Alma Cuellar and Dr. Maria Onofre Gallegos for their technical help during my research stay in Mexico. A special thanks to Shahin Rasooli who welcomed me with open arms in Puebla and was of great company during my stay.

I would like to thank all the undergraduate students who worked on these projects and whom I had the chance of supervising, Carol Morcos, El-Bachir Touré, Aranza Fernández-Mendoza and especially Emma McGurk who is now a graduate student in our group. She has contributed significantly to both projects and will be taking over as I complete this journey.

I would like to thank all my lab mates, Xinlong Chen, Joanne Woloszyn, Amanda Ineza Mugisha, Farough Agin, Alexandra Baczynska and Nicolas Strebel for their support and maintaining a positive environment in our research group. I would also like to thank Dr. Karim Muratov who taught me how to get through in a laboratory and showed me valuable experimental techniques which were crucial in conducting this research.

I would like to thank the Chemical Engineering department technical support staff members Franco Ziroldo, Gérard Nina and Patrick Pageau for their help in fixing and improving experimental montages. Thanks to Dr. Volodymyr Semeniuchenko from the uOttawa NMR facility, Glenn Poirier from the Electron Microprobe Laboaratory, Dr. Yun Liu and Dr. Neeraj Joshi from MatChar, Dr. Jeffrey Ovens from the X-ray core facility as well as Dr. David Liu from the Electron Microscopy facility in McGill.

I acknowledge the financial support from the Natural Sciences and Engineering Research Council of Canada (NSERC), the government of Ontario, the University of Ottawa and the International Experience Scholarship (EIS).

Finally, I would like to deeply thank my partner, my parents, my sister and all my friends who have supported me throughout my masters. I could not have completed this work without their continuous support.

# Table of Contents

# List of figures

# List of tables

# Abbreviations

AC – Activated carbon
ACF – Activated carbon fibers
All the compounds from intro?
ATR – Attenuated total reflectance
CNF – Cellulose nanofibers
CNT – Carbon nanotube
$CO_2$ – Carbon dioxide
CTAB - Cetyltrimethylammonium bromide
DAMO - Diaminosilane *N*-[3-(trimethoxysilyl)propyl] ethylenediamine
DHA – Dihydroxyacetone
DLS – Dynamic light scattering
DRS – Diffuse reflectance spectroscopy
EDA – Ethylenediamine
EDS – Energy dispersive X-ray spectroscopy
EPA – Environmental Protection Agency
eV – Electron volt
FA – Formic acid
$Fe_2O_3$ – Maghemite
$Fe_3O_4$ – Magnetite
FeO(OH) – Iron oxide hydroxide
FGD – Flue gas desulfurization
FTIR – Fourier transform infrared spectroscopy
g – gram
GA – Gallic acid
GAE – Gallic acid equivalents
GLAD – Glyceraldehyde
GLOA – Glycolic acid
GO – Graphene oxide
$H_2O_2$ – Hydrogen peroxide
$H_2SO_4$ – Sulfuric acid
HAADF – High-angle annular dark field
$HNO_3$ – Nitric acid
HPLC – High performance liquid chromatography
kg – kilogram
LSD – Lime spray drying
LSFO – Limestone forced oxidation
LSPR – Localised surface plasmon resonance
M – Molar (concentration unit)
$m^3$ – Cubic meter
MCC – Microcrystalline cellulose
MeCN – Acetonitrile
mg – milligram
MHz – Mega hertz
mL – Milliliter
MOF – Metal organic framework
MWNT – Mult wall nanotube
$NaBH_4$ – Sodium borohydride
NaOH – Sodium hydroxide
NCC – Nanocrystalline cellulose
nm – nanometer
NMR – Nuclear magnetic resonance
$NO_x$ – Nitrogen oxides
OD – Outer diameter
PAH – Polyaromatic hydrocarbons
PBR – Packed bed reactor
PDF card – Powder Diffraction File card
pKa – The negative base-10 logarithm of the acid dissociation constant
ppm – Parts per million
ROS – Reactive oxygen species
SAED – Selected area electron diffraction
SEM – Scanning electron microscopy
$SO_2$ – Sulfur dioxide
SPR – Surface plasmon resonance
STEM – Scanning transmission electron microscopy
SWNT – Single wall nanotube
TEM – Transmission electron microscopy
TEMPO - 2,2,6,6-Tetramethylpiperidinyloxy
TGA – Thermogravimetric analysis
$TiO_2$ – Titanium dioxide
TPC – Total phenolic content
USA – United States of America
UV – Ultraviolet
wt% – Weight percentage
XRD – X-ray diffraction
µm – Micrometer

# Chapter 1. Introduction

As the society evolves towards sustainable practices to face the global environmental crisis, major challenges must be addressed. Among those, sulfur dioxide emissions, which are significant source of acid rain and a threat to human health, is an example of an ongoing challenge. On the other hand, novel solutions could also be accompanied by new difficulties. As such, the increased production of biodiesel as an alternative fuel creates a significant waste stream, glycerol, which needs to be managed and valorised. These challenges should be addressed by proposing novel solutions, with one avenue is the development of sustainable materials. This thesis explores the synthesis of sustainable nanostructure iron oxide-based materials for application in the $SO_2$ capture and the valorization of glycerol.

## 1.1. Emergence of nanoparticles

Nanomaterials are widely developed today and have been a highly active research field across all disciplines over the last few decades and still is today [1–3]. They have allowed us to have smaller and more powerful electronic devices [4], safer food packaging [1], enhanced drug delivery, more durable vehicles [6] and highly technical fabrics [7] to name a few.

A material is classified as nanosized when at least one of its dimensions has a size ranging between 1 to 100 nm (or $10^{-9}$ meters) [8]. Due to their particularly small size, nanomaterials can behave very differently from their bulk counterpart [9] and their properties can be modified by altering their size [10]. This highly tuneable nature displays the vast potential of nanomaterials for diverse applications and explains the pronounced interest from researchers in their development. Nanoparticles may be classified according to their size, morphology, number of nano dimensions, properties or on their chemical composition [9]. Three types of nanoparticles will be briefly covered herein: carbon-based nanoparticles, metal nanoparticles and metal-oxide nanoparticles.

### 1.1.1. Carbon-based nanoparticles

Carbon-based nanomaterials have been known for several years now with Kroto et al. discovering the first $C_{60}$ fullerene in 1985 [11,12]. This was closely followed by the discovery of carbon nanotubes (CNTs) in 1991 by lijima [13]. These material's unique properties arise from

their three-dimensional structure. Carbon is unique as it can form different stable allotropes. This is possible because the carbon-carbon (C-C) bond can either be $sp^3$ or $sp^2$ hybridized, allowing for diverse combinations in the different allotropes [14]. By forming different combinations, structures such as the football shape of fullerene or the rod shape of carbon nanotubes may be achieved in materials containing exclusively carbon. Fullerenes are zero-dimensional, spherical nanostructures made of near $sp^2$ hybridized carbon [15]. Contrary to other carbon allotropes, fullerenes are soluble in organic solvents and may be modified with hydrophilic functionalities to dissolve in polar solvents, thus increasing their useability [16] notably for medical application such as drug delivery [17] and contrast enhancing agents [18]. Graphene is a single 2D layer material made of benzene rings attached together to form a sheet. Stacked sheets of graphene form graphite, which is the most stable form of carbon under normal conditions [19]. Graphene has drawn considerable attention due to its impressive thermal, mechanical and electrical properties which are a result of the significant π-conjugation between the aromatic rings forming this material [20]. CNTs are tubular structures made of single or multiple layers of graphene to yield single walled carbon nanotubes (SWNTs) or multi walled carbon nanotubes (MWNTs) [21]. This tubular structure provides outstanding mechanical strength which is combined to large surface areas and aspect ratios as well as interesting thermal and electrical conductivity [22]. Hence, CNTs have been used as structural fillers for polymer composites [23] and for electronics application [24].

### 1.1.2. Metal nanoparticles

Metal nanoparticles are another very common class of nanomaterials. Most transition metals can exist in the form of nanoparticles, although the most common are Au, Ag, Pt, Cu, Pd, Re, Zn, Ru, Ni, Co, Cd, Al and Fe [25]. Other than having high surface to volume ratios, metal nanoparticles also have unique optical properties due to strong localized surface plasmon resonance (LSPR) [26]. This phenomenon happens when incident light interacts with a nanoparticle's group of surface electrons, known as surface plasmon, and causes their oscillation to be in resonance with that of the incident light. This phenomenon can happen in the visible and the near infrared range which allows for its use in a broad range of applications. For example, the interaction between metal nanoparticles and specific molecules may produce a shift in the LSPR absorbance wavelength. This shift has been used to develop optical based sensors made of Ag and

Au nanoparticles [27]. LSPR is also used to enhance photocatalytic activity of wide band gap materials such as $TiO_2$. By introducing Au, Ag or Pt nanoparticle on $TiO_2$, Scarisoreanu et al. [28] successfully degraded methyl orange under both UV and visible light. $TiO_2$ on its own showed minimal activity under visible light due to this material's large bandgap. However, the LSPR of the different nanoparticles happened in the visible light range which provided photocatalytic activity to the modified $TiO_2$ when it was illuminated with this type of light.

### 1.1.3. Metal oxide nanoparticles

Another important class of nanomaterials are metal oxide nanoparticles. A few common examples are CuO, ZnO, $SnO_2$, $Al_2O_3$, MgO, NiO, AgO, $Fe_2O_3$, $TiO_2$, $CeO_2$, etc. Properties of each metal oxide nanoparticles differ depending on their chemical structure. A significant number are semiconductors, and this character has been utilized for their application as gas sensors. Indeed, reducing and oxidising gases interact differently with the oxygen adsorbed on the surface of the nanoparticles. This interaction slightly modifies the bandgap and thus affects the conductance in the sensing layer. This change in conductance can be related to the partial pressure of the monitored gas [29]. $SnO_2$, ZnO, CuO, $In_2O_3$ among others have been used as gas sensing metal oxides to monitor CO, $H_2$, $H_2S$, $NH_3$ and $NO_2$ [30]. Metal oxide nanoparticles have also been used in the field of catalysis, for instance in oxidation reactions as they provide high selectivity with minimal need of toxic chemicals [31]. An example is the use of CuO nanoparticles to enhance the catalytic oxidation of CO to $CO_2$ [32]. When supported on $SiO_2$-AlOOH composite nanosheets, Yan et al. [33] attributed the catalytic activity to an unsaturated coordination in $Cu^{2+}$ which allowed for CO to coordinate and be activated. An anionic vacancy on the $Cu^{2+}$ was also filled by $O_2$. The oxidation reaction could then take place between neighbouring CO and $O_2$ to produce $CO_2$.

## 1.2. Nanoparticle synthesis

Two different approaches are used to produce nanoparticles: a top-down and a bottom-up approach. The top-down approach generally relies on a mechanical pathway to break down bulk material into nanoparticles whereas the bottom-up approach relies on molecule assemblies to produce nanoparticles from a chemical reaction. From an energy point of view, the bottom-up

approach results in more energy losses, but allows for better tuneability of the generated nanoparticles [34].

### 1.2.1. Top-down approach

Top-down nanoparticle production is achieved by mechanical breaking of the bulk material to produce smaller and smaller particles eventually achieving nanomaterials. The simplest and most common technique used is from mechanical or ball milling. It consists in breaking down the bulk material in a mill by using balls of a harder material (generally steel balls) to impact the bulk material and effectively break it down until a uniform particle size is achieved [35]. In the process, the balls transfer their kinetic energy to the powder through the impact, which can cause deformation or fragmentation of the powder [36]. This energy transfer also results in a temperature increase during the process. The size of the particles is a function of multiple variables such as the ball material and their size, the milling time, the speed and the type of mill to name a few [37]. This technique is also used to form alloys (mechanical alloying) as the repeated collisions between particles can result in welding of smaller particles to form larger pieces [38]. Both mechanical milling and alloying are now well-established techniques used to produce multiple advanced materials [39].

Sputtering is another frequent technique used in the top-down approach. It consists in bombarding a target surface with high energy gaseous ions to eject particles from the material. The ejected particles can be recovered on a substrate to grow a thin film [40]. The degree at which particles are ejected depends on the target material and its crystallinity, the energy of the ions and the incident beam angle [41]. This technique is typically used for thin film deposition or chemical etching [42]. Laser ablation [43] and thermal decomposition [44] are two other techniques used in the top-down approach.

### 1.2.2. Bottom-up approach

The bottom-up approach is far more common in the context of material development and research as it allows for better control on the properties of the yielded nanoparticles. Chemical reduction is the most common and simple approach to form nanoparticles amongst all techniques. It consists in dispersing a metal precursor in a solvent, either aqueous or organic, and adding a

suitable reducing agent and stabilizing agent like a surfactant. During the process, the initial metal ions are reduced to their zero valent form which are typically insoluble. This allows for the growth of nuclei to proceed from agglomeration of the particles [45]. The nuclei are unstable assemblies which tend to keep growing, hence surfactants are used to control the nucleation process and as a result the nanoparticle size [46]. The nanoparticle suspension produced from the process is generally stable and may be used for diverse applications depending on the nature of the particles. A similar wet chemistry approach is the chemical precipitation, or coprecipitation method. This technique proceeds by dissolving metal precursors in a solution, then by modifying the solution to make the metal insoluble, such as by modifying the pH. The now insoluble material then precipitates yielding nanoparticles [47]. Modification of the reaction conditions such as the temperature or pH and use of different stabilising agents can be used to tune the properties of the nanoparticles [48].

The sol-gel technique is very common and a popular technique used at the laboratory and the industrial scale to produce metal-oxides as well as mixed metals oxide nanoparticles [49]. It consists in preparing a metal alkoxide precursor solution and hydrolysing it to form a colloidal suspension (sol). The sol then undergoes a condensation reaction to generate the gel which contains more solid particles then liquid in the form of a metal-oxygen-metal network [50]. The resulting gel can be used for different applications like membrane formation or to produce films. The complete drying of the solvent followed by heat treatment can yield solid ceramics and nanoparticles [51]. This technique is characterised by the production of high purity materials [52]. Another approach involving an increase in temperature is the hydrothermal method. In this process, a material of interest is dissolved in water and placed in a sealed autoclave. A temperature gradient is then established in the autoclave: in the higher temperature zone the material remains dissolved in water whereas in the lower temperature zone the solution becomes supersatured which forces the solute to precipitate and nucleate to form crystals [53]. The size of the nanoparticles produced from this method can be tuned by the initial concentration [54] and the nature of the solvent [54,55]. Their morphology is partially dictated by the temperature used in the process [56]. Hydrothermal synthesis can also be carried out by using supercritical water to enhance the kinetics and form smaller particles [57]. Continuous hydrothermal synthesis is also increasingly popular to increase the scalability of the process and produce more significant quantities of nanoparticles necessary for the current material applications [58].

### 1.2.3. Plant extract synthesis

The above techniques have their respective advantages and inconveniences for the nanoparticle formations. Some of which are substantial pressures, temperatures, the use of hazardous chemicals or long reaction times [59]. A novel approach which is growing in interest to overcome some of the shortcomings is the use of plant extracts to generate the nanoparticles, as this technique uses non-toxic and environmentally friendly materials [60]. The formation of the nanoparticles follows a similar mechanism as when using the chemical reduction method: ions are reduced to their zero-valence form, followed by nucleation of the particles and stabilisation to prevent further agglomeration [61]. In this case however, the phytochemicals present in plant extracts serve both as reducing agents and stabilizing agent thus allowing for better reagent economy and avoiding the use of hazardous chemicals [62]. Plant extracts contain a broad diversity of secondary metabolites such as flavonoids, alkaloids and terpenoids which have shown to be able to reduce metal ions [63,64]. The diversity of chemical structures makes it difficult to establish a precise mechanism, but it is generally agreed that polyphenols present in the extracts are the main source of reducing agents [65,66]. The phenolic groups act as electron donors in the bioreduction process to yield the zero-valent metal [67]. Subsequently, their resulting oxidised product (carbonyls), in conjunction with other functional groups present in the extracts such as amines and hydroxyls, serve as stabilizing agents preventing agglomeration [59–61][59–61][68,69]. Polyphenols are easily extracted from the plants in polar solvents such as water [70] and the use of an extract is more convenient for diverse applications. The process of forming the nanoparticles is very simple and simply consists in combining a metal precursor solution with the plant extract. Nanoparticles are usually formed in a matter of a few minutes and the process can be carried out at room temperature [60]. Of course, modification of the initial concentration, the pH and the temperatures are all parameters which can be tuned to achieve desired properties or morphologies in the nanoparticles [71,72].

Various plants and different parts of the plants such as the leaves, the roots, the flowers or the fruits have been successfully used to generate nanoparticles [73,74]. There does not seem to be a specific set of criteria to select a specific plant although one should consider a plant which is easily accessible, inexpensive and has a high concentration of polyphenols to ensure better reactivity. Tea (*Camellia sinensis*) is the second most consumed drink after water, and its availability is substantial around the globe [75]. All varieties (black, oolong, green and white) show

good antioxidant activity and have high total phenolic contents (TPC) [76]. Green tea has been reported to have the highest TPC amongst all [76–78] which can explain its important adoption for nanoparticle synthesis. Indeed, green tea extract has been vastly reported for the synthesis of Ag nanoparticles [79] which are often used for antimicrobial applications [80–82]. The as synthesized nanoparticles showed good activity against *E. Coli* [83] and *Staphylococcus aureus* [84]. ZnO nanoparticles [85,86] were also produced from green tea reduction and showed good antimicrobial activity. Highly stable and non-toxic gold nanoparticles were produced from green tea reduction and showed promising activity for diagnostic and therapeutic applications [87,88]. Fe nanoparticles were synthesized by this method and have been applied for environmental remediation such as wastewater treatment through malachite green dye degradation [89,90], nitrate removal [91] or Fenton like systems [92,93]. The nanoparticles were also used to remove metal contaminants like chromium (VI) [94] and arsenic (V) [95].

## 1.3. Sulfur dioxide capture

Fossil fuels have been the primary source of energy for the last centuries. Even with the current trend to adopt cleaner energy sources, experts still predict that after reaching a consumption peak, fossil fuels will remain an inherent part of the energy [96]. Combustion of fossil fuels liberates greenhouse gases such as $CO_2$ and pollutant gases like $NO_x$ and $SO_2$ in the atmosphere [97]. Sulfur is naturally present in the biosphere and may be emitted from natural phenomena like volcanic eruption [98]. However, anthropogenic emissions accounted for 60% of the emissions in 2018 [99]. This is because fossil fuels contain 1-2 wt% of sulfur which is released as $SO_2$ from the combustion. In the atmosphere, $SO_2$ is the primary precursor to the formation for acid rain which contains $H_2SO_4$ [100]. This contributes to lake acidification and can disturb fragile ecosystems [101]. Atmospheric $SO_2$ may also be oxidised to form aerosol and particulate matter [102] which are associated with risks of cardiovascular and respiratory mortality [103].

Strong policies have been enforced in multiple countries since 1970 to limit $SO_2$ emissions. In Canada, the *Clean Air Act* was adopted in 1971 and targeted $SO_2$ among other air pollutants. Between 1970 and 2011, $SO_2$ levels decreased by 96%, mainly due to the use of low sulfur fuels and programs limiting emissions [104]. A similar decrease of 95% was measured in the USA from 1980 to 2023 [105]. Developing countries are however still facing important $SO_2$ emission

challenges. China and India are currently the two countries with the highest $SO_2$ emissions as they are responsible for nearly 25% of the total global emissions [99]. Nevertheless, emissions in China have significantly decreased since 2013 mostly due to the implementation of high efficiency removal technology in power plants. On the other hand, emissions in India are on an upward trajectory [106] as this country relies heavily on coal to fulfil its energy demands. There seems to be a stabilisation in the emissions over recent year from implementation of environmental laws and deployment of $SO_2$ emission control technologies [107]. The most established process used for $SO_2$ removal from gaseous streams post combustion is flue gas desulfurization (FGD). Some other processes such as precombustion hydrodesulfurization and post combustion capture by adsorption or by biological methods are also used to a lesser extent [108].

### 1.3.1. Flue gas desulfurization

Flue gas desulfurizers can be divided into two main categories: the wet and the dry technology with both having various subcategories. The processes are classified as regenerable or non-regenerable based on whether the sulfur recovered in the process can be separated from the recycled absorbent or is being discarded with the absorbent [109]. The vast majority of industrial FGD rely on the wet process, and more specifically the wet limestone process as it is a cost-effective technique offering high performance [110].

In the wet flue gas desulfurization process, the $SO_2$ containing flue gas is brought into contact with a slurry containing either lime or limestone, with the latter being the more popular option due to lower costs [111]. When $SO_2$ gas dissolves in water, it forms sulphurous acid ($H_2SO_3$) from hydrolysis with water. This acid reacts nearly instantaneously with the bicarbonate base ($HCO_3^-$) coming from the limestone to produce calcium sulfite ($CaSO_3$). Most wet limestone FGD operate under forced oxidation (limestone forced oxidation, LSFO) by having air blowing in the reaction tank to fully oxidise the product to $CaSO_4$ or calcium sulfate (gypsum) [112]. The LSFO approach is preferred, as it prevents scaling in the reactor and allows for easy recovery of the saleable gypsum [113]. This technique can achieve 95% of removal efficiency, and the use of additives such as magnesium oxide can further increase this value [114]. Counter-current vertical spray towers are the conventional configuration in FGD as they maximise the mass transfer limited absorption, they are simple, resistant to corrosion, can handle large volumes and are inexpensive [115]. Lime is sometimes used instead of limestone because the latter has limited solubility in the

scrubber system compared to lime. To overcome this issue, limestone is finely ground prior to being used [116]. However, lime remains an alternative due to its higher reactivity, but this material is more expensive which limits its application [111]. Magnesium-enhanced lime is another absorbent used to achieve higher $SO_2$ removal using less absorbent due to its increased alkalinity which enhances the removal efficiency [108].

The other main process is the dry FGD, for which lime spray drying (LSD) is the most common technique used and is generally applied when low to medium sulfur coal is burned [111]. It essentially relies on the same chemical reactions as the wet limestone process meaning that lime or hydrated lime ($Ca(OH)_2$) reacts with sulfur dioxide to form calcium sulfite and calcium sulfate [117]. However, in this process the alkaline slurry is atomised and sprayed into the absorption tower. In the tower, the $SO_2$ is absorbed by the droplets and reacts with the base to form the above-mentioned products [118]. As the chemical reaction takes place, the heat from the flue gas causes an evaporation of the water from the droplets which leads to the recovery of solid desulfurization products and unreacted lime. They are recovered in electrostatic precipitators or bag filters [110]. This process is also referred to as a semi-dry process because the reaction takes place in the aqueous phase [117].

Although these technologies are well-established and widely used, they still have some drawbacks. The main disadvantage comes in the forms of the waste generated by both techniques. The wet limestone forced oxidation process could lead to the production of gypsum which can be commercialised, but to do so the material needs to meet specific quality criteria which require further processing. This is performed in certain plants but is not generalised and a large proportion of the flue gas desulfurization gypsum is disposed of in landfills [119]. The wet process also produces significant volumes of wastewater containing chlorides, arsenic, selenium, lead, mercury and other metals. Suitable treatment facilities must be implemented to prevent the release of these metals in the environment [120]. In the case of lime spray drying, the major product from the process is calcium sulfite. Only 25% or less of the generate products will oxidise to the saleable sulfate (gypsum) [117]. Therefore, the powder recovered is generally disposed of as a waste stream [110]. Finally, current commercial techniques are effective for removal of higher concentrations of $SO_2$ (up to 3.5%) [121], but struggle with the removal of trace concentrations of $SO_2$ [122]. This can be problematic in the context when further purification from other toxic gases (i.e. $NO_x$, CO) is required to meet more stringent regulations or specific applications. In fact, even low

concentrations of $SO_2$ are known to deactivate the catalysts used for these applications [123–125]. $SO_2$ can also poison catalysts used in applications aiming to capture or revalorise the $CO_2$ emitted from the combustion [126,127].

### 1.3.2. Adsorption

Adsorption has been proposed as an alternative or a complementary technique which could be used for dry regenerative flue gas desulfurization [128]. This approach is simple and can allow for removal of $SO_2$ through physical or chemical interactions with the porous sorbent [129]. The captured gas can then be desorbed to be recovered in a concentrated form and to regenerate the adsorbent, thus significantly decreasing the waste associated with the process. This technique can be applied at lower temperatures and also proves to be more effective at lower inlet concentrations of $SO_2$ which is favorable for applications were even trace amounts of $SO_2$ are detrimental [130]. The ideal adsorbents should offer high adsorption capacity, fast adsorption kinetics, good stability in the operating conditions, be regenerable and should come from renewable sources [129]. Adsorption processes for flue gas desulfurization is still low and not widely adopted in the industrial scale [108]. Research works to improve the adsorbent properties are carried out extensively and mostly focuses on activated carbon [131,132] and carbonaceous materials [133,134]. Some other materials which are currently investigated are metal organic frameworks (MOFs) [135], zeolites [136,137] and metal oxides [138,139].

#### 1.3.2.1. Activated carbon

Activated carbon (AC) are very common for purification and adsorption purposes. This is due to their high degree of porosity resulting in significant surface area, good stability, low cost and their versatility towards adsorption of various impurities [140]. They are amorphous materials which are produced from the combustion, partial combustion or thermal decomposition of carbonaceous materials [140].

When applying AC for $SO_2$ adsorption, only physical adsorption would be observed in the case where the process would take place in an inert atmosphere. However, this is not the case when dealing with flue gas as air contains oxygen. The presence of oxygen results in a chemisorption reaction in which $SO_2$ is oxidised to $SO_3$ on the surface of the AC [140,141]. Both these compounds can be removed from the surface to regenerate the adsorbent. The presence of basic functional

groups combined with small size pores of the AC was shown to enhance the adsorption capacity by Bagreev et al [142]. Indeed, the basic amine containing functional groups strengthen the physical adsorption of $SO_2$ while the smaller pores allow for a rapid reaction between co-adsorbed water and $SO_2$ molecules which form sulfuric acid. The sulfuric acid adsorption is much stronger than $SO_2$ and $SO_3$. Heat treatment prior to adsorption has shown to increase adsorption capacities as this desorbs oxygen containing functional groups which are acidic [143]. Other researchers also observed that the adsorption capacity of AC depended on the incoming $SO_2$ concentration and decreased with higher temperature [144,145].

To increase the selectivity and improve the adsorption capacity of activated carbons, various types of surface modifications have been proposed [128,146]. Generally, the increase in adsorption capacity is a result of an enhanced chemisorption of $SO_2$. By loading metals in the material, its performance can be enhanced as they can catalyse the oxidation reactions forming $SO_3$ and $H_2SO_4$. Indeed, Wang et al. [147] added cobalt, nickel, manganese, magnesium and copper on activated carbon fiber (ACF) and compared their adsorption capacities with unmodified ACF. For all modified samples there was an increase in surface area, pore volume and micropore volume. The cobalt modified ACF showed the highest activity due to a significant increase in the number of catalytic sites. Supporting iron on AC also showed to favors adsorption in a study conducted by Xiao-Li et al.[148] Indeed, catalytically active $Fe_3O_4$ species were observed on the surface for the modified AC and promoted the desulfurization by catalysing the formation of $H_2SO_4$. The adsorption capacity more than tripled when iron was loaded on AC and could be further increased by applying a nitric acid ($HNO_3$) treatment. $Fe_2(SO_4)_3$ was detected on the adsorbent after its utilisation, showing that the iron could react with the generated sulfuric acid and this pathway contributed to deactivation of the adsorbent.

#### 1.3.2.2. Cellulose

With the necessary trend for the development of sustainable materials, cellulose is gaining researcher's interest. It is the most common biopolymer in nature and its main raw material source is from wood pulp [149]. This biopolymer has a unique chemical structure consisting of repeating glucose units joined by covalent bond through an acetal functional group between the $C_1$ and $C_4$ of repeating glucopyranose units (β-1,4-glucan) [150]. Cellulose lies between classical polymers and carbohydrate as its properties are dictated by strong intermolecular interactions, chain-length

distribution and surface functional groups while being much stiffer than traditional polymers and sensible to hydrolysis and oxidation [151], giving particularly interesting properties. Hydroxyl functional groups are present on the surface of cellulose allowing for strong hydrogen bonding between chains which forms stiff fibrils. Within the fibrils, some regions of the polymer are amorphous while highly crystalline domains are also present and often desired in cellulose applications [152]. The high crystallinity produced by the hydrogen bonding network is responsible for the poor solubility of this material in water and other solvents albeit its highly polar nature [153]. The raw cellulosic material can be broken into shorter chains by acid treatment to yield microcrystalline cellulose as well as cellulose nanomaterials which have good mechanical properties, high surface area and low densities [152]. Chemical reactions with the hydroxyls to introduce carboxylic acids, esters, ethers or sulfate functional groups are also very common to extend the uses of cellulose [154,155].

There are limited reports of $SO_2$ adsorption by cellulose in the literature, although this material is a good candidate for this application. Yang et al. [156] performed an oxidation of hydroxyls on cellulose sourced from rice straw by using $KMnO_4$, followed by amine treatment. This increased the surface roughness, the presence of aldehyde and amine functional groups which all contributed to enhanced adsorption capacity. Using a simpler modification process, more recently our group compared the effect of the modifying functional group on the adsorption process by nanocrystalline cellulose (NCC). Carboxylic acid and amine modified NCC were compared, and the latter functional group contributed more significantly to the adsorption process [157]. Indeed, the adsorption capacity increased by 6 times when NCC was modified with ethylenediamine (EDA) compared to the pristine material [158].

Cellulose has been studied for other gaseous adsorption with most studies focusing on $CO_2$ adsorption [159]. On their own, cellulosic materials have shown moderate adsorption towards $CO_2$, but the adsorption capacity increased with surface modification. Amine functionalization is common for this application. Valdebenito et al. [160] observed that grafting diaminosilane *N*-[3-(trimethoxysilyl)propyl] ethylenediamine (DAMO) on cellulose nanofibers (CNF) increased the adsorption capacity of $CO_2$ due to enhanced chemisorption. $CO_2$ uptake also increased when CNF were modified with phtalimide, with dependence on the phtalimide amount, related to an increase in the number of amino and carbonyl groups on the surface. The hydroxyls can also be used to deposit metal particles on cellulose to enhance adsorption. Indeed, Campbell et al. [161] deposited

$Fe_3O_4$ and $TiO_2$ particles on cellulose which both increased the adsorption capacity from an acid-base mechanism with $CO_2$.

Various forms of cellulose are also studied as adsorbents for wastewater treatment. They have successfully been applied in the removal of metals, dyes, and both organic and inorganic ions among other materials [162]. Modification of the raw cellulose is performed to target specific contaminants and increase the adsorption capacity. For example, Fakhre & Ibrahim [163] grafted dibenzo-18-crown-6 onto cellulose for the removal of $Cd^{2+}$, $Zn^{2+}$, $Ni^{2+}$, $Pb^{2+}$ and $Cu^{2+}$ ions. They observed that the resulting composite material retained the mechanical properties of cellulose while being able to remove upwards of 90% of the incoming steam containing metals in the following preferential order: $Cd^{2+} > Pb^{2+} > Cu^{2+} > Zn^{2+} > Ni^{2+}$. D'Halluin et al. [164] used a similar approach and grafted ethylenediaminetetraacetic acid on cellulose due to its highly chelating nature. They obtained similar removal efficiencies as in the previous studies, but in this case $Ag^{1+}$, $Ni^{2+}$, $Zn^{2+}$, $Cd^{2+}$, $Pb^{2+}$, $Sn^{2+}$, and $Cu^{2+}$ were adsorbed. A simple modification with maleic anhydride allowed Zhou et al. [165] to efficiently remove $Hg^{2+}$ from an aqueous solution as well as the removal of three organic dyes: basic fuchsine, methylene blue and crystal violet. They attribute the enhancement in adsorption capacity following the modification with maleic anhydride to the more abundant -OH and -COOH functional groups which can trap ions and dyes from electrostatic interactions. They noted that the pH of the solution in which the adsorption takes place had a significant impact on the process where higher pH favored the adsorption process.

#### 1.3.2.3. Iron oxide particle for $SO_2$ capture

Among nanoparticles, iron oxides have received growing attention recently due to their highly abundant and sustainable nature, their affordability, their non-toxicity and their ease of preparation [166]. Their use has been well documented in the biomedical field. This is mainly due to the strong magnetic nature of magnetite ($Fe_3O_4$) and maghemite ($Fe_2O_3$) which makes them good contrast agents, drug delivery carriers and antimicrobial agent while being biocompatible [167]. Magnetite is composed of a mixture of $Fe^{2+}$ and $Fe^{3+}$ ions and is the transition metal oxide with the strongest magnetism. This results from its inverse spinel structure in which $Fe^{2+}$ ions are located only in the octahedral sites while the $Fe^{3+}$ ions occupied both the remaining octahedral sites and tetrahedral sites. This crystal arrangement leads to ferrimagnetic properties in the material [168]. The use of magnetite nanoparticles is expanding to various fields as iron is the second most

abundant metal on earth, making magnetite an affordable material that is non-toxic which are advantages compared to other noble metals [169]. Magnetite is used in the field of catalysis with notable examples being its industrial use as a catalyst in the Haber-Bosch process [170], in the Fischer-Tropsch synthesis [171] and in the water gas shift reaction [172].

Iron oxides have been investigated to a limited extent in the context of $SO_2$ adsorption. Pham et al. [173] produced $Fe_3O_4$ from a coprecipitation method and tested their material for adsorption of $SO_2$ and $NO_2$. They measured adsorptions of 40.5 mg/g $Fe_3O_4$ and 108.5 40.5 mg/g $Fe_3O_4$ for $SO_2$ and $NO_2$ respectively and associate this to the high porosity of the material. Ye & Ariya [174] reported that the $SO_2$ uptake on $Fe_3O_4$ particles was correlated to the number of hydroxyl groups present on the particles. These exposed O atoms could interact with the physisorbed $SO_2$ found on the Fe atoms to yield more strongly bonded chemisorbed $SO_2$. Indeed, it was observed that when oxygen is present in the $SO_2$ gaseous stream, iron oxides can oxidise $SO_2$ to $SO_3^{2-}$ and $SO_4^{2-}$ [175,176] By dispersing $Fe_3O_4$ nanoparticles on cellulose which contains an abundance of hydroxyl groups the adsorption mechanism could be enhanced from the nearby presence of O atoms.

## 1.4. Glycerol valorization

The production of glycerol has been steadily increasing over recent years as it is a byproduct in the biodiesel production and the demand for this alternative fuel is growing [177]. Unfortunately, the glycerol market is saturated from this overproduction leading to a drop in its price [178]. As such, this valuable platform chemical is often used as simple combustion material due to a lack of innovative techniques to transform this compound into valuable chemicals [179]. A potential solution would be to oxidise this compound to valuable chemicals like dihydroxyacetone or glyceraldehyde. To do so, an affordable and environmentally friendly technique which has been studied is to oxidise the glycerol using a Fenton reaction [180]. The Fenton reaction consists in combining a source of $Fe^{2+}$ with hydrogen peroxide and the target compound in water. The iron provides an excess electron to the peroxide, forming a hydroxy anion and a hydroxyl radical which is responsible for the oxidation. When Laurie & Waterhouse [180] performed this reaction, they observed that both dihydroxyacetone and glyceraldehyde were being formed which are both desired compound from this oxidation.

#### 1.4.1.1. Iron oxide nanoparticles for glycerol valorization

Iron oxide nanoparticles have also received increasing interest for heterogeneous Fenton-like reactions mostly applied for wastewater treatment as it has good redox properties, and its magnetic nature allows for easy recovery after the reaction [181]. Usman et al. [182] tested magnetite in a Fenton-like system at circumneutral pH for the degradation of polyaromatic hydrocarbons (PAH) found in soils. In a traditional Fenton system, the pH needs to be around 3 to prevent the production of ferric hydroxide sludge. However, they observed significant degradation of PAH when using magnetite at circumneutral pH whereas minimal reactivity was measured in the traditional Fenton system. This showed another advantage with magnetite as it did not require such an acidic environment and the associated chemicals.

Research is also conducted to explore magnetite as a photocatalyst for oxidation reactions. This could expand the material's applicability and further improve the green nature of the processes [183]. A photo-Fenton system was designed by Minella et al. [184] to oxidise phenol using magnetite irradiated by UVA radiation in the presence of hydrogen peroxide ($H_2O_2$). The magnetite catalysed reactions showed similar degradation performances at classical $Fe^{2+}$ salts but were also active at circumneutral pH. No reactivity was observed in the absence of irradiation. By modifying the structure of magnetite such as with the doping of other photoactive metals, the photocatalytic activity of the material can be enhanced, and the absorption range can be tuned towards visible light. This is from the presence of new energy levels near the conduction band which come from the doped metal [185]. Silver is often selected to dope photocatalysts due to its surface plasmon resonance (SPR) which promotes the absorption of light around 400nm and its intrinsic photocatalytic reactivity [186]. Magnetite-silver nanocomposites were indeed synthesized by coprecipitation by Nono et al. [187]. They applied the nanoparticles in a photo-Fenton system to degrade rhodamine B and observed that the activity of the synthesized photocatalysts increased with increasing silver content. This type of photocatalyst is a promising choice for the application of glycerol oxidation to valuable chemicals.

## 1.5. Research objectives

Based on the versatile properties of iron oxide nanoparticles, magnetite has been selected as a material of choice to study further in this thesis, to address two different challenges: trace sulfur

dioxide capture and photocatalytic oxidation of glycerol into value added chemicals. These two challenges are related by the selected material to be designed. Therefore, individual objectives were assigned to each application. However, a general aim to keep both processes as environmentally responsible as possible was applied.

### 1.5.1. $SO_2$ capture

Wet scrubbers are the workhorses in the field of desulfurization. However, there remains a need to remove trace concentrations of $SO_2$ left after this process for high purity applications or to valorise the gaseous waste stream. It's been shown by previous group members that chemical modification to cellulose can enhance the affinity of this material for $SO_2$ capture [157,158]. Building on this work, we would like to determine if we can improve this affinity by developing a green synthesis to deposit magnetite nanoparticles on the surface of cellulose and yield a sustainable, highly active adsorbent. This question is complex and different objectives covered in this thesis will help answer it:

- Efficiently prepare magnetite nanoparticles using a plant-based approach
- Investigate if cellulose is a suitable support for magnetite nanoparticles
- Determine if magnetite nanoparticles show adsorption affinity towards $SO_2$
- Asses which synthesis conditions should be changed to increase the adsorption capacity

### 1.5.2. Glycerol valorization

Glycerol overproduction from biodiesel is becoming a crucial problem as it significantly hinders the biodiesel production and causes important amounts of this chemical being used as combustion fuel. Photocatalytic upgrading of this compound using a cost effective and sustainable process is desired to maintain the biodiesel growth. Magnetite is a catalyst which satisfies these conditions but has not been reported for this specific application. Our collaborators from Tecnológico de Monterrey produced magnetite from revalorised steel and applied it in a Fenton-like system for degradation of black liquor [188]. Building on their work, in the second part of this thesis we would like to determine whether magnetite or modified magnetite is as suitable

photocatalyst for partial oxidation of glycerol to dihydroxyacetone. Related objectives are covered in this thesis to determine if this photocatalytical process is suitable:

- Determine if magnetite can be doped by metal nanoparticles using a plant-based approach
- Evaluate the intrinsic activity of magnetite for the oxidation of glycerol in a Fenton-like system
- Expand the applicability of magnetite to perform this reaction without hydrogen peroxide

## 1.6. Content of the thesis

This thesis is separated in four chapters. Chapter 1 provided necessary background information through a brief literature review to better understand the scope of the research. Chapter 2 will cover the application of a cellulose-based adsorbent modified with magnetite nanoparticles in the adsorption process of trace concentrations of $SO_2$. This chapter summarizes the synthesis parameters and evaluates their effect on the adsorption capacities of the different adsorbents. Chapter 3 describes a sustainable method to obtain magnetite nanoparticles and their application in the oxidation of glycerol. Different reaction conditions are varied to increase the glycerol conversion and selectively for dihydroxyacetone over other oxidation products. Chapter 4 summarizes the key findings from this thesis and discusses future work to be carried out for both applications.

# References


[1] El-Kady, M. M.; Ansari, I.; Arora, C.; Rai, N.; Soni, S.; Verma, D. K.; Singh, P.; Mahmoud, A. E. D. Nanomaterials: A Comprehensive Review of Applications, Toxicity, Impact, and Fate to Environment. *J. Mol. Liq.* **2023**, *370*, 121046. https://doi.org/10.1016/j.molliq.2022.121046.

[2] Baig, N.; Kammakakam, I.; Falath, W. Nanomaterials: A Review of Synthesis Methods, Properties, Recent Progress, and Challenges. *Mater. Adv.* **2021**, *2* (6), 1821–1871. https://doi.org/10.1039/D0MA00807A.

[3] Roduner, E. Size Matters: Why Nanomaterials Are Different. *Chem. Soc. Rev.* **2006**, *35* (7), 583–592. https://doi.org/10.1039/B502142C.

[4] Lu, W.; Lieber, C. M. Nanoelectronics from the Bottom Up. *Nat. Mater.* **2007**, *6* (11), 841–850. https://doi.org/10.1038/nmat2028.

[5] Sahani, S.; Sharma, Y. C. Advancements in Applications of Nanotechnology in Global Food Industry. *Food Chem.* **2021**, *342*, 128318. https://doi.org/10.1016/j.foodchem.2020.128318.

[6] Goyal, R. K. *Nanomaterials and Nanocomposites: Synthesis, Properties, Characterization Techniques, and Applications*; CRC Press: Boca Raton, 2017. https://doi.org/10.1201/9781315153285.

[7] Yetisen, A. K.; Qu, H.; Manbachi, A.; Butt, H.; Dokmeci, M. R.; Hinestroza, J. P.; Skorobogatiy, M.; Khademhosseini, A.; Yun, S. H. Nanotechnology in Textiles. *ACS Nano* **2016**, *10* (3), 3042–3068. https://doi.org/10.1021/acsnano.5b08176.

[8] *ISO 80004-1:2023*. ISO. https://www.iso.org/standard/79525.html (accessed 2024-12-07).

[9] Khan, S.; Hossain, M. K. 2 - Classification and Properties of Nanoparticles. In *Nanoparticle-Based Polymer Composites*; Mavinkere Rangappa, S., Parameswaranpillai, J., Yashas Gowda, T. G., Siengchin, S., Seydibeyoglu, M. O., Eds.; Woodhead Publishing Series in Composites Science and Engineering; Woodhead Publishing, 2022; pp 15–54. https://doi.org/10.1016/B978-0-12-824272-8.00009-9.

[10] Saleh, T. A. Nanomaterials: Classification, Properties, and Environmental Toxicities. *Environ. Technol. Innov.* **2020**, *20*, 101067. https://doi.org/10.1016/j.eti.2020.101067.

[11] Kroto, H. W.; Heath, J. R.; O'Brien, S. C.; Curl, R. F.; Smalley, R. E. C60: Buckminsterfullerene. *Nature* **1985**, *318* (6042), 162–163. https://doi.org/10.1038/318162a0.

[12] Patel, K. D.; Singh, R. K.; Kim, H.-W. Carbon-Based Nanomaterials as an Emerging Platform for Theranostics. *Mater. Horiz.* **2019**, *6* (3), 434–469. https://doi.org/10.1039/C8MH00966J.

[13] Iijima, S. Helical Microtubules of Graphitic Carbon. *Nature* **1991**, *354* (6348), 56–58. https://doi.org/10.1038/354056a0.

[14] Iye, Y. 1.10 - Electronic States and Transport Properties of Carbon Crystalline: Graphene, Nanotube, and Graphite. In *Comprehensive Semiconductor Science and Technology*; Bhattacharya, P., Fornari, R., Kamimura, H., Eds.; Elsevier: Amsterdam, 2011; pp 359–382. https://doi.org/10.1016/B978-0-44-453153-7.00068-7.

[15] Kausar, A. Chapter 1 - Fullerene: Fundamentals and State-of-the-Art. In *Polymer/Fullerene Nanocomposites*; Kausar, A., Ed.; Micro and Nano Technologies; Elsevier, 2023; pp 1–19. https://doi.org/10.1016/B978-0-323-99515-3.00001-8.

[16] Nakamura, E.; Isobe, H. Functionalized Fullerenes in Water. The First 10 Years of Their Chemistry, Biology, and Nanoscience. *Acc. Chem. Res.* **2003**, *36* (11), 807–815. https://doi.org/10.1021/ar030027y.
[17] Montellano, A.; Ros, T. D.; Bianco, A.; Prato, M. Fullerene C60 as a Multifunctional System for Drug and Gene Delivery. *Nanoscale* **2011**, *3* (10), 4035–4041. https://doi.org/10.1039/C1NR10783F.
[18] Chen, Z.; Ma, L.; Liu, Y.; Chen, C. Applications of Functionalized Fullerenes in Tumor Theranostics. *Theranostics* **2012**, *2* (3), 238–250. https://doi.org/10.7150/thno.3509.
[19] Ando, T. The Electronic Properties of Graphene and Carbon Nanotubes. *NPG Asia Mater.* **2009**, *1* (1), 17–21. https://doi.org/10.1038/asiamat.2009.1.
[20] Allen, M. J.; Tung, V. C.; Kaner, R. B. Honeycomb Carbon: A Review of Graphene. *Chem. Rev.* **2010**, *110* (1), 132–145. https://doi.org/10.1021/cr900070d.
[21] Popov, V. N. Carbon Nanotubes: Properties and Application. *Mater. Sci. Eng. R Rep.* **2004**, *43* (3), 61–102. https://doi.org/10.1016/j.mser.2003.10.001.
[22] Ibrahim, K. S. Carbon Nanotubes-Properties and Applications: A Review. *Carbon Lett.* **2013**, *14* (3), 131–144. https://doi.org/10.5714/CL.2013.14.3.131.
[23] Mittal, G.; Dhand, V.; Rhee, K. Y.; Park, S.-J.; Lee, W. R. A Review on Carbon Nanotubes and Graphene as Fillers in Reinforced Polymer Nanocomposites. *J. Ind. Eng. Chem.* **2015**, *21*, 11–25. https://doi.org/10.1016/j.jiec.2014.03.022.
[24] Peng, L.-M.; Zhang, Z.; Wang, S. Carbon Nanotube Electronics: Recent Advances. *Mater. Today* **2014**, *17* (9), 433–442. https://doi.org/10.1016/j.mattod.2014.07.008.
[25] Saleh, T. A. Chapter 8 - Properties of Nanoadsorbents and Adsorption Mechanisms. In *Interface Science and Technology*; Saleh, T. A., Ed.; Surface Science of Adsorbents and Nanoadsorbents; Elsevier, 2022; Vol. 34, pp 233–263. https://doi.org/10.1016/B978-0-12-849876-7.00010-5.
[26] Wang, L.; Hasanzadeh Kafshgari, M.; Meunier, M. Optical Properties and Applications of Plasmonic-Metal Nanoparticles. *Adv. Funct. Mater.* **2020**, *30* (51), 2005400. https://doi.org/10.1002/adfm.202005400.
[27] Montes-García, V.; A. Squillaci, M.; Diez-Castellnou, M.; Khac Ong, Q.; Stellacci, F.; Samorì, P. Chemical Sensing with Au and Ag Nanoparticles. *Chem. Soc. Rev.* **2021**, *50* (2), 1269–1304. https://doi.org/10.1039/D0CS01112F.
[28] Ag, Au and Pt Decorated TiO2 Biocompatible Nanospheres for UV & Vis Photocatalytic Water Treatment. *Appl. Surf. Sci.* **2020**, *509*, 145217. https://doi.org/10.1016/j.apsusc.2019.145217.
[29] Franke, M. E.; Koplin, T. J.; Simon, U. Metal and Metal Oxide Nanoparticles in Chemiresistors: Does the Nanoscale Matter? *Small* **2006**, *2* (1), 36–50. https://doi.org/10.1002/smll.200500261.
[30] Chavali, M. S.; Nikolova, M. P. Metal Oxide Nanoparticles and Their Applications in Nanotechnology. *SN Appl. Sci.* **2019**, *1* (6), 607. https://doi.org/10.1007/s42452-019-0592-3.
[31] Akbari, A.; Amini, M.; Tarassoli, A.; Eftekhari-Sis, B.; Ghasemian, N.; Jabbari, E. Transition Metal Oxide Nanoparticles as Efficient Catalysts in Oxidation Reactions. *Nano-Struct. Nano-Objects* **2018**, *14*, 19–48. https://doi.org/10.1016/j.nanoso.2018.01.006.
[32] Zedan, A. F.; Mohamed, A. T.; El-Shall, M. S.; AlQaradawi, S. Y.; AlJaber, A. S. Tailoring the Reducibility and Catalytic Activity of CuO Nanoparticles for Low Temperature CO Oxidation. *RSC Adv.* **2018**, *8* (35), 19499–19511. https://doi.org/10.1039/C8RA03623C.

[33] Yan, Z.; Yang, H.; Ouyang, J.; Tang, A. In Situ Loading of Highly-Dispersed CuO Nanoparticles on Hydroxyl-Group-Rich SiO2-AlOOH Composite Nanosheets for CO Catalytic Oxidation. *Chem. Eng. J.* **2017**, *316*, 1035–1046. https://doi.org/10.1016/j.cej.2017.02.043.

[34] Stark, W. J.; Stoessel, P. R.; Wohlleben, W.; Hafner, A. Industrial Applications of Nanoparticles. *Chem. Soc. Rev.* **2015**, *44* (16), 5793–5805. https://doi.org/10.1039/C4CS00362D.

[35] Koch, C. C.; Whittenberger, J. D. Mechanical Milling/Alloying of Intermetallics. *Intermetallics* **1996**, *4* (5), 339–355. https://doi.org/10.1016/0966-9795(96)00001-5.

[36] Yadav, T. P.; Yadav, R. M.; Singh, D. P. Mechanical Milling: A Top Down Approach for the Synthesis of Nanomaterials and Nanocomposites. *Nanosci. Nanotechnol.* **2012**, *2* (3), 22–48.

[37] Suryanarayana, C. Mechanical Alloying and Milling. *Prog. Mater. Sci.* **2001**, *46* (1), 1–184. https://doi.org/10.1016/S0079-6425(99)00010-9.

[38] Benjamin, J. S. Dispersion Strengthened Superalloys by Mechanical Alloying. *Metall. Trans.* **1970**, *1* (10), 2943–2951. https://doi.org/10.1007/BF03037835.

[39] El-Eskandarany, M. S.; Al-Hazza, A.; Al-Hajji, L. A.; Ali, N.; Al-Duweesh, A. A.; Banyan, M.; Al-Ajmi, F. Mechanical Milling: A Superior Nanotechnological Tool for Fabrication of Nanocrystalline and Nanocomposite Materials. *Nanomaterials* **2021**, *11* (10), 2484. https://doi.org/10.3390/nano11102484.

[40] Ayyub, P.; Chandra, R.; Taneja, P.; Sharma, A. K.; Pinto, R. Synthesis of Nanocrystalline Material by Sputtering and Laser Ablation at Low Temperatures. *Appl. Phys. A* **2001**, *73* (1), 67–73. https://doi.org/10.1007/s003390100833.

[41] Wasa, K.; Kitabatake, M.; Adachi, H. 3 - Sputtering Phenomena. In *Thin Film Materials Technology*; Wasa, K., Kitabatake, M., Adachi, H., Eds.; William Andrew Publishing: Norwich, NY, 2004; pp 71–114. https://doi.org/10.1016/B978-081551483-1.50004-6.

[42] Wender, H.; Migowski, P.; Feil, A. F.; Teixeira, S. R.; Dupont, J. Sputtering Deposition of Nanoparticles onto Liquid Substrates: Recent Advances and Future Trends. *Coord. Chem. Rev.* **2013**, *257* (17), 2468–2483. https://doi.org/10.1016/j.ccr.2013.01.013.

[43] Semaltianos, N. G. Nanoparticles by Laser Ablation. *Crit. Rev. Solid State Mater. Sci.* **2010**, *35* (2), 105–124. https://doi.org/10.1080/10408431003788233.

[44] Salavati-Niasari, M.; Davar, F.; Mir, N. Synthesis and Characterization of Metallic Copper Nanoparticles via Thermal Decomposition. *Polyhedron* **2008**, *27* (17), 3514–3518. https://doi.org/10.1016/j.poly.2008.08.020.

[45] Szczyglewska, P.; Feliczak-Guzik, A.; Nowak, I. Nanotechnology–General Aspects: A Chemical Reduction Approach to the Synthesis of Nanoparticles. *Molecules* **2023**, *28* (13), 4932. https://doi.org/10.3390/molecules28134932.

[46] Wang, H.; Qiao, X.; Chen, J.; Ding, S. Preparation of Silver Nanoparticles by Chemical Reduction Method. *Colloids Surf. Physicochem. Eng. Asp.* **2005**, *256* (2), 111–115. https://doi.org/10.1016/j.colsurfa.2004.12.058.

[47] Lassoued, A.; Dkhil, B.; Gadri, A.; Ammar, S. Control of the Shape and Size of Iron Oxide (α-Fe2O3) Nanoparticles Synthesized through the Chemical Precipitation Method. *Results Phys.* **2017**, *7*, 3007–3015. https://doi.org/10.1016/j.rinp.2017.07.066.

[48] Petcharoen, K.; Sirivat, A. Synthesis and Characterization of Magnetite Nanoparticles via the Chemical Co-Precipitation Method. *Mater. Sci. Eng. B* **2012**, *177* (5), 421–427. https://doi.org/10.1016/j.mseb.2012.01.003.

[49] Bokov, D.; Turki Jalil, A.; Chupradit, S.; Suksatan, W.; Javed Ansari, M.; Shewael, I. H.; Valiev, G. H.; Kianfar, E. Nanomaterial by Sol-Gel Method: Synthesis and Application. *Adv. Mater. Sci. Eng.* **2021**, *2021* (1), 5102014. https://doi.org/10.1155/2021/5102014.

[50] Danks, A. E.; Hall, S. R.; Schnepp, Z. The Evolution of 'Sol–Gel' Chemistry as a Technique for Materials Synthesis. *Mater. Horiz.* **2016**, *3* (2), 91–112. https://doi.org/10.1039/C5MH00260E.

[51] Navas, D.; Fuentes, S.; Castro-Alvarez, A.; Chavez-Angel, E. Review on Sol-Gel Synthesis of Perovskite and Oxide Nanomaterials. *Gels* **2021**, *7* (4), 275. https://doi.org/10.3390/gels7040275.

[52] Hench, L. L.; West, J. K. The Sol-Gel Process. *Chem. Rev.* **1990**, *90* (1), 33–72. https://doi.org/10.1021/cr00099a003.

[53] Li, J.; Wu, Q.; Wu, J. Synthesis of Nanoparticles via Solvothermal and Hydrothermal Methods. In *Handbook of Nanoparticles*; Aliofkhazraei, M., Ed.; Springer International Publishing: Cham, 2016; pp 295–328. https://doi.org/10.1007/978-3-319-15338-4_17.

[54] Ge, S.; Shi, X.; Sun, K.; Li, C.; Uher, C.; Baker, J. R. Jr.; Banaszak Holl, M. M.; Orr, B. G. Facile Hydrothermal Synthesis of Iron Oxide Nanoparticles with Tunable Magnetic Properties. *J. Phys. Chem. C* **2009**, *113* (31), 13593–13599. https://doi.org/10.1021/jp902953t.

[55] Saleh, S. M.; Soliman, A. M.; Sharaf, M. A.; Kale, V.; Gadgil, B. Influence of Solvent in the Synthesis of Nano-Structured ZnO by Hydrothermal Method and Their Application in Solar-Still. *J. Environ. Chem. Eng.* **2017**, *5* (1), 1219–1226. https://doi.org/10.1016/j.jece.2017.02.004.

[56] Torres-Gómez, N.; Nava, O.; Argueta-Figueroa, L.; García-Contreras, R.; Baeza-Barrera, A.; Vilchis-Nestor, A. R. Shape Tuning of Magnetite Nanoparticles Obtained by Hydrothermal Synthesis: Effect of Temperature. *J. Nanomater.* **2019**, *2019* (1), 7921273. https://doi.org/10.1155/2019/7921273.

[57] Outokesh, M.; Hosseinpour, M.; Ahmadi, S. J.; Mousavand, T.; Sadjadi, S.; Soltanian, W. Hydrothermal Synthesis of CuO Nanoparticles: Study on Effects of Operational Conditions on Yield, Purity, and Size of the Nanoparticles. *Ind. Eng. Chem. Res.* **2011**, *50* (6), 3540–3554. https://doi.org/10.1021/ie1017089.

[58] *Continuous Hydrothermal Synthesis of Inorganic Nanoparticles: Applications and Future Directions | Chemical Reviews*. https://pubs.acs.org/doi/full/10.1021/acs.chemrev.6b00417 (accessed 2024-12-08).

[59] Abid, N.; Khan, A. M.; Shujait, S.; Chaudhary, K.; Ikram, M.; Imran, M.; Haider, J.; Khan, M.; Khan, Q.; Maqbool, M. Synthesis of Nanomaterials Using Various Top-down and Bottom-up Approaches, Influencing Factors, Advantages, and Disadvantages: A Review. *Adv. Colloid Interface Sci.* **2022**, *300*, 102597. https://doi.org/10.1016/j.cis.2021.102597.

[60] Mittal, A. K.; Chisti, Y.; Banerjee, U. C. Synthesis of Metallic Nanoparticles Using Plant Extracts. *Biotechnol. Adv.* **2013**, *31* (2), 346–356. https://doi.org/10.1016/j.biotechadv.2013.01.003.

[61] Patil, M. P.; Kim, G.-D. Eco-Friendly Approach for Nanoparticles Synthesis and Mechanism behind Antibacterial Activity of Silver and Anticancer Activity of Gold Nanoparticles. *Appl. Microbiol. Biotechnol.* **2017**, *101* (1), 79–92. https://doi.org/10.1007/s00253-016-8012-8.

[62] Iravani, S. Green Synthesis of Metal Nanoparticles Using Plants. *Green Chem.* **2011**, *13* (10), 2638–2650. https://doi.org/10.1039/C1GC15386B.

[63] Jain, S.; Mehata, M. S. Medicinal Plant Leaf Extract and Pure Flavonoid Mediated Green Synthesis of Silver Nanoparticles and Their Enhanced Antibacterial Property. *Sci. Rep.* **2017**, *7* (1), 15867. https://doi.org/10.1038/s41598-017-15724-8.

[64] Makarov, V. V.; Love, A. J.; Sinitsyna, O. V.; Makarova, S. S.; Yaminsky, I. V.; Taliansky, M. E.; Kalinina, N. O. "Green" Nanotechnologies: Synthesis of Metal Nanoparticles Using Plants. *Acta Naturae* **2014**, *6* (1), 35.

[65] Nasrollahzadeh, M.; Mohammad Sajadi, S. Green Synthesis of Copper Nanoparticles Using *Ginkgo Biloba* L. Leaf Extract and Their Catalytic Activity for the Huisgen [3 + 2] Cycloaddition of Azides and Alkynes at Room Temperature. *J. Colloid Interface Sci.* **2015**, *457*, 141–147. https://doi.org/10.1016/j.jcis.2015.07.004.

[66] Jiménez-Rosado, M.; Gomez-Zavaglia, A.; Guerrero, A.; Romero, A. Green Synthesis of ZnO Nanoparticles Using Polyphenol Extracts from Pepper Waste (Capsicum Annuum). *J. Clean. Prod.* **2022**, *350*, 131541. https://doi.org/10.1016/j.jclepro.2022.131541.

[67] Nasrollahzadeh, M.; Sajadi, S. M.; Rostami-Vartooni, A.; Hussin, S. M. Green Synthesis of CuO Nanoparticles Using Aqueous Extract of *Thymus Vulgaris* L. Leaves and Their Catalytic Performance for *N*-Arylation of Indoles and Amines. *J. Colloid Interface Sci.* **2016**, *466*, 113–119. https://doi.org/10.1016/j.jcis.2015.12.018.

[68] Mosaviniya, M.; Kikhavani, T.; Tanzifi, M.; Tavakkoli Yaraki, M.; Tajbakhsh, P.; Lajevardi, A. Facile Green Synthesis of Silver Nanoparticles Using *Crocus Haussknechtii Bois* Bulb Extract: Catalytic Activity and Antibacterial Properties. *Colloid Interface Sci. Commun.* **2019**, *33*, 100211. https://doi.org/10.1016/j.colcom.2019.100211.

[69] El-Seedi, H. R.; El-Shabasy, R. M.; Khalifa, S. A. M.; Saeed, A.; Shah, A.; Shah, R.; Iftikhar, F. J.; Abdel-Daim, M. M.; Omri, A.; Hajrahand, N. H.; Sabir, J. S. M.; Zou, X.; Halabi, M. F.; Sarhan, W.; Guo, W. Metal Nanoparticles Fabricated by Green Chemistry Using Natural Extracts: Biosynthesis, Mechanisms, and Applications. *RSC Adv.* **2019**, *9* (42), 24539–24559. https://doi.org/10.1039/C9RA02225B.

[70] Prado, J. M.; Vardanega, R.; Debien, I. C. N.; Meireles, M. A. A.; Gerschenson, L. N.; Sowbhagya, H. B.; Chemat, S.; Prado, J. M.; Vardanega, R.; Debien, I. C. N.; Meireles, M. A. A.; Gerschenson, L. N.; Sowbhagya, H. B.; Chemat, S. Chapter 6 - Conventional Extraction. In *Food Waste Recovery (Second Edition)*; Galanakis, C. M., Ed.; Academic Press: San Diego, 2021; pp 109–127. https://doi.org/10.1016/B978-0-12-820563-1.00015-9.

[71] Patra, J. K.; Baek, K.-H. Green Nanobiotechnology: Factors Affecting Synthesis and Characterization Techniques. *J. Nanomater.* **2014**, *2014* (1), 417305. https://doi.org/10.1155/2014/417305.

[72] Dwivedi, A. D.; Gopal, K. Biosynthesis of Silver and Gold Nanoparticles Using *Chenopodium Album* Leaf Extract. *Colloids Surf. Physicochem. Eng. Asp.* **2010**, *369* (1), 27–33. https://doi.org/10.1016/j.colsurfa.2010.07.020.

[73] kazemi, S.; Hosseingholian, A.; Gohari, S. D.; Feirahi, F.; Moammeri, F.; Mesbahian, G.; Moghaddam, Z. S.; Ren, Q. Recent Advances in Green Synthesized Nanoparticles: From Production to Application. *Mater. Today Sustain.* **2023**, *24*, 100500. https://doi.org/10.1016/j.mtsust.2023.100500.

[74] Vanlalveni, C.; Lallianrawna, S.; Biswas, A.; Selvaraj, M.; Changmai, B.; Rokhum, S. L. Green Synthesis of Silver Nanoparticles Using Plant Extracts and Their Antimicrobial Activities: A Review of Recent Literature. *RSC Adv.* **2021**, *11* (5), 2804–2837. https://doi.org/10.1039/D0RA09941D.

[75] Pastoriza, S.; Pérez-Burillo, S.; Rufián-Henares, J. Á. How Brewing Parameters Affect the Healthy Profile of Tea. *Curr. Opin. Food Sci.* **2017**, *14*, 7–12. https://doi.org/10.1016/j.cofs.2016.12.001.

[76] Zhao, C.-N.; Tang, G.-Y.; Cao, S.-Y.; Xu, X.-Y.; Gan, R.-Y.; Liu, Q.; Mao, Q.-Q.; Shang, A.; Li, H.-B. Phenolic Profiles and Antioxidant Activities of 30 Tea Infusions from Green, Black, Oolong, White, Yellow and Dark Teas. *Antioxidants* **2019**, *8* (7), 215. https://doi.org/10.3390/antiox8070215.

[77] Lin, Y.-S.; Tsai, Y.-J.; Tsay, J.-S.; Lin, J.-K. Factors Affecting the Levels of Tea Polyphenols and Caffeine in Tea Leaves. *J. Agric. Food Chem.* **2003**, *51* (7), 1864–1873. https://doi.org/10.1021/jf021066b.

[78] Unachukwu, U. J.; Ahmed, S.; Kavalier, A.; Lyles, J. T.; Kennelly, E. J. White and Green Teas (Camellia Sinensis Var. Sinensis): Variation in Phenolic, Methylxanthine, and Antioxidant Profiles. *J. Food Sci.* **2010**, *75* (6), C541–C548. https://doi.org/10.1111/j.1750-3841.2010.01705.x.

[79] Wirwis, A.; Sadowski, Z. Green Synthesis of Silver Nanoparticles: Optimizing Green Tea Leaf Extraction for Enhanced Physicochemical Properties. *ACS Omega* **2023**, *8* (33), 30532–30549. https://doi.org/10.1021/acsomega.3c03775.

[80] Widatalla, H. A.; Yassin, L. F.; Alrasheid, A. A.; Ahmed, S. A. R.; Widdatallah, M. O.; Eltilib, S. H.; Mohamed, A. A. Green Synthesis of Silver Nanoparticles Using Green Tea Leaf Extract, Characterization and Evaluation of Antimicrobial Activity. *Nanoscale Adv.* **2022**, *4* (3), 911–915. https://doi.org/10.1039/D1NA00509J.

[81] Rolim, W. R.; Pelegrino, M. T.; de Araújo Lima, B.; Ferraz, L. S.; Costa, F. N.; Bernardes, J. S.; Rodigues, T.; Brocchi, M.; Seabra, A. B. Green Tea Extract Mediated Biogenic Synthesis of Silver Nanoparticles: Characterization, Cytotoxicity Evaluation and Antibacterial Activity. *Appl. Surf. Sci.* **2019**, *463*, 66–74. https://doi.org/10.1016/j.apsusc.2018.08.203.

[82] Nakhjavani, M.; Nikkhah, V.; Sarafraz, M. M.; Shoja, S.; Sarafraz, M. Green Synthesis of Silver Nanoparticles Using Green Tea Leaves: Experimental Study on the Morphological, Rheological and Antibacterial Behaviour. *Heat Mass Transf.* **2017**, *53* (10), 3201–3209. https://doi.org/10.1007/s00231-017-2065-9.

[83] Sun, Q.; Cai, X.; Li, J.; Zheng, M.; Chen, Z.; Yu, C.-P. Green Synthesis of Silver Nanoparticles Using Tea Leaf Extract and Evaluation of Their Stability and Antibacterial Activity. *Colloids Surf. Physicochem. Eng. Asp.* **2014**, *444*, 226–231. https://doi.org/10.1016/j.colsurfa.2013.12.065.

[84] Asghar, M. A.; Zahir, E.; Shahid, S. M.; Khan, M. N.; Asghar, M. A.; Iqbal, J.; Walker, G. Iron, Copper and Silver Nanoparticles: Green Synthesis Using Green and Black Tea Leaves Extracts and Evaluation of Antibacterial, Antifungal and Aflatoxin B1 Adsorption Activity. *LWT* **2018**, *90*, 98–107. https://doi.org/10.1016/j.lwt.2017.12.009.

[85] Irshad, S.; Salamat, A.; Anjum, A. A.; Sana, S.; Saleem, R. S.; Naheed, A.; Iqbal, A. Green Tea Leaves Mediated ZnO Nanoparticles and Its Antimicrobial Activity. *Cogent Chem.* **2018**, *4* (1), 1469207. https://doi.org/10.1080/23312009.2018.1469207.

[86] MalligArjuna Rao, S.; Kotteeswaran, S.; Visagamani, A. M. Green Synthesis of Zinc Oxide Nanoparticles from *Camellia Sinensis:* Organic Dye Degradation and Antibacterial Activity. *Inorg. Chem. Commun.* **2021**, *134*, 108956. https://doi.org/10.1016/j.inoche.2021.108956.

[87] Nune, S. K.; Chanda, N.; Shukla, R.; Katti, K.; Kulkarni, R. R.; Thilakavathy, S.; Mekapothula, S.; Kannan, R.; Katti, K. V. Green Nanotechnology from Tea: Phytochemicals in Tea as Building Blocks for Production of Biocompatible Gold Nanoparticles. *J. Mater. Chem.* **2009**, *19* (19), 2912–2920. https://doi.org/10.1039/B822015H.

[88] Ahmeda, A.; Zangeneh, A.; Zangeneh, M. M. Green Synthesis and Chemical Characterization of Gold Nanoparticle Synthesized Using Camellia Sinensis Leaf Aqueous Extract for the Treatment of Acute Myeloid Leukemia in Comparison to Daunorubicin in a Leukemic Mouse Model. *Appl. Organomet. Chem.* **2020**, *34* (3), e5290. https://doi.org/10.1002/aoc.5290.

[89] Huang, L.; Weng, X.; Chen, Z.; Megharaj, M.; Naidu, R. Green Synthesis of Iron Nanoparticles by Various Tea Extracts: Comparative Study of the Reactivity. *Spectrochim. Acta. A. Mol. Biomol. Spectrosc.* **2014**, *130*, 295–301. https://doi.org/10.1016/j.saa.2014.04.037.

[90] Weng, X.; Huang, L.; Chen, Z.; Megharaj, M.; Naidu, R. Synthesis of Iron-Based Nanoparticles by Green Tea Extract and Their Degradation of Malachite. *Ind. Crops Prod.* **2013**, *51*, 342–347. https://doi.org/10.1016/j.indcrop.2013.09.024.

[91] Wang, T.; Lin, J.; Chen, Z.; Megharaj, M.; Naidu, R. Green Synthesized Iron Nanoparticles by Green Tea and Eucalyptus Leaves Extracts Used for Removal of Nitrate in Aqueous Solution. *J. Clean. Prod.* **2014**, *83*, 413–419. https://doi.org/10.1016/j.jclepro.2014.07.006.

[92] Kuang, Y.; Wang, Q.; Chen, Z.; Megharaj, M.; Naidu, R. Heterogeneous Fenton-like Oxidation of Monochlorobenzene Using Green Synthesis of Iron Nanoparticles. *J. Colloid Interface Sci.* **2013**, *410*, 67–73. https://doi.org/10.1016/j.jcis.2013.08.020.

[93] Truskewycz, A.; Shukla, R.; Ball, A. S. Iron Nanoparticles Synthesized Using Green Tea Extracts for the Fenton-like Degradation of Concentrated Dye Mixtures at Elevated Temperatures. *J. Environ. Chem. Eng.* **2016**, *4* (4, Part A), 4409–4417. https://doi.org/10.1016/j.jece.2016.10.008.

[94] Hao, R.; Li, D.; Zhang, J.; Jiao, T. Green Synthesis of Iron Nanoparticles Using Green Tea and Its Removal of Hexavalent Chromium. *Nanomaterials* **2021**, *11* (3), 650. https://doi.org/10.3390/nano11030650.

[95] Wu, Z.; Su, X.; Lin, Z.; Khan, N. I.; Owens, G.; Chen, Z. Removal of As(V) by Iron-Based Nanoparticles Synthesized via the Complexation of Biomolecules in Green Tea Extracts and an Iron Salt. *Sci. Total Environ.* **2021**, *764*, 142883. https://doi.org/10.1016/j.scitotenv.2020.142883.

[96] *Executive summary – World Energy Outlook 2023 – Analysis*. IEA. https://www.iea.org/reports/world-energy-outlook-2023/executive-summary (accessed 2024-12-08).

[97] *Where greenhouse gases come from - U.S. Energy Information Administration (EIA)*. https://www.eia.gov/energyexplained/energy-and-the-environment/where-greenhouse-gases-come-from.php (accessed 2024-12-08).

[98] Macdonald, B. C. T.; Denmead, O. T.; White, I.; Melville, M. D. Natural Sulfur Dioxide Emissions from Sulfuric Soils. *Atmos. Environ.* **2004**, *38* (10), 1473–1480. https://doi.org/10.1016/j.atmosenv.2003.12.005.

[99] 5f139f4c-Final-Global-Hotspot-and-Emission-Sources-for-So2_19th_august-2019.Pdf. https://www.greenpeace.org/static/planet4-africa-stateless/2019/08/5f139f4c-final-global-hotspot-and-emission-sources-for-so2_19th_august-2019.pdf (accessed 2024-12-08).

[100] Yuan, D.-F.; Liu, Y.; Trabelsi, T.; Zhang, Y.-R.; Li, J.; Francisco, J. S.; Guo, H.; Wang, L.-S. Probing the Dynamics and Bottleneck of the Key Atmospheric SO2 Oxidation Reaction by the Hydroxyl Radical. *Proc. Natl. Acad. Sci.* **2024**, *121* (6), e2314819121. https://doi.org/10.1073/pnas.2314819121.

[101] Calvert, J. G.; Lazrus, A.; Kok, G. L.; Heikes, B. G.; Walega, J. G.; Lind, J.; Cantrell, C. A. Chemical Mechanisms of Acid Generation in the Troposphere. *Nature* **1985**, *317* (6032), 27–35. https://doi.org/10.1038/317027a0.

[102] Cox, R. A. Particle Formation from Homogeneous Reactions of Sulphur Dioxide and Nitrogen Dioxide. *Tellus* **1974**. https://doi.org/10.3402/tellusa.v26i1-2.9782.

[103] Venners, S. A.; Wang, B.; Xu, Z.; Schlatter, Y.; Wang, L.; Xu, X. Particulate Matter, Sulfur Dioxide, and Daily Mortality in Chongqing, China. *Environ. Health Perspect.* **2003**, *111* (4), 562–567. https://doi.org/10.1289/ehp.5664.

[104] H144-29-2016-Eng.Pdf. https://publications.gc.ca/collections/collection_2016/sc-hc/H144-29-2016-eng.pdf (accessed 2024-12-08).

[105] US EPA, O. *Sulfur Dioxide Trends*. https://www.epa.gov/air-trends/sulfur-dioxide-trends (accessed 2024-12-08).

[106] Li, C.; McLinden, C.; Fioletov, V.; Krotkov, N.; Carn, S.; Joiner, J.; Streets, D.; He, H.; Ren, X.; Li, Z.; Dickerson, R. R. India Is Overtaking China as the World's Largest Emitter of Anthropogenic Sulfur Dioxide. *Sci. Rep.* **2017**, *7* (1), 14304. https://doi.org/10.1038/s41598-017-14639-8.

[107] Kuttippurath, J.; Patel, V. K.; Pathak, M.; Singh, A. Improvements in SO2 Pollution in India: Role of Technology and Environmental Regulations. *Environ. Sci. Pollut. Res.* **2022**, *29* (52), 78637–78649. https://doi.org/10.1007/s11356-022-21319-2.

[108] Pandey, R. A.; Biswas, R.; Chakrabarti, T.; Devotta, S. Flue Gas Desulfurization: Physicochemical and Biotechnological Approaches. *Crit. Rev. Environ. Sci. Technol.* **2005**. https://doi.org/10.1080/10643380500326374.

[109] *Document Display | NEPIS | US EPA*. https://nepis.epa.gov/Exe/ZyNET.exe/P1007IQM.TXT?ZyActionD=ZyDocument&Client=EPA&Index=2000+Thru+2005&Docs=&Query=&Time=&EndTime=&SearchMethod=1&TocRestrict=n&Toc=&TocEntry=&QField=&QFieldYear=&QFieldMonth=&QFieldDay=&IntQFieldOp=0&ExtQFieldOp=0&XmlQuery=&File=D%3A%5Czyfiles%5CIndex%20Data%5C00thru05%5CTxt%5C00000024%5CP1007IQM.txt&User=ANONYMOUS&Password=anonymous&SortMethod=h%7C-&MaximumDocuments=1&FuzzyDegree=0&ImageQuality=r75g8/r75g8/x150y150g16/i425&Display=hpfr&DefSeekPage=x&SearchBack=ZyActionL&Back=ZyActionS&BackDesc=Results%20page&MaximumPages=1&ZyEntry=1&SeekPage=x&ZyPURL# (accessed 2024-12-08).

[110] AR-13.Pdf. https://www3.epa.gov/region1/npdes/merrimackstation/pdfs/ar/AR-13.pdf (accessed 2024-12-08).

[111] Srivastava, R. K.; Jozewicz, W. Flue Gas Desulfurization: The State of the Art. *J. Air Waste Manag. Assoc.* **2001**, *51* (12), 1676–1688. https://doi.org/10.1080/10473289.2001.10464387.

[112] Córdoba, P. Status of Flue Gas Desulphurisation (FGD) Systems from Coal-Fired Power Plants: Overview of the Physic-Chemical Control Processes of Wet Limestone FGDs. *Fuel* **2015**, *144*, 274–286. https://doi.org/10.1016/j.fuel.2014.12.065.
[113] Valle-Zermeño, R. del; Formosa, J.; Chimenos, J. M. Wet Flue Gas Desulfurization Using Alkaline Agents. *Rev. Chem. Eng.* **2015**, *31* (4), 303–327. https://doi.org/10.1515/revce-2015-0002.
[114] De Gisi, S.; Molino, A.; Notarnicola, M. Enhancing the Recovery of Gypsum in Limestone-Based Wet Flue Gas Desulfurization with High Energy Ball Milling Process: A Feasibility Study. *Process Saf. Environ. Prot.* **2017**, *109*, 117–129. https://doi.org/10.1016/j.psep.2017.03.033.
[115] Zhu, J.; Ye, S.; Bai, J.; Wu, Z.; Liu, Z.; Yang, Y. A Concise Algorithm for Calculating Absorption Height in Spray Tower for Wet Limestone–Gypsum Flue Gas Desulfurization. *Fuel Process. Technol.* **2015**, *129*, 15–23. https://doi.org/10.1016/j.fuproc.2014.07.002.
[116] Shengyu, L.; Wende, X.; Pei, L.; Zhixiang, Y. Feasibility Study of New Limestone Flue Gas Desulfurization Process. *CLEAN – Soil Air Water* **2008**, *36* (5–6), 482–487. https://doi.org/10.1002/clen.200700106.
[117] Miller, B. G. CHAPTER 6 - Emissions Control Strategies for Power Plants. In *Coal Energy Systems*; Miller, B. G., Ed.; Sustainable World; Academic Press: Burlington, 2005; pp 283–392. https://doi.org/10.1016/B978-012497451-7/50006-1.
[118] Li, X.; Han, J.; Liu, Y.; Dou, Z.; Zhang, T. Summary of Research Progress on Industrial Flue Gas Desulfurization Technology. *Sep. Purif. Technol.* **2022**, *281*, 119849. https://doi.org/10.1016/j.seppur.2021.119849.
[119] Koralegedara, N. H.; Pinto, P. X.; Dionysiou, D. D.; Al-Abed, S. R. Recent Advances in Flue Gas Desulfurization Gypsum Processes and Applications – A Review. *J. Environ. Manage.* **2019**, *251*, 109572. https://doi.org/10.1016/j.jenvman.2019.109572.
[120] Gingerich, D. B.; Grol, E.; Mauter, M. S. Fundamental Challenges and Engineering Opportunities in Flue Gas Desulfurization Wastewater Treatment at Coal Fired Power Plants. *Environ. Sci. Water Res. Technol.* **2018**, *4* (7), 909–925. https://doi.org/10.1039/C8EW00264A.
[121] Poullikkas, A. Review of Design, Operating, and Financial Considerations in Flue Gas Desulfurization Systems. *Energy Technol. Policy* **2015**, *2* (1), 92–103. https://doi.org/10.1080/23317000.2015.1064794.
[122] An, X.-C.; Li, Z.-M.; Zhou, Y.; Zhu, W.; Tao, D.-J. Rapid Capture and Efficient Removal of Low-Concentration SO2 in Simulated Flue Gas by Hypercrosslinked Hollow Nanotube Ionic Polymers. *Chem. Eng. J.* **2020**, *394*, 124859. https://doi.org/10.1016/j.cej.2020.124859.
[123] Hammershøi, P. S.; Jangjou, Y.; Epling, W. S.; Jensen, A. D.; Janssens, T. V. W. Reversible and Irreversible Deactivation of Cu-CHA NH3-SCRcatalysts by SO2 and SO3. *Appl. Catal. B Environ.* **2018**, *226*, 38–45. https://doi.org/10.1016/j.apcatb.2017.12.018.
[124] Farrauto, R. J.; Wedding, B. Poisoning by SOx of Some Base Metal Oxide Auto Exhaust Catalysts. *J. Catal.* **1974**, *33* (2), 249–255. https://doi.org/10.1016/0021-9517(74)90268-1.
[125] Guo, Y.; Li, C.; Lu, S.; Zhao, C. Understanding the Deactivation of K2CO3/AC for Low-Concentration CO2 Removal in the Presence of Trace SO2 and NO2. *Chem. Eng. J.* **2016**, *301*, 325–333. https://doi.org/10.1016/j.cej.2016.05.011.

[126] Narayanan, P.; Lively, R. P.; Jones, C. W. Effect of SO2 on the CO2 Capture Performance of Self-Supported Branched Poly(Ethyleneimine) Scaffolds. *Energy Fuels* **2023**, *37* (7), 5257–5269. https://doi.org/10.1021/acs.energyfuels.2c03846.
[127] Xie, X.; Liu, L.; Liu, H.; Sun, Z. Mechanistic Insights into SO2-Induced Deactivation of Ni-Based Materials for Integrated CO2 Capture and Methanation. *Fuel* **2025**, *382*, 133755. https://doi.org/10.1016/j.fuel.2024.133755.
[128] Hanif, M. A.; Ibrahim, N.; Abdul Jalil, A. Sulfur Dioxide Removal: An Overview of Regenerative Flue Gas Desulfurization and Factors Affecting Desulfurization Capacity and Sorbent Regeneration. *Environ. Sci. Pollut. Res.* **2020**, *27* (22), 27515–27540. https://doi.org/10.1007/s11356-020-09191-4.
[129] Bamdad, H.; Hawboldt, K.; MacQuarrie, S. A Review on Common Adsorbents for Acid Gases Removal: Focus on Biochar. *Renew. Sustain. Energy Rev.* **2018**, *81*, 1705–1720. https://doi.org/10.1016/j.rser.2017.05.261.
[130] Zhang, P.; Wanko, H.; Ulrich, J. Adsorption of SO2 on Activated Carbon for Low Gas Concentrations. *Chem. Eng. Technol.* **2007**, *30* (5), 635–641. https://doi.org/10.1002/ceat.200600360.
[131] Raymundo-Piñero, E.; Cazorla-Amorós, D.; Salinas-Martinez de Lecea, C.; Linares-Solano, A. Factors Controling the SO2 Removal by Porous Carbons: Relevance of the SO2 Oxidation Step. *Carbon* **2000**, *38* (3), 335–344. https://doi.org/10.1016/S0008-6223(99)00109-8.
[132] Rosas, J. M.; Ruiz-Rosas, R.; Rodríguez-Mirasol, J.; Cordero, T. Kinetic Study of SO2 Removal over Lignin-Based Activated Carbon. *Chem. Eng. J.* **2017**, *307*, 707–721. https://doi.org/10.1016/j.cej.2016.08.111.
[133] Lizzio, A. A.; DeBarr, J. A. Mechanism of SO2 Removal by Carbon. *Energy Fuels* **1997**, *11* (2), 284–291. https://doi.org/10.1021/ef960197+.
[134] Lizzio, A. A.; DeBarr, J. A. Effect of Surface Area and Chemisorbed Oxygen on the SO2 Adsorption Capacity of Activated Char. *Fuel* **1996**, *75* (13), 1515–1522. https://doi.org/10.1016/0016-2361(96)00127-5.
[135] Martínez-Ahumada, E.; López-Olvera, A.; Jancik, V.; Sánchez-Bautista, J. E.; González-Zamora, E.; Martis, V.; Williams, D. R.; Ibarra, I. A. MOF Materials for the Capture of Highly Toxic H2S and SO2. *Organometallics* **2020**, *39* (7), 883–915. https://doi.org/10.1021/acs.organomet.9b00735.
[136] Srinivasan, A.; Grutzeck, M. W. The Adsorption of SO2 by Zeolites Synthesized from Fly Ash. *Environ. Sci. Technol.* **1999**, *33* (9), 1464–1469. https://doi.org/10.1021/es9802091.
[137] Yi, H.; Deng, H.; Tang, X.; Yu, Q.; Zhou, X.; Liu, H. Adsorption Equilibrium and Kinetics for SO2, NO, CO2 on Zeolites FAU and LTA. *J. Hazard. Mater.* **2012**, *203–204*, 111–117. https://doi.org/10.1016/j.jhazmat.2011.11.091.
[138] Liu, X.; Chen, L.; Qi, G. Enhanced SO2 Capture Performance of MnO2 by Doping with Alkali Metal Ions for Diesel Emission Control. *Chem. Eng. Technol.* **2018**, *41* (8), 1675–1681. https://doi.org/10.1002/ceat.201700542.
[139] Lowell, P. S.; Schwitzgebel, K.; Parsons, T. B.; Sladek, K. J. Selection of Metal Oxides for Removing SO2 From Flue Gas. *Ind. Eng. Chem. Process Des. Dev.* **1971**, *10* (3), 384–390. https://doi.org/10.1021/i260039a018.
[140] Bansal, R. C.; Goyal, M. Activated Carbon and Its Surface Structure. In *Activated Carbon Adsorption*; CRC Press, 2005.

[141] Raymundo-Piñero, E.; Cazorla-Amorós, D.; Linares-Solano, A. Temperature Programmed Desorption Study on the Mechanism of SO2 Oxidation by Activated Carbon and Activated Carbon Fibres. *Carbon* **2001**, *39* (2), 231–242. https://doi.org/10.1016/S0008-6223(00)00119-6.

[142] Bagreev, A.; Bashkova, S.; Bandosz, T. J. Adsorption of SO2 on Activated Carbons: The Effect of Nitrogen Functionality and Pore Sizes. *Langmuir* **2002**, *18* (4), 1257–1264. https://doi.org/10.1021/la011320e.

[143] Daley, M. A.; Mangun, C. L.; DeBarrb, J. A.; Riha, S.; Lizzio, A. A.; Donnals, G. L.; Economy, J. Adsorption of SO2 onto Oxidized and Heat-Treated Activated Carbon Fibers (ACFs). *Carbon* **1997**, *35* (3), 411–417. https://doi.org/10.1016/S0008-6223(97)89612-1.

[144] Li, B.; Ma, C. Study on the Mechanism of SO2 Removal by Activated Carbon. *Energy Procedia* **2018**, *153*, 471–477. https://doi.org/10.1016/j.egypro.2018.10.063.

[145] Lua, A. C.; Guo, J. Adsorption of Sulfur Dioxide on Activated Carbon from Oil-Palm Waste. *J. Environ. Eng.* **2001**, *127* (10), 895–901. https://doi.org/10.1061/(ASCE)0733-9372(2001)127:10(895).

[146] Abdulrasheed, A. A.; Jalil, A. A.; Triwahyono, S.; Zaini, M. A. A.; Gambo, Y.; Ibrahim, M. Surface Modification of Activated Carbon for Adsorption of SO2 and NOX: A Review of Existing and Emerging Technologies. *Renew. Sustain. Energy Rev.* **2018**, *94*, 1067–1085. https://doi.org/10.1016/j.rser.2018.07.011.

[147] Wang, J.; Zhao, F.; Hu, Y.; Zhao, R.; Liu, R. Modification of Activated Carbon Fiber by Loading Metals and Their Performance on SO2 Removal. *Chin. J. Chem. Eng.* **2006**, *14* (4), 478–485. https://doi.org/10.1016/S1004-9541(06)60102-X.

[148] Liu, X.-L.; Guo, J.-X.; Chu, Y.-H.; Luo, D.-M.; Yin, H.-Q.; Sun, M.-C.; Yavuz, R. Desulfurization Performance of Iron Supported on Activated Carbon. *Fuel* **2014**, *123*, 93–100. https://doi.org/10.1016/j.fuel.2014.01.068.

[149] Figueiredo, J. A.; Ismael, M. I.; Anjo, C. M. S.; Duarte, A. P. Cellulose and Derivatives from Wood and Fibers as Renewable Sources of Raw-Materials. In *Carbohydrates in Sustainable Development I*; Rauter, A. P., Vogel, P., Queneau, Y., Eds.; Springer: Berlin, Heidelberg, 2010; pp 117–128. https://doi.org/10.1007/128_2010_88.

[150] Atalla, R. H.; Isogai, A. 6.16 - Celluloses. In *Comprehensive Natural Products II*; Liu, H.-W. (Ben), Mander, L., Eds.; Elsevier: Oxford, 2010; pp 493–539. https://doi.org/10.1016/B978-008045382-8.00691-2.

[151] Klemm, D.; Heublein, B.; Fink, H.-P.; Bohn, A. Cellulose: Fascinating Biopolymer and Sustainable Raw Material. *Angew. Chem. Int. Ed.* **2005**, *44* (22), 3358–3393. https://doi.org/10.1002/anie.200460587.

[152] Moon, R. J.; Martini, A.; Nairn, J.; Simonsen, J.; Youngblood, J. Cellulose Nanomaterials Review: Structure, Properties and Nanocomposites. *Chem. Soc. Rev.* **2011**, *40* (7), 3941–3994. https://doi.org/10.1039/C0CS00108B.

[153] Pinkert, A.; Marsh, K. N.; Pang, S. Reflections on the Solubility of Cellulose. *Ind. Eng. Chem. Res.* **2010**, *49* (22), 11121–11130. https://doi.org/10.1021/ie1006596.

[154] Heinze, T.; El Seoud, O. A.; Koschella, A. *Cellulose Derivatives*; Springer Series on Polymer and Composite Materials; Springer International Publishing: Cham, 2018. https://doi.org/10.1007/978-3-319-73168-1.

[155] Seddiqi, H.; Oliaei, E.; Honarkar, H.; Jin, J.; Geonzon, L. C.; Bacabac, R. G.; Klein-Nulend, J. Cellulose and Its Derivatives: Towards Biomedical Applications. *Cellulose* **2021**, *28* (4), 1893–1931. https://doi.org/10.1007/s10570-020-03674-w.

[156] Yang, C.; Tan, T.; Zhu, X. Adsorptive Capacity of Ethylenediamine Treated Oxidised Rice Straw for Sulfur Dioxide. *Carbohydr. Polym.* **2012**, *87* (2), 1843–1848. https://doi.org/10.1016/j.carbpol.2011.10.013.

[157] Zafari, R.; Fauteux-Lefebvre, C. Surface Modification Investigation of Nanocrystalline Cellulose with Combined Functional Groups for Sulfur Dioxide Capture. *Adsorption* **2023**, *29* (3), 151–161. https://doi.org/10.1007/s10450-023-00390-2.

[158] Zafari, R.; Mendonça, F. G.; Tom Baker, R.; Fauteux-Lefebvre, C. Efficient SO2 Capture Using an Amine-Functionalized, Nanocrystalline Cellulose-Based Adsorbent. *Sep. Purif. Technol.* **2023**, *308*, 122917. https://doi.org/10.1016/j.seppur.2022.122917.

[159] Ho, N. A. D.; Leo, C. P. A Review on the Emerging Applications of Cellulose, Cellulose Derivatives and Nanocellulose in Carbon Capture. *Environ. Res.* **2021**, *197*, 111100. https://doi.org/10.1016/j.envres.2021.111100.

[160] Valdebenito, F.; García, R.; Cruces, K.; Ciudad, G.; Chinga-Carrasco, G.; Habibi, Y. CO2 Adsorption of Surface-Modified Cellulose Nanofibril Films Derived from Agricultural Wastes. *ACS Sustain. Chem. Eng.* **2018**, *6* (10), 12603–12612. https://doi.org/10.1021/acssuschemeng.8b00771.

[161] Campbell, S.; Bernard, F. L.; Rodrigues, D. M.; Rojas, M. F.; Carreño, L. Á.; Chaban, V. V.; Einloft, S. Performance of Metal-Functionalized Rice Husk Cellulose for CO2 Sorption and CO2/N2 Separation. *Fuel* **2019**, *239*, 737–746. https://doi.org/10.1016/j.fuel.2018.11.078.

[162] Hokkanen, S.; Bhatnagar, A.; Sillanpää, M. A Review on Modification Methods to Cellulose-Based Adsorbents to Improve Adsorption Capacity. *Water Res.* **2016**, *91*, 156–173. https://doi.org/10.1016/j.watres.2016.01.008.

[163] Fakhre, N. A.; Ibrahim, B. M. The Use of New Chemically Modified Cellulose for Heavy Metal Ion Adsorption. *J. Hazard. Mater.* **2018**, *343*, 324–331. https://doi.org/10.1016/j.jhazmat.2017.08.043.

[164] d'Halluin, M.; Rull-Barrull, J.; Bretel, G.; Labrugère, C.; Le Grognec, E.; Felpin, F.-X. Chemically Modified Cellulose Filter Paper for Heavy Metal Remediation in Water. *ACS Sustain. Chem. Eng.* **2017**, *5* (2), 1965–1973. https://doi.org/10.1021/acssuschemeng.6b02768.

[165] Zhou, Y.; Jin, Q.; Hu, X.; Zhang, Q.; Ma, T. Heavy Metal Ions and Organic Dyes Removal from Water by Cellulose Modified with Maleic Anhydride. *J. Mater. Sci.* **2012**, *47* (12), 5019–5029. https://doi.org/10.1007/s10853-012-6378-2.

[166] S. Chaudhari, D.; P. Upadhyay, R.; Y. Shinde, G.; B. Gawande, M.; Filip, J.; S. Varma, R.; Zbořil, R. A Review on Sustainable Iron Oxide Nanoparticles: Syntheses and Applications in Organic Catalysis and Environmental Remediation. *Green Chem.* **2024**, *26* (13), 7579–7655. https://doi.org/10.1039/D4GC01870B.

[167] Arias, L. S.; Pessan, J. P.; Vieira, A. P. M.; Lima, T. M. T. de; Delbem, A. C. B.; Monteiro, D. R. Iron Oxide Nanoparticles for Biomedical Applications: A Perspective on Synthesis, Drugs, Antimicrobial Activity, and Toxicity. *Antibiotics* **2018**, *7* (2), 46. https://doi.org/10.3390/antibiotics7020046.

[168] Klotz, S.; Steinle-Neumann, G.; Strässle, Th.; Philippe, J.; Hansen, Th.; Wenzel, M. J. Magnetism and the Verwey Transition in ${\mathrm{Fe}}_{3}{\mathrm{O}}_{4}$ under Pressure. *Phys. Rev. B* **2008**, *77* (1), 012411. https://doi.org/10.1103/PhysRevB.77.012411.

[169] Baeza, A.; Guillena, G.; Ramón, D. J. Magnetite and Metal-Impregnated Magnetite Catalysts in Organic Synthesis: A Very Old Concept with New Promising Perspectives. *ChemCatChem* **2016**, *8* (1), 49–67. https://doi.org/10.1002/cctc.201500854.

[170] Ertl, G. Heterogeneous Catalysis on the Atomic Scale. *Chem. Rec.* **2001**, *1* (1), 33–45. https://doi.org/10.1002/1528-0691(2001)1:1<33::AID-TCR6>3.0.CO;2-V.

[171] Glebov, L. S.; Kliger, G. A.; Popova, T. P.; Shiryaeva, V. E.; Ryzhikov, V. P.; Marchevskaya, E. V.; Lesik, O. A.; Loktev, S. M.; Beryezkin, V. G. Obtaining Dimethylalkylamines from CO, H2 and (CH3)2NH by the Modified Fischer-Tropsch Synthesis on a Reduced Fused Magnetite Catalyst: Molecular Weight Distribution of the Products and Synthesis Mechanism. *J. Mol. Catal.* **1986**, *35* (3), 335–348. https://doi.org/10.1016/0304-5102(86)87081-X.

[172] LUND, C. R. F.; KUBSH, J. E.; DUMESIC, J. A. Water Gas Shift over Magnetite-Based Catalysts. In *Solid State Chemistry in Catalysis*; ACS Symposium Series; American Chemical Society, 1985; Vol. 279, pp 313–338. https://doi.org/10.1021/bk-1985-0279.ch019.

[173] Pham, X.-M.; Pham, D. L.; Hanh, N. T.; Dang Thi, T. A.; Thuy Giang, L. N.; Phuong, H. T.; Anh, N. T.; Nhung, H. T.; Le, G. T.; Hoang, M. H.; Nguyen, T. V. An Initial Evaluation on the Adsorption of SO2 and NO2 over Porous Fe3O4 Nanoparticles Synthesized by Facile Scalable Method. *J. Chem.* **2019**, *2019* (1), 9742826. https://doi.org/10.1155/2019/9742826.

[174] Ye, C. Z.; Ariya, P. A. Co-Adsorption of Gaseous Benzene, Toluene, Ethylbenzene, m-Xylene (BTEX) and SO2 on Recyclable Fe3O4 Nanoparticles at 0–101% Relative Humidities. *J. Environ. Sci.* **2015**, *31*, 164–174. https://doi.org/10.1016/j.jes.2014.10.019.

[175] Fu, H.; Wang, X.; Wu, H.; Yin, Y.; Chen, J. Heterogeneous Uptake and Oxidation of SO2 on Iron Oxides. *J. Phys. Chem. C* **2007**, *111* (16), 6077–6085. https://doi.org/10.1021/jp070087b.

[176] Baltrusaitis, J.; Cwiertny, D. M.; Grassian, V. H. Adsorption of Sulfur Dioxide on Hematite and Goethite Particle Surfaces. *Phys. Chem. Chem. Phys.* **2007**, *9* (41), 5542–5554. https://doi.org/10.1039/B709167B.

[177] Pirzadi, Z.; Meshkani, F. From Glycerol Production to Its Value-Added Uses: A Critical Review. *Fuel* **2022**, *329*, 125044. https://doi.org/10.1016/j.fuel.2022.125044.

[178] Kaur, J.; Sarma, A. K.; Jha, M. K.; Gera, P. Valorisation of Crude Glycerol to Value-Added Products: Perspectives of Process Technology, Economics and Environmental Issues. *Biotechnol. Rep.* **2020**, *27*, e00487. https://doi.org/10.1016/j.btre.2020.e00487.

[179] Liu, Y.; Zhong, B.; Lawal, A. Recovery and Utilization of Crude Glycerol, a Biodiesel Byproduct. *RSC Adv.* **2022**, *12* (43), 27997–28008. https://doi.org/10.1039/D2RA05090K.

[180] Laurie, V. F.; Waterhouse, A. L. Oxidation of Glycerol in the Presence of Hydrogen Peroxide and Iron in Model Solutions and Wine. Potential Effects on Wine Color. *J. Agric. Food Chem.* **2006**, *54* (13), 4668–4673. https://doi.org/10.1021/jf053036p.

[181] Pereira, M. C.; Oliveira, L. C. A.; Murad, E. Iron Oxide Catalysts: Fenton and Fentonlike Reactions – a Review. *Clay Miner.* **2012**, *47* (3), 285–302. https://doi.org/10.1180/claymin.2012.047.3.01.

[182] Usman, M.; Faure, P.; Ruby, C.; Hanna, K. Remediation of PAH-Contaminated Soils by Magnetite Catalyzed Fenton-like Oxidation. *Appl. Catal. B Environ.* **2012**, *117–118*, 10–17. https://doi.org/10.1016/j.apcatb.2012.01.007.

[183] Bagheri, S.; Julkapli, N. M. Magnetite Hybrid Photocatalysis: Advance Environmental Remediation. *Rev. Inorg. Chem.* **2016**, *36* (3), 135–151. https://doi.org/10.1515/revic-2015-0014.

[184] Minella, M.; Marchetti, G.; De Laurentiis, E.; Malandrino, M.; Maurino, V.; Minero, C.; Vione, D.; Hanna, K. Photo-Fenton Oxidation of Phenol with Magnetite as Iron Source. *Appl. Catal. B Environ.* **2014**, *154–155*, 102–109. https://doi.org/10.1016/j.apcatb.2014.02.006.

[185] Khlyustova, A.; Sirotkin, N.; Kusova, T.; Kraev, A.; Titov, V.; Agafonov, A. Doped TiO2: The Effect of Doping Elements on Photocatalytic Activity. *Mater. Adv.* **2020**, *1* (5), 1193–1201. https://doi.org/10.1039/D0MA00171F.

[186] Sarina, S.; Waclawik, E. R.; Zhu, H. Photocatalysis on Supported Gold and Silver Nanoparticles under Ultraviolet and Visible Light Irradiation. *Green Chem.* **2013**, *15* (7), 1814–1833. https://doi.org/10.1039/C3GC40450A.

[187] Nchimi Nono, K.; Vahl, A.; Terraschke, H. Towards High-Performance Photo-Fenton Degradation of Organic Pollutants with Magnetite-Silver Composites: Synthesis, Catalytic Reactions and In Situ Insights. *Nanomaterials* **2024**, *14* (10), 849. https://doi.org/10.3390/nano14100849.

[188] Flores-López, Z. D.; Solís-Díaz, A. B.; Cervantes-Aviles, P. A.; Thangarasu, P.; Kumar, D.; Kaur, H.; Singh, J.; Lokande, P.; Huerta-Aguilar, C. A.; Mubarak, N. M. Insight Mechanism of Magnetic Activated Catalyst Derived from Recycled Steel Residue for Black Liquor Degradation. *Sci. Rep.* **2024**, *14* (1), 19057. https://doi.org/10.1038/s41598-024-70072-8.

# Chapter 2. A sustainable approach to trace sulfur dioxide capture: adsorption on cellulose modified with iron oxide nanoparticles


## Abstract

Cellulose is an increasingly popular biopolymer used in research due to its abundance, sustainable nature and non-toxicity. Adsorbents made from cellulose and its derivatives have been mostly focusing on capturing $CO_2$ and limited research has been conducted on $SO_2$ capture. In this work, we modified nanocrystalline and microcrystalline cellulose with iron oxide nanoparticles synthesized using green tea extract. The nanoparticle deposition was confirmed by Fourier Transform Infrared Spectroscopy (FTIR), scanning electron microscopy (SEM), scanning transmission electron microscopy (STEM), energy dispersive X-ray spectroscopy (EDS) and X-ray diffraction (XRD). Thermogravimetric analysis (TGA) was used to quantify the concentration of deposited iron. The impact of the type of cellulose used as the support, the deposition time, the iron concentration in the adsorbents and the volume of reducing agent used for the deposition were investigated by breakthrough experiments. The presence of 1.24 wt% of iron on microcrystalline cellulose increased its adsorption capacity from $3.8\times10^{-4}$ $mg_{SO_2}/g_{adsorbent}$ to 0.22 $mg_{SO_2}/g_{adsorbent}$. The chemical speciation of the iron and the iron content in the adsorbent had significant impacts on the capture capacity. These findings show that iron oxide nanoparticles supported on microcrystalline cellulose are a promising adsorbent for $SO_2$ capture while being sustainable and benign.



## Keywords

Sulfur dioxide, adsorption, cellulose, iron oxide, green tea, sustainable

## 2.1. Introduction

Sulfur dioxide ($SO_2$) is a pollutant gas which is released in the atmosphere predominantly from fossil fuel combustion, although natural emissions are also observed. $SO_2$ forms sulfuric acid ($H_2SO_4$) when in contact with water in the atmosphere, resulting in acid rain. $SO_2$ pollution may also lead to respiratory diseases, cardiovascular diseases and an increased risk of type-2 diabetes [1]. Its emissions were targeted along with five other pollutants beginning from 1970 through the EPA's Clean Air Act [2]. Since then, emissions have decreased in North America but remain a problem in developing countries [3].

Various technologies are available to remove $SO_2$ from flue gas, and it can be achieved either through wet or dry processes [4].Wet flue gas desulfurization (FGD) processes are the most commonly used and can achieve over 99% $SO_2$ removal [5]. However, they are energy intensive and generate significant amounts of wastewater [6]. They are also inefficient when dealing with low or trace concentrations of $SO_2$ [7]. Indeed, some $SO_2$ is always leftover in the gaseous stream exiting the FGD process. This can be problematic for further processes intending to revalorise or further purify flue gas (i.e. $CO_2$) because even low concentrations of $SO_2$ in the gaseous stream can deactivate or poison catalysts.

Alternative approaches have been proposed to capture $SO_2$ from gaseous streams, especially for low concentration streams. Interesting techniques involving ionic liquids [8–10] and deep eutectic solvents [11,12] have been successful for this application. However, these materials require complex synthesis or molecules which renders their application on larger scale unrealistic and uneconomical. Adsorption is another approach used to capture the low concentrations of $SO_2$. The efficiency of adsorbents generally relies on their high surface area which maximises the number of pores available to interact with the targeted molecule. As such, activated carbons [13–15], zeolites [16,17], porous organic polymers [18], and metal organic frameworks (MOFs) [19,20], which are all materials with high surface areas, have been investigated for the application of $SO_2$ removal at high and low concentrations. Modification of these adsorbents can be further achieved to enhance their activity by targeting specific characteristics of the $SO_2$ molecule, for example its dipole moment [21,22] or its acidic nature [23].

Cellulose, an increasingly popular carbon-based material investigated for diverse applications ranging from biomedical applications [24] to polymer engineering [25] and metal nanoparticle support [26], has not been extensively reported for $SO_2$ capture. It has however been

mainly studied for the adsorption of another acidic gas: $CO_2$. Although cellulose on its own shows limited adsorption, when it is modified the adsorption mechanism can be enhanced. For example, Zhao et al. [27] deposited $Ca^{2+}$ ions on the surface of cellulose which increased the adsorption capacity due to the formation of $CaCO_3$. Campbell et al. [28] increased the adsorption by favoring an acid-base mechanism between $CO_2$ and nanoparticles of $Fe_3O_4$ or $TiO_2$ deposited on cellulose. Our group has previously explored the chemical modification of nanocrystalline cellulose (NCC) with amine and carboxylic acid for this application [29,30].

Being an affordable, benign, abundant and sustainable material, its research potential is obvious. It is composed of repeating D-glucopyranose units linked by β-1,4-glycosidic bonds [31]. Bulk cellulose can be easily processed into a micro or nanoscale material via chemical or mechanical methods thus increasing its end application potential. Reactive hydroxyl (-OH) functional groups cover the surface of the natural polymer, allowing for easy chemical modification by routine chemistry such as esterification or oxidation reactions [32]. Cellulose is also a good support for metallic nanoparticles due to its porous fibrous nature which contributes to preventing agglomeration of nanoparticles [33]. Prior chemical modification to introduce polar functional groups or direct use of inherent hydroxyls covering the surface of cellulose can also contribute to nanoparticle stability [34]. Three methods are commonly used to disperse nanoparticles on cellulose: reduction from an external reducing agent, reduction from cellulose modified with reducing functional groups and reduction from the inherent hydroxyl on cellulose [35].

Besides, iron oxide nanoparticles are receiving growing attention due to their abundance, their non-toxicity, their low cost and their versatility [36]. They have been studied for $SO_2$ capture as they are able to catalytically oxidise $SO_2$ to the corresponding sulfite or sulfate species which are more strongly adsorbed [37,38]. The iron oxide nanoparticles are also characterised by high specific areas and porosities which contribute synergistically to improve the adsorption process [39,40]. Their combination with an adsorbent could enhance its affinity for $SO_2$ [41,42]. When Arcibar-Orozco et al. [43] supported iron nanoparticles on activated carbon, they observed an increase of 25% in the amount of $SO_2$ adsorbed compared to unmodified activated carbon.

Metallic nanoparticles are now commonly used in the development of novel materials allowing achieving various functions. In the process of developing novel materials, metallic nanoparticles are typically formed from a bottom-up approach. Iron oxide nanoparticles can be

easily synthesized using various techniques. A very common approach is the coprecipitation method which consists in mixing iron precursor salts in a solvent and increasing the pH to precipitate the iron out of the solution and yield nanoparticles [44]. A stabilising agent is added to control the nucleation and produce nanoparticles of the desired size [45]. Another approach is the liquid phase chemical reduction. This technique consists in dissolving an iron salt in an appropriate solvent and using a reducing agent such as sodium borohydride or hydrazine to form metallic ions. A capping agent is added to control the nucleation and prevent agglomeration of nanoparticles [46]. Typical capping agents are sodium citrate or surfactants such as Cetyltrimethylammonium bromide (CTAB) [47]. Although efficient and convenient, this method has the drawbacks of requiring expensive, hazardous chemicals and relying on trained personnel to ensure the reaction conditions are adequate [48]. A similar approach gaining in popularity is the use of "green" reducing agents to synthesize nanoparticle, one of which is plant extracts. It is well documented that plant extracts contain phytochemicals such as sugars, proteins and polyphenols which act as reducing agents to form the metallic ions [49]. Furthermore, these molecules can also stabilise the nanoparticles, thus preventing their agglomeration and removing the need to use another reagent to prevent this phenomenon. This approach has the advantages of being sustainable, non-toxic, rapid, easy to handle and cost-effective [50].

In this study, we aim to develop a novel, green adsorbent for trace concentration $SO_2$ capture. The adsorbent is a combination of two materials which have shown activity towards $SO_2$: cellulose and biosynthesized iron oxide nanoparticles. By modifying cellulose with these nanoparticles, a novel adsorbent is produced trough an environmentally friendly synthesis. Two types of cellulose, nanocrystalline cellulose (NCC) and microcrystalline cellulose (MCC), are compared as adsorbent supports. The iron nanoparticle concentration, deposition time as well as the amount of plant-based reducing agent are investigated to improve the adsorption capacity.

## 2.2. Experimental

### 2.2.1. Materials

Nanocrystalline cellulose was obtained from CelluForce Inc. (Windsor, Quebec). Microcrystalline cellulose, $Fe(NO_3)_3$ (98%) and coarse quartz wool (9-30 μm) were purchased from Fisher Scientific. $Na_2CO_3$ (≥99.5%) was purchased from VWR chemicals. Folin-Ciocalteu

reagent was purchased from Sigma-Aldrich. Reagents were used without further purification. Deionized water was used for the plant extractions and for the adsorbent synthesis. Green tea, peppermint tea, lime and lemon were purchased from a local supermarket. Gas cylinders containing pure Argon (99.99 %) and a mixture of $SO_2$ in Ar (provided at 25 ppm $SO_2$ in Ar) were received from Messer.

### 2.2.2. Plant extract preparation

In a 250 mL Erlenmeyer connected to a condenser, 100 mL of deionized water was brought to boiling point. Once the water was boiling, 1 to 4 g of the desired plant were quickly added, depending on the desired extract concentration. The mixture was allowed to boil for 5 minutes. After 5 minutes, it was removed from heat and left on the bench to cool for 10 minutes. The solution was then filtered by vacuum filtration to recover the plant extract. The extract was kept at 4°C for up to 10 days. In the case of green tea and peppermint tea, the dried leaves were removed from the bag in which they were contained, without further treatment. In the case of lime and lemon, the skin was peeled, dried overnight in an oven at 40°C and ground prior to being extracted.

### 2.2.3. Total phenolic content assessment

The total phenolic content (TPC) measurement was performed based on a reported method [51]. Briefly, 15 mL of water, 1 mL of Folin-Ciocalteu phenol reagent, and 1 mL of either a solution of know concentration of gallic acid (to prepare a calibration curve) or 1 mL of the plant extract were added to test tubes. They were agitated and allowed to sit for 6 minutes. 3 mL of a 20 wt% solution of sodium carbonate was added, and the tubes were agitated again and let for 120 minutes in the dark. Their absorbance was then measured at 765nm using a UV-Vis spectrophotometer (Zuzi 4201/20). The TPC of the plant extract solutions was determined by performing a linear regression from a gallic acid calibration curve and was reported as gallic acid equivalents (GAE). The dry GAE concentration of the plants was calculated using the following equation:

$$C_{GAE,D} = C_{GAE,E} \times \frac{1}{C_{Extract}} \tag{2.1}$$

Where $C_{GAE,D}$ is the dry GAE concentration of the plants, $C_{GAE,E}$ is the GAE concentration in the extract which is determined from the calibration curve (mg GAE/L) and $C_{Extract}$ is the plant extract concentration (2 g of green tea/100 mL of water).

For calculations of the stoichiometric equivalents, it was considered that each GAE would be equivalent to three hydrides as each gallic acid molecule contains three reactive phenolic hydroxyls. Equivalents were calculated to yield a fully reduced iron species (zero valent) from the iron (III) precursors salt solution. The following equation was used:

$$Equivalents_{GT} = \frac{\frac{C_{GAE,E}}{M_{GA}} \times \frac{3\ mol_{hydride}}{mol_{GA}} \times V_{GT}}{\frac{m_{Fe(NO_3)_3 \cdot 9H_2O}}{M_{Fe(NO_3)_3 \cdot 9H_2O}} \times \frac{3\ mol_{hydride}}{mol_{Fe}}} \quad (2.2)$$

Where $M_{GA}$ is the molar mass of gallic acid, $V_{GT}$ is the volume of green tea used for the reduction, $m_{Fe(NO_3)_3 \cdot 9H_2O}$ is the mass of iron nitrate nonahydrate used for the deposition and $M_{Fe(NO_3)_3 \cdot 9H_2O}$ is the molar mass of iron nitrate nonahydrate

### 2.2.4. Adsorbent synthesis

100 mL of deionized water was added to an Erlenmeyer flask. The desired amount of $Fe(NO_3)_3$ was then added based on the desired deposition. One gram of cellulose was added to the solution and the suspension was stirred with a sufficient speed to maintain the cellulose in suspension. The desired volume of plant extract was added dropwise to the suspension. An immediate colour change from orange to black was observed. The vessel was then capped with parafilm, and the suspension was allowed to stir for the desired time (24 to 168 hours). Once the deposition time was reached, the stirring was stopped, and the suspension was centrifuged for 10 minutes at 4000 rpm. The aqueous supernatant was discarded, and the recovered solid was washed twice with ethanol (with repeated centrifugation). It was then dried overnight at 40°C.

### 2.2.5. $SO_2$ capture experiments

100 mg of adsorbent was loaded in a quartz tube (4 mm ID, 6.5 mm OD, mm length) to form a packed bed of around 2 cm in length. The adsorbent was sandwiched in quartz wool to prevent it from moving during the adsorption experiment. This packed bed reactor was connected to the capture setup which allows for either argon to flow (to purge the system) or 25 ppm $SO_2$ in argon (for the adsorption experiment). Mass flow controllers (Aalborg DPC) were used to control the inlet gas flow rate using a modified version of the LabView program provided by Aalborg. A volumetric flow meter (Agilent CrossLab CS) was connected at the outlet to measure the exiting flow rate. The $SO_2$ concentration in the outlet stream was measured every second using a Draeger X-am 2500 detector. Prior to performing the capture experiment, the system was purged using argon (15 mL/min) for at least 15 minutes or until the detector indicated 0.1 ppm $SO_2$ or less. All capture experiments were conducted at room temperature and 1 atm, with an inlet flow rate of 10 mL/min. The experimental setup was placed in a fume hood and the exiting gas was vented.

The capture capacity of the adsorbents can be calculated by determining the area over the breakthrough curves up to the inlet concentration. To normalize the calculations and account for experimental differences, the blank's breakthrough curve was used as the upper limit below which the area would be calculated. The area from which the adsorption capacity was determined was calculated by the following equations.

$$a_{under\ the\ curve} = \sum_{t=0}^{t=(t-1)} y_1 \times (x_2 - x_1) \tag{2.3}$$

$$a_{capacity} = a_{blank} - a_{sample}\ [ppm\ SO_2 \cdot s] \tag{2.4}$$

From this area the mass of $SO_2$ adsorbed was calculated using the flow rate (*f*)

$$m_{SO_2} = a_{capacity}[ppm\ SO_2 \cdot s] \times 10^{-6} \frac{\frac{mol\ SO_2}{mol}}{ppm\ SO_2} \times f[mL/min] \times \frac{64\,000\ mg\ SO_2}{mol\ SO_2} \times \frac{1\ mol}{22\,400\ mL} \times \frac{1\ min}{60\ s} \tag{2.5}$$

And the capture capacity per mass of adsorbent or iron was calculated using the following

$$C = \frac{m_{SO_2}\,[mg\,SO_2]}{m_{\frac{adsorbent}{Fe}}\left[m_{\frac{adsorbent}{Fe}}\right]} \times \frac{1000\,mg}{g} \tag{2.6}$$

### 2.2.6. Adsorbent characterization

Transmission electron microscopy (TEM) and scanning transmission electron microscopy (STEM) were used to evaluate the Fe-based nanoparticle size and their dispersion on the cellulose support. This was achieved by capturing images using the high-angle annular dark-field (HAADF) detector and by performing energy dispersive X-ray spectroscopy (EDS) maps as well as localized measurements This characterisation was performed using a Thermo Scientific Talos F2000X. Scanning electron microscopy (SEM) was performed to investigate the morphology of the adsorbent using a JEOL 6610LV SEM. The functional groups present on the adsorbent were quantified by performing FTIR in ATR mode using a Thermo Scientific Nicolet 6700 FTIR/ATR. X-ray diffraction (XRD) was performed using a Bruker D8 Endeavor Polycrystalline X-ray diffractometer with a Cu Kα sealed-tube source (λ=1.54184 Å) and a LynxEye XE-T 1-D silicon strip detector. The iron weight content in each adsorbent was measured by Thermogravimetric analysis (TGA) using a TA Instruments TGA 550. Air was used as the atmosphere for the process and a ramp of 10°C/minute up to 1000°C was used to fully degrade the cellulose supported. The remaining mass was attributed to iron, considering it was entirely in the $Fe_2O_3$ oxidation state.

## 2.3. Results and discussion

### 2.3.1. Plant extract selection

The measurement of the total phenolic content (TPC) of the various used plant extracts with the Folin-Ciocalteu reagent was performed as an initial step. This reagent contains a mixture of sodium molybdate and sodium tungstate which is reduced by phenols to produce a blue colored complex that absorbs light at 765 nm [52]. The unknown TPC of plant extracts was determined by using a calibration curve which was made from gallic acid. As such, the TPC is reported as gallic acid equivalents (GAE). The aim was to determine the concentrations of polyphenols in the plant extracts and identify the highest containing one. These phytochemicals are known to have the ability to reduce the metallic ions into nanoparticles via the donation of electrons from the readily

oxidizable phenols present on the molecules [53]. The oxidized polyphenols are then able to stabilise the nanoparticles thus preventing agglomeration and avoiding the use of another stabilising agent such as a surfactant. Figure 2.1 depicts the general pathway through which this phenomenon occurs.

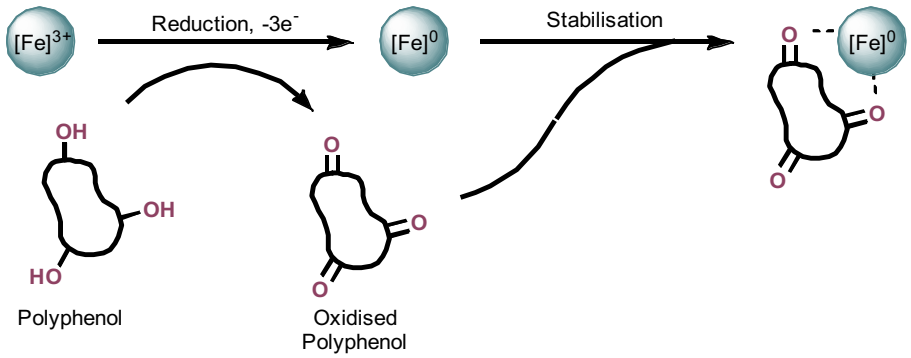


**Figure 2.1.** Scheme of iron reduction by polyphenols

By selecting a plant extract having a high polyphenol concentration, the reduction step should perform more readily, and less extract would be required, allowing for better reagent economy. Extract of four different plants (green tea, peppermint tea, lime and lemon) were prepared at concentrations of 1 g, 2 g and 4 g of dry plant for 100 mL of water. Figure 2.2a shows how the TPC increases with increasing extract concentration, which is expected. Green tea extract has a significantly higher TPC when compared to lemon and curry extracts, and its TPC is similar to peppermint tea extract. Both tea extracts contain a GAE concentration about 10 times higher than the lemon and lime extract with the same concentration. This is in agreement with various other studies which have used green tea extract for the synthesis of various metal nanoparticles [54–56]. However, when assessing the concentration of polyphenols in the dry plant (the dry plant before extraction, figure 2.2b) it was observed that for both citrus extracts, the dry GAE concentration was independent of the extract concentration. This is expected as the TPC in the dry plant is fixed for a specific plant and should rather change based on the species of the plant. However, this was not the case for both tea extracts for which a decrease in the dry GAE concentration was measured with increasing extract concentration. This indicates that as more dry plant is used to produce a higher concentration extract, the amount of polyphenols extracted by the water was not proportional, suggesting that a maximal extraction was achieved. Thus, using a

higher mass of dry plant to produce the extract did not lead to a significant increase in phenolic content in the plant extract. As such, green tea with a concentration of 2 g/100 mL was selected for the synthesis of the adsorbents in this study, as it allows for a good balance between the final phenolic concentration in the extract and the mass of dry plant used.

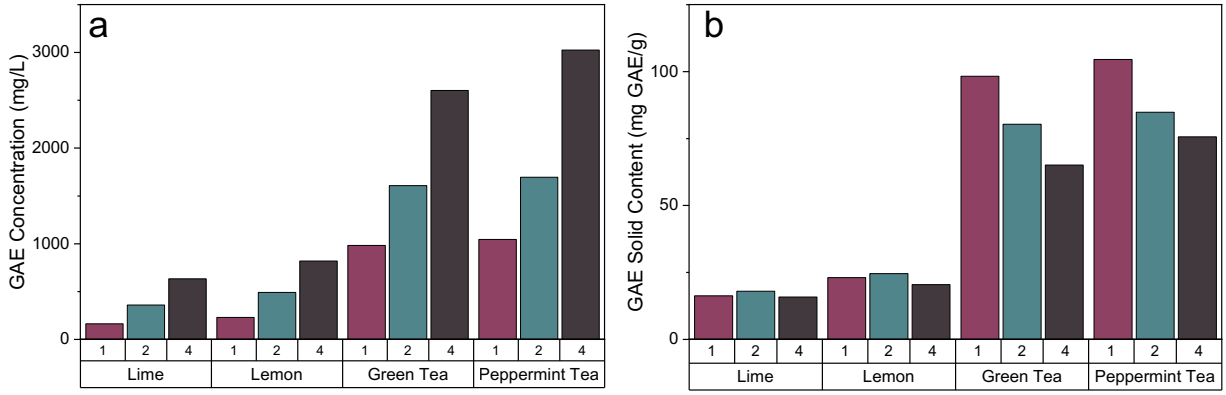


**Figure 2.2.** TPC measurement of four different plant extracts in terms of (a) GAE concentration and (b) GAE solid content

When establishing stoichiometric measurement to determine the volume of green tea required to perform the plant-based reduction of iron, the average GAE concentration, which was determined using the Folin-Ciocalteu total phenolic content assessment, was used. For the 2 g/100 mL extract, the average concentration was of 1607 mg GAE/L.

### 2.3.2. Synthesis parameters for the green iron deposition

Several synthesis parameters were varied to enhance the adsorption capacity of the adsorbent and determine which parameters were key to optimising the $SO_2$ capture. A summary of the synthesis conditions for the different adsorbents is found in table 2.1.

Adsorbent 1 depicts the initial conditions which were used as a reference point to be modified. A 10 wt% of iron was aimed for. The initial volume of green tea was selected based on a visual assessment of the solution's colour: green tea extract was added to the iron precursor solution causing an instant change of colour from orange to black, indicative of the formation of iron nanoparticles [53]. When the solution stopped darkening, the volume of green tea added was deemed sufficient and used as the reference volume. Adsorbents 2 and 3 were meant to evaluate if

the reference volume of reducing agent was sufficient and evaluate whether stoichiometric amounts of green tea extract would improve the adsorption properties. Adsorbent 4 aimed to investigate the chemical speciation of the iron deposited on the cellulose, hence the absence of reducing agent, and its impact on the adsorption process. Additionally, the type of cellulose used as the support was investigated (adsorbents 5-7), the deposition time (adsorbents 8-10), and the iron content (adsorbents 11-14) which were conducted using the reference volume of reducing agent adjusted to the aimed deposition.

**Table 2.1.** Adsorbent synthesis parameters

| Adsorbent | Aimed iron deposition (wt%) | Support | Deposition time (hours) | Volume of green tea (mL) | Green tea equivalents |
|---|---|---|---|---|---|
| 1 | 10 | MCC | 72 | 6 | 0.04 |
| 2 | 10 | MCC | 72 | 151 | 1 |
| 3 | 10 | MCC | 72 | 303 | 2 |
| 4 | 10 | MCC | 72 | 0 | 0 |
| 5 | 10 | NCC | 72 | 6 | 0.04 |
| 6 | 35 | NCC | 72 | 20 | 0.03 |
| 7 | 35 | MCC | 72 | 20 | 0.03 |
| 8 | 10 | MCC | 24 | 6 | 0.04 |
| 9 | 10 | MCC | 120 | 6 | 0.04 |
| 10 | 10 | MCC | 168 | 6 | 0.04 |
| 11 | 5 | MCC | 72 | 3 | 0.04 |
| 12 | 20 | MCC | 72 | 12 | 0.04 |
| 13 | 50 | MCC | 72 | 30 | 0.02 |
| 14 | 75 | MCC | 72 | 45 | 0.01 |

### 2.3.3. Characterization of the adsorbent

ATR-FTIR spectroscopy was used to characterize the starting cellulose material and its modification with Fe-based nanoparticles. Spectra of pristine MCC (figure 2.3a) exhibits the

characteristic peaks expected from cellulose. Namely, a broad peak at 3330 $cm^{-1}$ which is attributed to O-H stretching, a peak 2904 $cm^{-1}$ attributed to C-H stretching [57], a peak around 1320 $cm^{-1}$ corresponding to the O-H bending in alcohols [58] and a series of strong peaks at 1162, 1112 and 1057 $cm^{-1}$ characteristic of stretching in ethers and primary as well as secondary alcohols [58]. The deposition of Fe-based nanoparticles on the cellulosic support was monitored by assessing the variation of intensity in the peak located at 560 $cm^{-1}$ which we assigned to Fe-O [59–61]. The baseline of all the peaks was normalized to compare peak intensities. As seen in figure 2.3b, the intensity of this peak gradually increases as the aimed iron deposition is increased. This suggests that the deposition process is effective as higher depositions should lead to stronger peak intensity when a successful deposition is achieved. It is also important to note that there is no absorption in the 1600 $cm^{-1}$ range on the spectrum of the cellulose modified with a 50 wt% aim of Fe-based nanoparticles (figure 2.3a). This absorption would be typical from the stretching of carbonyls. This absence indicates that the reduction of the iron precursor was most probably carried out solely by the plant extract. Indeed, if the cellulose support contributed to the reduction, resulting carbonyl groups from the oxidation of the hydroxyls would have been observed by FTIR which was not the case. Hence the cellulose support did not seem to contribute nor get oxidised during the formation of nanoparticles.

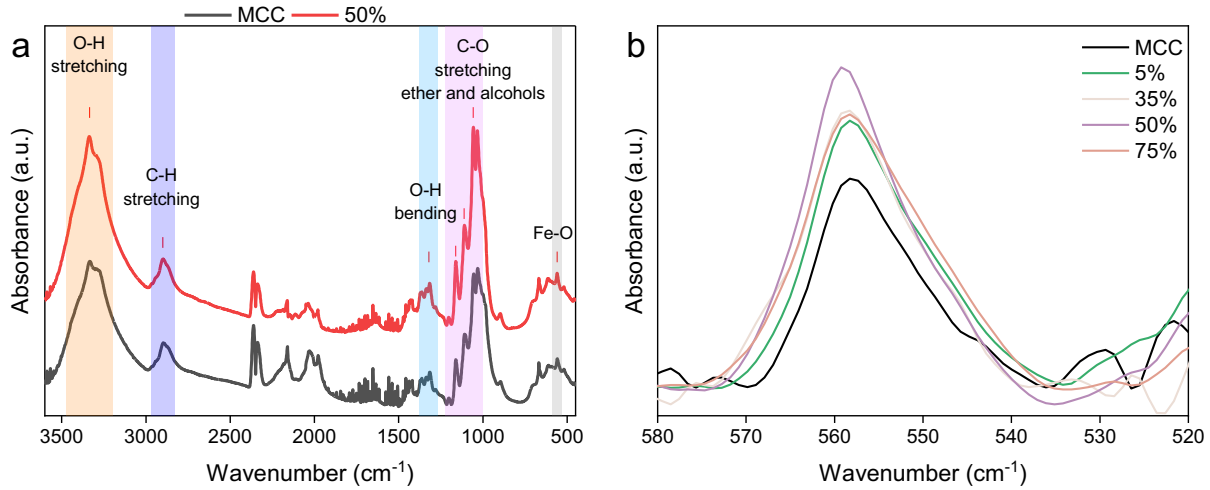


**Figure 2.3.** FTIR characterisation of (a) pristine and Fe modified microcrystalline cellulose, and (b) concentration of iron on microcrystalline cellulose

Thermogravimetric (TGA) analysis was conducted on the samples following the deposition of Fe-based nanoparticles on the cellulose support to quantify the iron content in the adsorbent and asses the achieved iron deposition. Figure 2.4a depicts a typical TGA curve obtained when combusting the adsorbent samples under air up to 1 000°C. A steep drop in mass is observed around 300°C from the degradation of the cellulose support. The amount of deposited iron can be quantified from the leftover mass of the sample. As the measurement is performed under air, the iron is completely oxidised to $Fe_2O_3$ under these conditions [62,63] and the leftover mass is corrected to account only for iron as no ash remained from the combustion of pristine MCC.

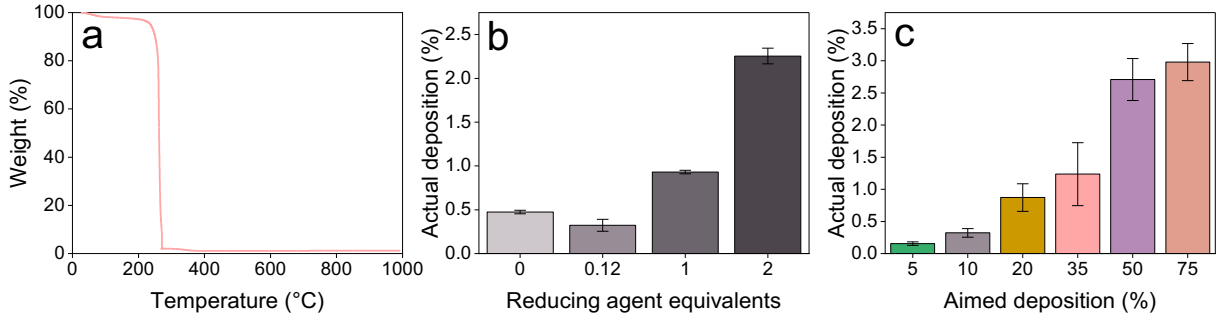


**Figure 2.4.** (a) Typical TGA degradation curve of adsorbent and the actual iron deposition in the adsorbent based on (b) the amount of reducing agent and (c) the aimed deposition

Figure 2.4b compares the mass of iron measured in each adsorbent for the various stoichiometric ratios of reducing agent used (adsorbents 1-4, table 2.1). When no reducing agent was used, 0.47 wt% of iron was measured in the sample although none was expected. When green tea was used as the reducing agent, the deposited mass of iron increased with the stoichiometric ratio. Using the reference volume of green tea (0.04 equivalents), 0.32 wt% of iron was deposited. When using 1 equivalent and 2 equivalents of reducing agent, respective iron contents of 0.93 wt% and 2.25 wt% were measured in the samples. Figure 2.4c compiles the leftover iron in the samples as a function of the aimed iron deposition (adsorbents 11-14, table 2.1). As expected, the actual amount of iron deposited on the sample increased when the aim was increased. The actual depositions ranged from 0.16 wt% to 2.98 wt% when aims varied from 5 wt% to 75 wt.%.

It was observed that as the aimed deposition increased, the material's colour varied from white to black as expected since the iron concentration in the adsorbent increased (figure 2.5). On the other hand, when no reducing agent was used the retrieved powder maintained the orange

appearance observed in the iron nitrate precursor salt solution. A colour change from orange to black is indicative of the reduction of iron and nanoparticle formation. XRD analysis and SEM imaging were carried out to assess if there was a change in the chemical speciation of the iron depending on the amount of reducing agent used.

SEM was used to compare the morphology of the above-described adsorbents: pristine MCC, MCC modified with iron using no reducing agent, 0.04 equivalents and 2 equivalents of reducing agent. As seen on figure 2.5a, pristine MCC has a mostly uniform size with some larger particles being observed. In both cases where no reducing agent was used (figure 2.5b-c), agglomerates were observed from the presence of particles which appear as white on the images due to a different mode of electron scattering (circled). Localised EDS was performed on these particles and showed that they contained iron above the iron concentration measured by TGA (see supplementary information). When EDS was performed on surrounding MCC particles, no iron was identified. This would indicate a weak deposition process when no reducing agent was used as the iron clusters were simply recovered with the MCC from a precipitation during the deposition process. There is no uniform deposition otherwise iron would have been measured on the MCC as well and not be limited to the clusters. When a larger deposition volume is used (figure 2.5c) this difference between iron clusters and cellulose particles is even more pronounced and can be observed from the contrasting white and darker particles as circled on the image.

In the case when 0.04 equivalents of green tea were used as a reducing agent, the morphology of the sample was very similar to that of pristine MCC. No iron clusters were observed on the images indicating a uniform deposition with limited agglomeration on the support. Localised EDS was also performed on this sample and iron was detected in all the particles, again supporting the successful deposition of the nanoparticles. However, when 2 equivalents were used, some agglomeration was obvious from the presence of very large iron clusters which were confirmed by localised EDS (circled on figure 2.5e). These agglomerates are probably a result of an excess of nanoparticles and the inability for the cellulose to stabilise them all. As such, agglomerates were formed and precipitated out of the solution during the deposition process. They were then recovered with the adsorbent which would explain the much darker colour of this adsorbent. A black layer of Fe-based nanoparticles was also observed on top of this adsorbent after the centrifugation process which further supports the hypothesis of agglomeration of the nanoparticles and the precipitation of these clusters.

Figure 2.5f-i shows the XRD patterns of pristine MCC and MCC modified with iron using different amounts of green tea. When no reducing agent was used (figure 2.5g-h) the adsorbent had an orange colour. By simply increasing the total volume used when the deposition was carried out, the amount of iron recovered in the sample increased significantly (see supporting information) and the XRD pattern corresponded to that of FeO(OH). This iron hydroxide was expected to be formed when no reducing agent was used as the $Fe^{3+}$ ions are hydrolysed by water to form the hydroxide when no reducing agent is present [64]. It is hypothesized that the chemical speciation of the iron is the same when a "standard" volume is used to perform the deposition, as the reaction conditions are otherwise identical. However, this could not be confirmed by XRD as the iron content was too low for the signals to be distinguished from the one of MCC (figure 2.5g). In the cases when 0.04 equivalents and 2 equivalents of green tea were used, the oxidation state of the iron could not be resolved by XRD (figure 2.5i-j). For both these cases, the strong amorphous signal of MCC, which results in very broad peaks, likely overlapped with those of the Fe-based nanoparticles. This phenomenon is further accentuated by the nano nature of the particles. Indeed, nanoparticles exhibit weaker and broader signals by XRD as they produce more scattered diffraction [65].

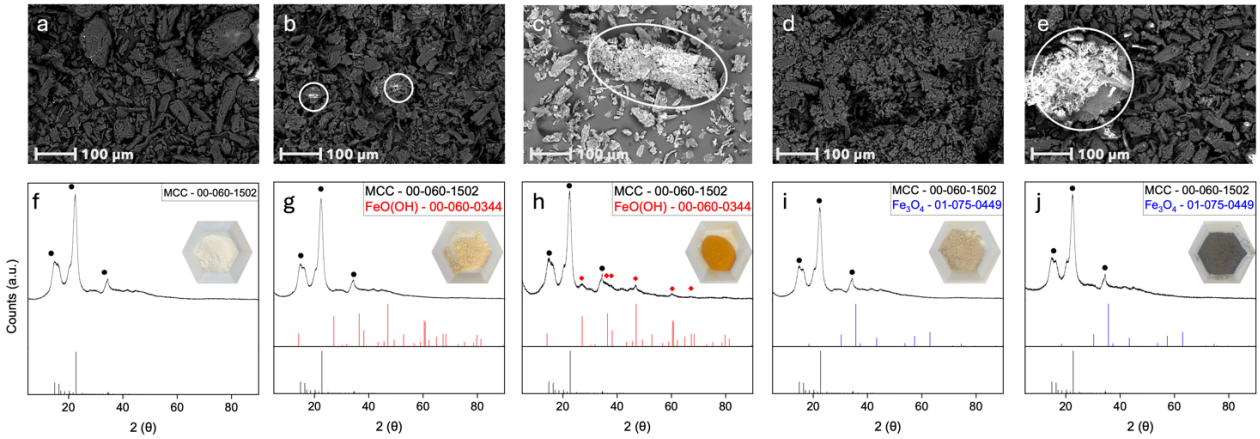


**Figure 2.5.** SEM images of (a) pristine MCC and MCC modified with iron using (b) no reducing agent, (c) no reducing agent using the same total volume as when using 2 equivalents (d) 0.04 equivalents of reducing agent and (e) 2 equivalents of reducing agent. XRD patterns of the adsorbents with (f) pristine MCC, (g) no reducing agent, (h) no reducing agent using the same total volume as when using 2 equivalents, (i) 0.04 equivalents of reducing agent and (j) 2 equivalents of reducing agent.

Transmission electron microscopy (TEM) was used to determine the size of the Fe-based nanoparticles and the chemical speciation of the iron after the plant-based reduction. The chemical speciation could not be determined by XRD when the nanoparticles were deposited on MCC, and SEM did not provide sufficient resolution to distinguish the nanoparticles from the support. Therefore, a suspension of nanoparticles on their own was prepared for TEM imaging. Figures 2.6a and 2.6b show the nanoparticles produced by this method are spherical and have an average size of about 10 nm. Nanoparticles were delimited by either a change in the diffraction pattern or the presence of an amorphous section surrounding a diffraction pattern. When either of these were observed, it was considered as the delimitation between the particle and the background. Selected area electron diffraction (SAED) was performed on these particles to determine the chemical speciation of the iron since it could not be determined through XRD. Although this reduction has already been reported, there does not seem to be a consensus in the literature as for the chemical speciation of the iron with both zero-valent iron [66] and iron oxide [67] being reported. SAED patterns are found on figures 2.6c and 2.6d, and their reconstruction allowed to identify the oxidation of iron as corresponding to magnetite, or $Fe_3O_4$ (see supplementary information for details).

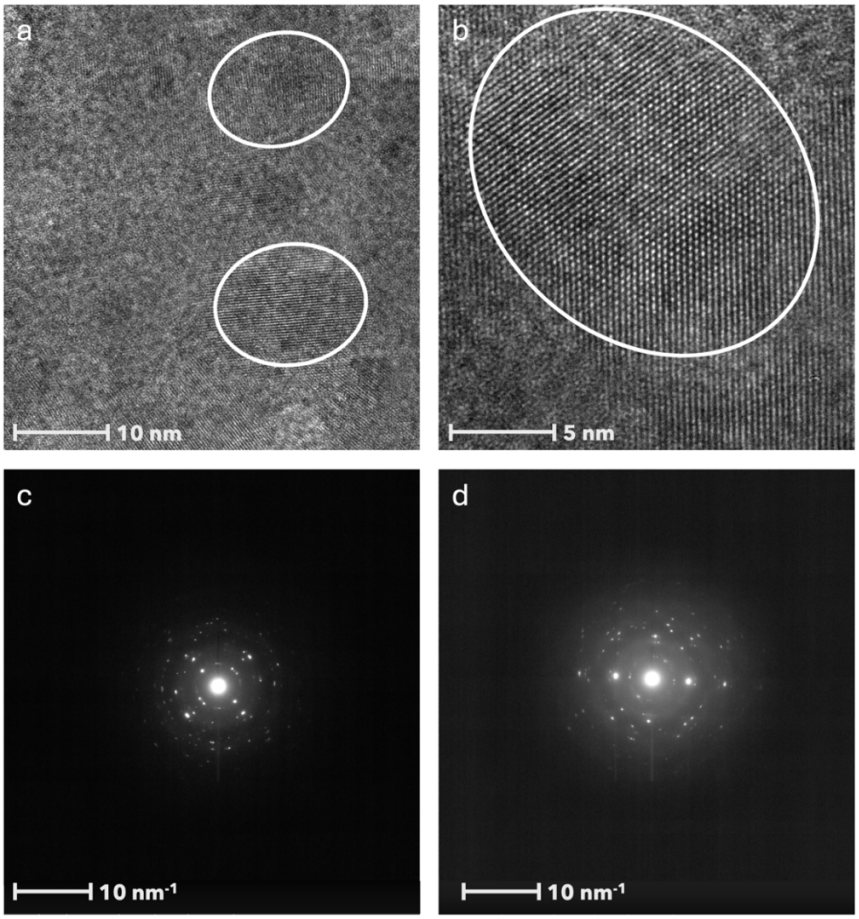


**Figure 2.6.** TEM images of (a,b) $Fe_3O_4$ nanoparticles after reduction with green tea and (c,d) SAED patterns of the nanoparticles

STEM imaging and EDS mapping were used to compare the morphology of both types of support, namely MCC and NCC, and determine if an iron deposition pattern was observed. Figure 2.7 compares high-angle annular dark field (HAADF) images and EDS maps from both types of support. From the HAADF images, it is apparent that the NCC support is much smaller, and the expected fibrous nature of the support was observed (figure 2.7a). Some denser particles were dispersed across the sample as seen by the white particles on the image. Although they could appear as agglomerates of $Fe_3O_4$ nanoparticles, both EDS mapping (figure 2.7c) and localised EDS measurement (see supplementary information) did not show any localised increase in the iron concentration in these specific locations compared to the rest of the sample. EDS mapping did not show any preferred orientation or location for the $Fe_3O_4$ nanoparticles to deposit on. Iron was observed across the entirety of the sample image and was not only with the cellulose fibers. This indicated that the iron recovered in this sample was not effectively stabilised by the NCC. MCC, on the other hand, is a significantly larger support and is much more amorphous in nature when

compared to NCC (figure 2.7b). Indeed, the amorphous domains of the biopolymer contain chains entangled together, without any chemical interaction. On the other hand, crystalline domains will likely be characterised by strong hydrogen bonding between the hydroxyls. In such case, the hydroxyls would be less available to stabilise $Fe_3O_4$ nanoparticles, thus leading to a weaker deposition. The weaker deposition process observed on NCC could result from this phenomenon as it contains more crystalline domains than MCC. EDS mapping was performed in various locations across the adsorbent and iron was systematically observed exclusively on the MCC (figure 2.7d). This would indicate that the $Fe_3O_4$ nanoparticles were preferentially deposited on the surface of the MCC as desired, and no un-stabilised $Fe_3O_4$ nanoparticles were left in the sample.

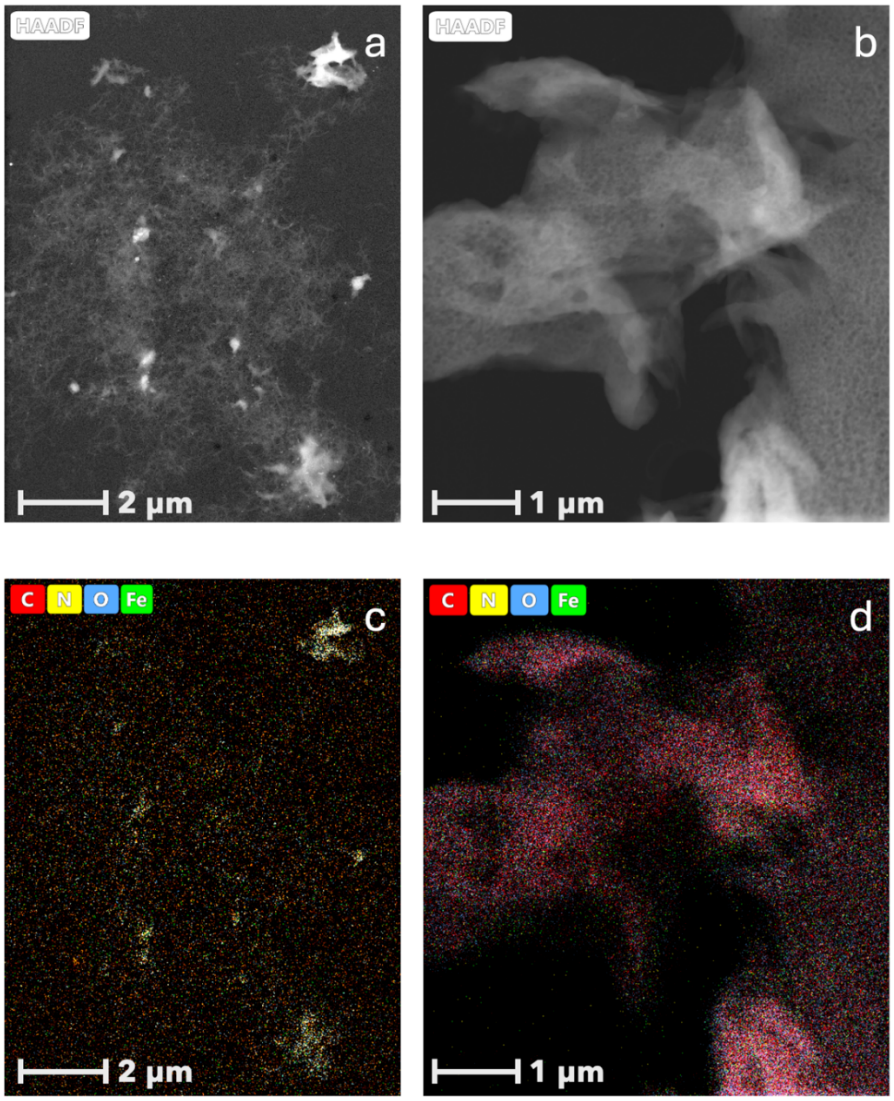


**Figure 2.7.** HAADF images of (a) NCC based adsorbent and (b) MCC based adsorbent. EDS maps of (c) NCC based adsorbent and (d) MCC based adsorbent

### 2.3.4. $SO_2$ capture experiments

Breakthrough experiments were performed to investigate the affinity of the adsorbents for $SO_2$ and measure their adsorption capacities. Each series of breakthrough experiments were designed to evaluate a specific impact in the synthesis conditions and assess its importance in the adsorbent's performance. Breakthrough times and adsorption capacities of the adsorbents were evaluated when the outlet concentration reached 1 ppm $SO_2$. They are presented in figure 2.8. As mentioned in the experimental section, blank experiments were performed to establish the experimental saturation concentration of the packed bed reactor (PBR) which was measured at 23 ppm $SO_2$ (slightly lower than the concentration advertised by the supplier). This value was used to normalize the experimental results. The blank and the pristine MCC breakthrough curves are also shown on each plot as reference curves. All the $SO_2$ capture experiments were performed up to the saturation point.

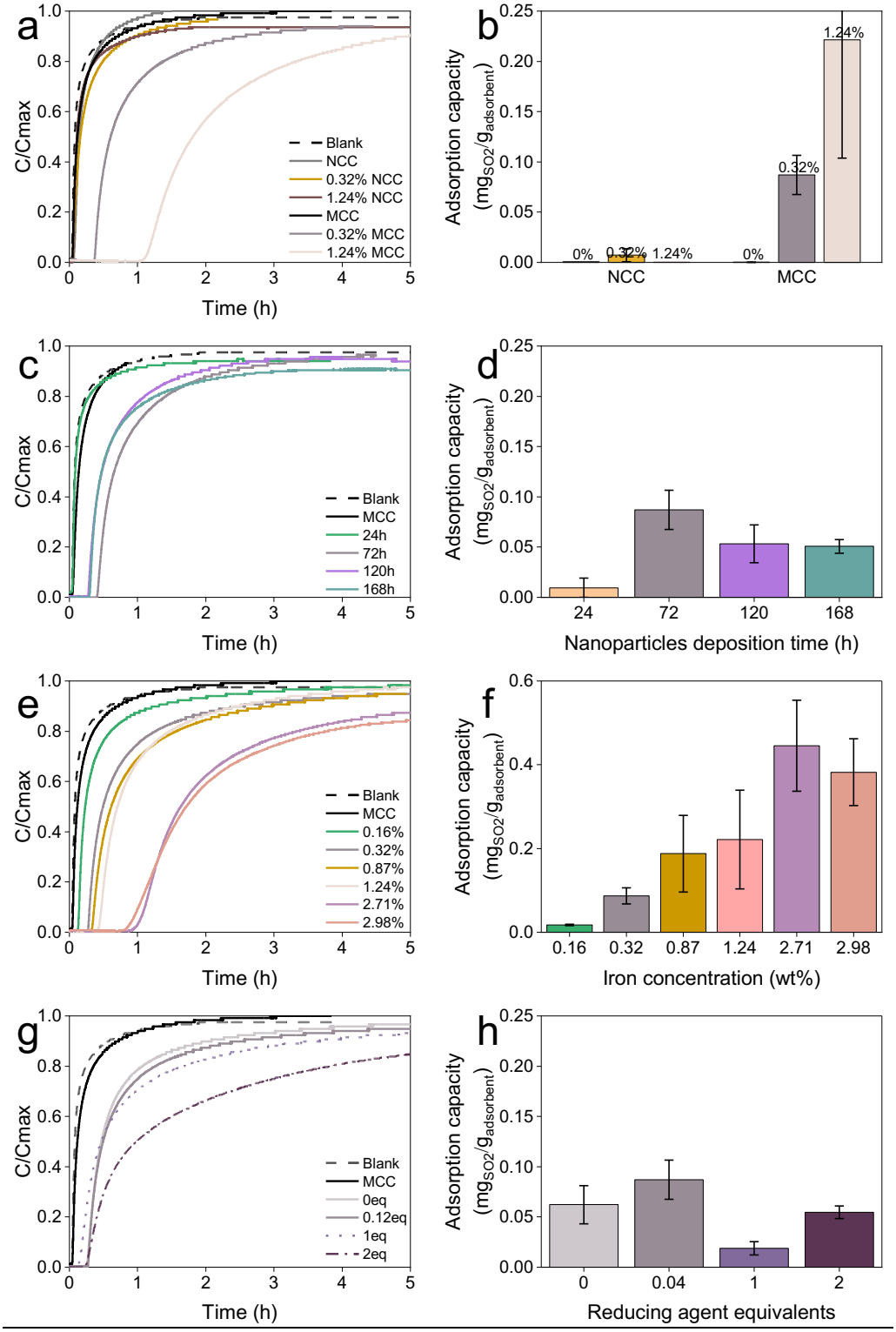


**Figure 2.8.** Breakthrough curves and adsorption capacities in terms of mass of adsorbent to assess the effect of (a,b) the nature of the support, (c,d) the deposition time, (e,f) the aimed deposition and (g,h) the amount of reducing agent. Capture experiments were conducted with 100mg of adsorbent, a flow rate of 10 mL/min and at room temperature. The adsorption capacity was evaluated at 1 ppm. The percentages represent iron concentration in the adsorbents (wt%). For columns with error bars, n=3.

#### 2.3.4.1. Impact of the type of cellulose support

Nanocrystalline cellulose and microcrystalline cellulose were compared as supports for the iron nanoparticles. Both types of cellulose showed low adsorption capabilities in their pristine form, with breakthrough times of 3.0 minutes for both NCC and MCC. This corresponded to an adsorption capacity of $3.8\times10^{-4}$ $mg_{SO_2}/g_{adsorbent}$. Modification of the support with $Fe_3O_4$ nanoparticles increased the adsorption capabilities and therefore resulted in an increase in breakthrough time. To assess the effect of the nature of the support, two different deposition concentrations of 0.32 wt% and 1.24 wt% were selected for each support and compared between their counterpart and the raw supports. As seen on figure 2.8a-b, modifying NCC with either 0.32 wt% or 1.24 wt% of $Fe_3O_4$ nanoparticles had no significant impact on the affinity of the adsorbent for $SO_2$. Indeed, breakthrough times marginally increased to 5.4 and 3.5 minutes respectively for 0.32 wt% and 1.24 wt% which corresponds to adsorption capacities of $7.2\times10^{-3}$ $mg_{SO_2}/g_{adsorbent}$ and $1.2\times10^{-3}$ $mg_{SO_2}/g_{adsorbent}$. This indicated that NCC was not a suitable candidate for this specific application as even modification of the material did not lead to any increase in adsorption. On the contrary, modification of MCC with $Fe_3O_4$ nanoparticles substantially increased the capture potential of the adsorbent, with breakthrough time increasing to 21.7 minutes for 0.32 wt% (capture capacity of 0.087 $mg_{SO_2}/g_{adsorbent}$) and 46.6 minutes for 1.24 wt% (capture capacity of 0.22 $mg_{SO_2}/g_{adsorbent}$). This represents an increase in capture capacity of 225 times for 0.32 wt% and 577 times for 1.24 wt%. This increase is probably a result of the localized deposition of $Fe_3O_4$ nanoparticles on MCC which was not the case on NCC. With the nanoparticles being attached to the support, they can act synergistically in the adsorption process.

#### 2.3.4.2. Nanoparticle deposition time impact

The second parameter investigated for its impact on the adsorption capacities was the time of the deposition of $Fe_3O_4$ nanoparticles on the MCC during the synthesis. To evaluate this, various adsorbents with an aimed iron deposition of 10 wt% were synthesized. $Fe_3O_4$ nanoparticles were stirred with the MCC for durations varying from 24 hours (1 day) to 168 hours (7 days) in increments of 48 hours. It is obvious that a 24-hour deposition was insufficient to ensure adequate deposition on the support as seen in figure 2.8c-d. Indeed for 24 hours of deposition, the synthesized adsorbent performed similarly to MCC meaning with a breakthrough time of 5.6 minutes and an adsorption capacity of $9.6\times10^{-3}$ $mg_{SO_2}/g_{adsorbent}$. This would indicate that the

deposition is slow and is limited by surface interactions between the magnetite nanoparticles and the support. When the deposition time was of 72 hours, the breakthrough time increased to 21.7 minutes and the associated adsorption capacity was 0.087 $mg_{SO_2}/g_{adsorbent}$. This significant improvement confirmed that the deposition process did take place, but at a slow rate. When the deposition time was increased further to 120 hours (5 days) and 168 hours (7 days) no significant improvement were observed in either case. For both depositions the breakthrough times were of 16.3 minutes and 16.1 minutes respectively which are both lower than the 21.7 minutes achieved with 72 hours deposition. The adsorption capacities also decreased to 0.053 $mg_{SO_2}/g_{adsorbent}$ and 0.051 $mg_{SO_2}/g_{adsorbent}$. The lack of improvement could result from an equilibrium being achieved after the 72 hours deposition as the nanoparticles are only physically retained on the surface of the cellulose and can return in suspension. A deposition time of 72 hours was selected as being the optimal between the four deposition times investigated and was kept for further syntheses.

#### 2.3.4.3. Impact of iron content on adsorption capacity

To assess the importance of iron in the $SO_2$ capture process, various adsorbents were synthesized with different iron contents. To achieve this, the concentration of the iron nitrate precursor salt was varied for each sample to aim for a desired final iron content as reported in adsorbents 11-14 of table 2.1. The volume of green tea was modified accordingly while maintaining a constant ratio of volume of green tea over the aimed deposition as for the reference conditions (adsorbent 1). Although the measured iron concentration in the samples was lower than the aimed deposition, as observed by TGA analysis, an increase in the iron content of the samples was proportionally obtained while increasing the precursor concentration. As seen on figure 2.8e-f, there was an increase in the capture capacity compared to pristine MCC immediately when iron was deposited on the surface with the breakthrough time increasing to 7.7 minutes and the adsorption capacity to 0.017 $mg_{SO_2}/g_{adsorbent}$ with an iron content of only 0.16 wt%. Increasing the iron content in the adsorbent systemically increased the adsorption capacity of the material thus confirming that $Fe_3O_4$ nanoparticles played a key role in the process. This effect seemed to plateau past an iron concentration of 2.71 wt% which resulted in a breakthrough time of 83.6 minutes and an adsorption capacity of 0.45 $mg_{SO_2}/g_{adsorbent}$. When an iron concentration of 2.98 wt% was measured, the breakthrough time and the adsorption capacity decreased to 70.3 minute and 0.38 $mg_{SO_2}/g_{adsorbent}$ respectively. The difference is not significant enough to confidently differentiate

the two, hence why a plateau effect is proposed. This could be a result of a less uniform deposition resulting in a decrease of interface between MCC and the nanoparticles as well as less iron surface available for the adsorption.

#### 2.3.4.4. Impact of the amount of reducing agent on adsorption

The last parameter monitored was the impact of the amount of reducing agent used to generate the nanoparticles (figure 2.8g-h). The aim was to confirm whether the nanoparticles maintained their ability to capture $SO_2$ when 1 or 2 equivalents of green tea were used as reducing agent although some agglomeration of $Fe_3O_4$ particles had been observed by SEM in these adsorbents. Although using more green tea resulted in a higher iron content in the adsorbents (measured by TGA), the adsorption capacities decreased in both cases. Indeed, breakthrough times decreased from 21.7 minutes (observed when using 0.04 equivalents of green tea) to 9.4 minutes and 16.5 minutes as the conditions were modified from using the reference volume of green tea to using 1 and 2 equivalents respectively. In terms of capture capacities, this meant a decrease from 0.087 $mg_{SO_2}/g_{adsorbent}$ to 0.025 $mg_{SO_2}/g_{adsorbent}$ and 0.061 $mg_{SO_2}/g_{adsorbent}$. This showed that the iron being recovered in these samples was not able to efficiently interact with $SO_2$ and favor its adsorption. This was likely due to the nanoparticles having agglomerated under these conditions as observed by SEM. There was an increase in $SO_2$ capture when comparing the 2-equivalent to the 1-equivalent sample, but the former contained over 2 times more iron hence its adsorption capacity should increase. When no reducing agent was used, $SO_2$ adsorption was still observed although the iron was not in the same chemical speciation as when reduced. Indeed it was shown by XRD that FeO(OH) was present in this adsorbent. This form of iron did not perform as well as the $Fe_3O_4$ nanoparticles which is shown by the lower breakthrough time of 16.7 minutes and capture capacity of 0.062 $mg_{SO_2}/g_{adsorbent}$. Using a sub stoichiometric amount of reducing agent yielded the adsorbent for which the nanoparticles had the highest affinity for $SO_2$.

#### 2.3.4.5. Adsorption capacity as function of iron content

To further quantify the effectiveness of the $Fe_3O_4$ nanoparticles in increasing the adsorption of $SO_2$, adsorption capacities for each adsorbent were expressed per mass of iron rather than per mass of adsorbent. This allows to compare the three types of iron oxides observed across the adsorbents – $Fe_3O_4$ nanoparticles, agglomerated $Fe_3O_4$ and FeO(OH). Figure 2.9 depicts how these

capacities vary as the nature of the iron changes. This is achieved by modifying the amount of reducing agent used. Comparing the adsorbent where no reducing agent was used to the one where 0.04 equivalents of reducing agent were used (adsorbents 1 and 4), it is obvious that the $Fe_3O_4$ nanoparticles have a higher affinity towards $SO_2$ than the FeO(OH) particles. Indeed, the capacity doubled going from 12.0 $mg_{SO_2}/g_{Fe}$ to 24.6 $mg_{SO_2}/g_{Fe}$ when using 0.04 equivalents of green over no reducing agent. This is a clear confirmation that the iron speciation influences the adsorption capacity. The adsorbents synthesized by using 1 and 2 equivalents of green tea showed agglomeration of the $Fe_3O_4$ particles by SEM. A significant decrease of capture capacity was observed for both these adsorbents compared to when 0.04 equivalents of green tea were used. Both performed similarly with a capacity of 2.7 $mg_{SO_2}/g_{Fe}$ which is a decrease of one order of magnitude compared to the capacity of 24.6 $mg_{SO_2}/g_{Fe}$ which was measured for the sample synthesized with 0.04 equivalents of green tea. A decrease in adsorption is to be expected when nanoparticles agglomerate as they provide less surface area and loose some reactivity specific to their nano form. This goes to show that synthesis conditions for the adsorbent must be carefully chosen to achieve the optimal material for this specific application.

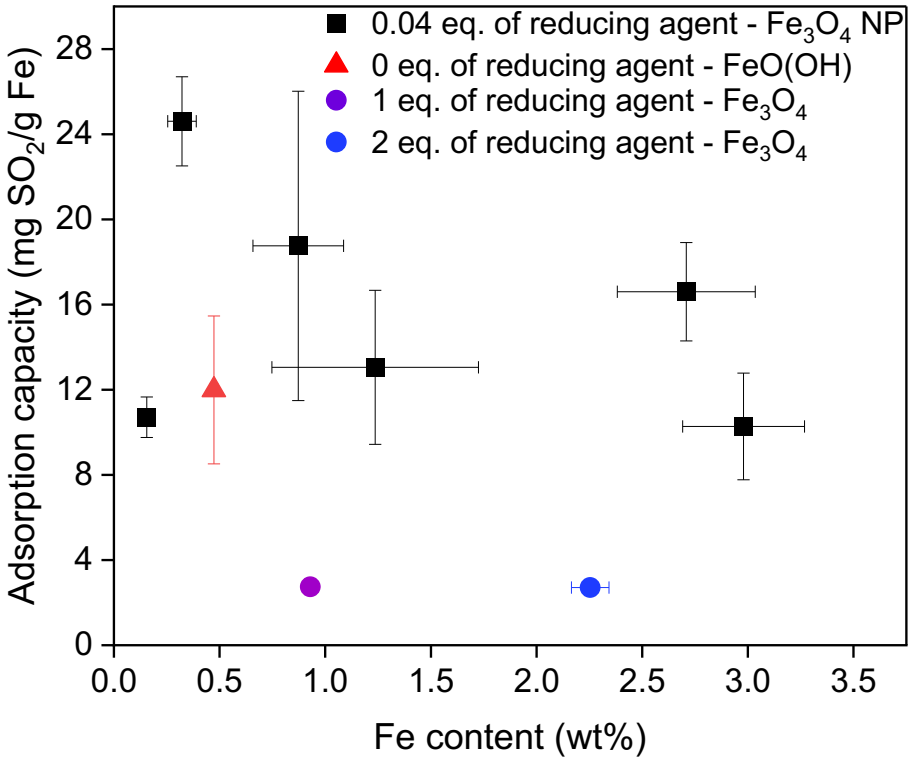


**Figure 2.9.** Adsorption capacities in terms of mass of iron depending on the volume of reducing agent used

The capacities were also compared across the adsorbents for which the aimed deposition of iron was varied while maintaining the standard volume of reducing agent. Among those adsorbents the iron remains in the form of $Fe_3O_4$ nanoparticles and solely the impact of the concentration of magnetite in the sample is compared. Across the samples, an optimum was achieved between a 0.3 wt% and 1.0 wt% of iron on the support. This type of phenomenon is common when depositing nanoparticles on a support as a balance between the presence of $Fe_3O_4$ nanoparticles, sufficient surface area and interface is achieved. By not reaching this optimum, as is the case with less then 0.3 wt%, or by going pass this optimum, as with all the adsorbents with concentrations over 1.0 wt%, one of the components starts having a negative impact which decreases the adsorption capacity. It is interesting to note that the capacities for the depositions using the standard volume of reducing agent which have an iron content of 2.7 wt% and 3.0 wt% are both significantly higher than that of the adsorbent synthesized using 2 equivalents of reducing agent (2.3 wt%) although they contained similar amounts of iron. Indeed, the mass of iron in the adsorbent containing 2.7 wt% was only 1.2 times higher and the mass of iron in the adsorbent containing 3.0 wt% was 1.3 times higher than that of the adsorbent synthesized with 2 equivalents of reducing agent. However, the capacities increased respectively by 6.0 times and 3.8 times. This further demonstrates the critical nature of the $Fe_3O_4$ particle agglomeration in the $SO_2$ adsorption process.

## 2.4. Conclusion

$Fe_3O_4$ nanoparticles were synthesized by using a green tea extract and were deposited on NCC and MCC. This yielded new, sustainable adsorbents used for the first time in the capture of 25 ppm $SO_2$ in Ar. FTIR was used to monitor the deposition of magnetite nanoparticles on the cellulose and TGA to assess the effective quantity deposited on the support. STEM imaging showed that the deposition process was more efficient on the MCC than the NCC support. Adsorbents were synthesized using 0, 0.04, 1 and 2 equivalents of green tea as the reducing agent. SEM imaging showed some agglomeration of the $Fe_3O_4$ nanoparticles when 0 and 2 equivalents of green tea were used. XRD was used to confirm the chemical speciation of the iron when no reducing agent was used. FeO(OH) was observed under this condition which differs from $Fe_3O_4$ observed by SAED when using the green tea reduction.

Adsorbent synthesis parameters were varied to evaluate their influence in the adsorption process. Namely, the type of the cellulose (NCC or MCC), the deposition time, the concentration of $Fe_3O_4$ nanoparticles and the chemical speciation of the iron were investigated. Their impact was measured by breakthrough experiments. NCC was inefficient for this application and MCC required deposition of $Fe_3O_4$ nanoparticles by using 0.04 equivalents of green tea as reducing agent. A 72-hour deposition time with an iron concentration of 0.32 wt% resulted in a capture capacity of 0.087 $mg_{SO_2}/g_{adsorbent}$, which is 225 times increase compared to pristine MCC. As the iron content increased in the adsorbent, the adsorption also increased, indicative that the $Fe_3O_4$ nanoparticles were key in this process. The adsorption capacity per mass of iron in the adsorbent was maximal around a deposition of 0.3 wt% - 1 wt%. When no reducing agent was used, FeO(OH) was present in the adsorbent and the capture capacity decreased by nearly 50%. When 1 and 2 equivalents of green tea were used, agglomerated $Fe_3O_4$ particles were observed in the adsorbents and the capture capacities decreased by an order of magnitude compared to when 0.04 equivalents were used. In summary, $Fe_3O_4$ nanoparticles supported on MCC proved to be an effective and sustainable adsorbent for the capture of trace concentrations (25ppm) of $SO_2$.

# References


[1] Khalaf, E. M.; Mohammadi, M. J.; Sulistiyani, S.; Ramírez-Coronel, A. A.; Kiani, F.; Jalil, A. T.; Almulla, A. F.; Asban, P.; Farhadi, M.; Derikondi, M. Effects of Sulfur Dioxide Inhalation on Human Health: A Review. *Rev. Environ. Health* **2024**, *39* (2), 331–337. https://doi.org/10.1515/reveh-2022-0237.

[2] US EPA, O. *Clean Air Act Requirements and History*. https://www.epa.gov/clean-air-act-overview/clean-air-act-requirements-and-history (accessed 2024-12-09).

[3] Klimont, Z.; Smith, S. J.; Cofala, J. The Last Decade of Global Anthropogenic Sulfur Dioxide: 2000-2011 Emissions. *Environ. Res. Lett.* **2013**, *8* (1), 014003. https://doi.org/10.1088/1748-9326/8/1/014003.

[4] Srivastava, R. K.; Jozewicz, W. Flue Gas Desulfurization: The State of the Art. *J. Air Waste Manag. Assoc.* **2001**, *51* (12), 1676–1688. https://doi.org/10.1080/10473289.2001.10464387.

[5] Wet_and_dry_scrubbers_section_5_chapter_1_control_cost_manual_7th_edition.Pdf. https://www.epa.gov/sites/default/files/2021-05/documents/wet_and_dry_scrubbers_section_5_chapter_1_control_cost_manual_7th_edition.pdf (accessed 2024-12-09).

[6] Hanif, M. A.; Ibrahim, N.; Abdul Jalil, A. Sulfur Dioxide Removal: An Overview of Regenerative Flue Gas Desulfurization and Factors Affecting Desulfurization Capacity and Sorbent Regeneration. *Environ. Sci. Pollut. Res.* **2020**, *27* (22), 27515–27540. https://doi.org/10.1007/s11356-020-09191-4.

[7] An, X.-C.; Li, Z.-M.; Zhou, Y.; Zhu, W.; Tao, D.-J. Rapid Capture and Efficient Removal of Low-Concentration SO2 in Simulated Flue Gas by Hypercrosslinked Hollow Nanotube Ionic Polymers. *Chem. Eng. J.* **2020**, *394*, 124859. https://doi.org/10.1016/j.cej.2020.124859.

[8] Yang, D.; Hou, M.; Ning, H.; Ma, J.; Kang, X.; Zhang, J.; Han, B. Reversible Capture of SO2 through Functionalized Ionic Liquids. *ChemSusChem* **2013**, *6* (7), 1191–1195. https://doi.org/10.1002/cssc.201300224.

[9] Cui, G.; Zhao, N.; Li, Y.; Wang, H.; Zhao, Y.; Li, Z.; Wang, J. Limited Number of Active Sites Strategy for Improving SO2 Capture by Ionic Liquids with Fluorinated Acetylacetonate Anion. *ACS Sustain. Chem. Eng.* **2017**, *5* (9), 7985–7992. https://doi.org/10.1021/acssuschemeng.7b01551.

[10] Gong, W.-Q.; Wu, X.-L.; Li, Z.-M.; Zhou, Y.; Zhu, W.; Tao, D.-J. Sulfate Ionic Liquids Impregnated 2D Boron Nitride Nanosheets for Trace SO2 Capture with High Capacity and Selectivity. *Sep. Purif. Technol.* **2021**, *270*, 118824. https://doi.org/10.1016/j.seppur.2021.118824.

[11] Sheng, K.; Li, D.; Kang, Y. Unexpectedly Promoted SO2 Capture in Novel Ionic Liquid-Based Eutectic Solvents: The Synergistic Interactions. *J. Mol. Liq.* **2021**, *337*, 116432. https://doi.org/10.1016/j.molliq.2021.116432.

[12] Jiang, B.; Zhang, H.; Zhang, L.; Zhang, N.; Huang, Z.; Chen, Y.; Sun, Y.; Tantai, X. Novel Deep Eutectic Solvents for Highly Efficient and Reversible Absorption of SO2 by Preorganization Strategy. *ACS Sustain. Chem. Eng.* **2019**, *7* (9), 8347–8357. https://doi.org/10.1021/acssuschemeng.8b06822.

[13] Zhu, J. L.; Wang, Y. H.; Zhang, J. C.; Ma, R. Y. Experimental Investigation of Adsorption of NO and SO2 on Modified Activated Carbon Sorbent from Flue Gases. *Energy Convers. Manag.* **2005**, *46* (13), 2173–2184. https://doi.org/10.1016/j.enconman.2004.10.011.

[14] Li, Z.; Liu, Y.; Wang, H.; Tsai, C.-J.; Yang, X.; Xing, Y.; Zhang, C.; Xiao, P.; Webley, P. A. A Numerical Modelling Study of SO2 Adsorption on Activated Carbons with New Rate Equations. *Chem. Eng. J.* **2018**, *353*, 858–866. https://doi.org/10.1016/j.cej.2018.07.119.

[15] Karatepe, N.; Orbak, İ.; Yavuz, R.; Özyuğuran, A. Sulfur Dioxide Adsorption by Activated Carbons Having Different Textural and Chemical Properties. *Fuel* **2008**, *87* (15), 3207–3215. https://doi.org/10.1016/j.fuel.2008.06.002.

[16] Gupta, A.; Gaur, V.; Verma, N. Breakthrough Analysis for Adsorption of Sulfur-Dioxide over Zeolites. *Chem. Eng. Process. Process Intensif.* **2004**, *43* (1), 9–22. https://doi.org/10.1016/S0255-2701(02)00213-1.

[17] Deng, H.; Yi, H.; Tang, X.; Yu, Q.; Ning, P.; Yang, L. Adsorption Equilibrium for Sulfur Dioxide, Nitric Oxide, Carbon Dioxide, Nitrogen on 13X and 5A Zeolites. *Chem. Eng. J.* **2012**, *188*, 77–85. https://doi.org/10.1016/j.cej.2012.02.026.

[18] Dai, Z.; Chen, W.; Kan, X.; Li, F.; Bao, Y.; Zhang, F.; Xiong, Y.; Meng, X.; Zheng, A.; Xiao, F.-S.; Liu, F. Stable Porous Organic Polymers Used for Reversible Adsorption and Efficient Separation of Trace SO2. *ACS Macro Lett.* **2022**, *11* (8), 999–1007. https://doi.org/10.1021/acsmacrolett.2c00320.

[19] Ren, Y.-B.; Xu, H.-Y.; Gang, S.-Q.; Gao, Y.-J.; Jing, X.; Du, J.-L. An Ultra-Stable Zr(IV)-MOF for Highly Efficient Capture of SO2 from SO2/CO2 and SO2/CH4 Mixtures. *Chem. Eng. J.* **2022**, *431*, 134057. https://doi.org/10.1016/j.cej.2021.134057.

[20] Xing, S.; Liang, J.; Brandt, P.; Schäfer, F.; Nuhnen, A.; Heinen, T.; Boldog, I.; Möllmer, J.; Lange, M.; Weingart, O.; Janiak, C. Capture and Separation of SO2 Traces in Metal–Organic Frameworks via Pre-Synthetic Pore Environment Tailoring by Methyl Groups. *Angew. Chem. Int. Ed.* **2021**, *60* (33), 17998–18005. https://doi.org/10.1002/anie.202105229.

[21] Carter, J. H.; Han, X.; Moreau, F. Y.; da Silva, I.; Nevin, A.; Godfrey, H. G. W.; Tang, C. C.; Yang, S.; Schröder, M. Exceptional Adsorption and Binding of Sulfur Dioxide in a Robust Zirconium-Based Metal–Organic Framework. *J. Am. Chem. Soc.* **2018**, *140* (46), 15564–15567. https://doi.org/10.1021/jacs.8b08433.

[22] Zhang, S.; Wang, L.; Zhang, Y.; Cao, F.; Sun, Q.; Ren, X.; Wennersten, R. Effect of Hydroxyl Functional Groups on SO2 Adsorption by Activated Carbon. *J. Environ. Chem. Eng.* **2022**, *10* (6), 108727. https://doi.org/10.1016/j.jece.2022.108727.

[23] Chen, C.; Xu, K.; Ji, X.; Miao, L.; Jiang, J. Enhanced Adsorption of Acidic Gases (CO2, NO2 and SO2) on Light Metal Decorated Graphene Oxide. *Phys. Chem. Chem. Phys.* **2014**, *16* (22), 11031–11036. https://doi.org/10.1039/C4CP00702F.

[24] Seddiqi, H.; Oliaei, E.; Honarkar, H.; Jin, J.; Geonzon, L. C.; Bacabac, R. G.; Klein-Nulend, J. Cellulose and Its Derivatives: Towards Biomedical Applications. *Cellulose* **2021**, *28* (4), 1893–1931. https://doi.org/10.1007/s10570-020-03674-w.

[25] Miao, C.; Hamad, W. Y. Cellulose Reinforced Polymer Composites and Nanocomposites: A Critical Review. *Cellulose* **2013**, *20* (5), 2221–2262. https://doi.org/10.1007/s10570-013-0007-3.

[26] Cai, J.; Kimura, S.; Wada, M.; Kuga, S. Nanoporous Cellulose as Metal Nanoparticles Support. *Biomacromolecules* **2009**, *10* (1), 87–94. https://doi.org/10.1021/bm800919e.

[27] Zhao, H.-X.; Li, J.-C.; Wang, Y.; Guo, Y.-R.; Li, S.; Pan, Q.-J. An Environment-Friendly Technique for Direct Air Capture of Carbon Dioxide via a Designed Cellulose and Calcium System. *Sep. Purif. Technol.* **2023**, *307*, 122774. https://doi.org/10.1016/j.seppur.2022.122774.

[28] Campbell, S.; Bernard, F. L.; Rodrigues, D. M.; Rojas, M. F.; Carreño, L. Á.; Chaban, V. V.; Einloft, S. Performance of Metal-Functionalized Rice Husk Cellulose for CO2 Sorption and CO2/N2 Separation. *Fuel* **2019**, *239*, 737–746. https://doi.org/10.1016/j.fuel.2018.11.078.

[29] Zafari, R.; Fauteux-Lefebvre, C. Surface Modification Investigation of Nanocrystalline Cellulose with Combined Functional Groups for Sulfur Dioxide Capture. *Adsorption* **2023**, *29* (3), 151–161. https://doi.org/10.1007/s10450-023-00390-2.

[30] Zafari, R.; Mendonça, F. G.; Tom Baker, R.; Fauteux-Lefebvre, C. Efficient SO2 Capture Using an Amine-Functionalized, Nanocrystalline Cellulose-Based Adsorbent. *Sep. Purif. Technol.* **2023**, *308*, 122917. https://doi.org/10.1016/j.seppur.2022.122917.

[31] Heinze, T. Cellulose: Structure and Properties. In *Cellulose Chemistry and Properties: Fibers, Nanocelluloses and Advanced Materials*; Rojas, O. J., Ed.; Springer International Publishing: Cham, 2016; pp 1–52. https://doi.org/10.1007/12_2015_319.

[32] Eyley, S.; Thielemans, W. Surface Modification of Cellulose Nanocrystals. *Nanoscale* **2014**, *6* (14), 7764–7779. https://doi.org/10.1039/C4NR01756K.

[33] Kamel, S.; Khattab, T. A. Recent Advances in Cellulose Supported Metal Nanoparticles as Green and Sustainable Catalysis for Organic Synthesis. *Cellulose* **2021**, *28* (8), 4545–4574. https://doi.org/10.1007/s10570-021-03839-1.

[34] Lam, E.; Male, K. B.; Chong, J. H.; Leung, A. C. W.; Luong, J. H. T. Applications of Functionalized and Nanoparticle-Modified Nanocrystalline Cellulose. *Trends Biotechnol.* **2012**, *30* (5), 283–290. https://doi.org/10.1016/j.tibtech.2012.02.001.

[35] Kaushik, M.; Moores, A. Review: Nanocelluloses as Versatile Supports for Metal Nanoparticles and Their Applications in Catalysis. *Green Chem.* **2016**, *18* (3), 622–637. https://doi.org/10.1039/C5GC02500A.

[36] S. Chaudhari, D.; P. Upadhyay, R.; Y. Shinde, G.; B. Gawande, M.; Filip, J.; S. Varma, R.; Zbořil, R. A Review on Sustainable Iron Oxide Nanoparticles: Syntheses and Applications in Organic Catalysis and Environmental Remediation. *Green Chem.* **2024**, *26* (13), 7579–7655. https://doi.org/10.1039/D4GC01870B.

[37] Zhao, L.; Li, X.; Zhao, Q.; Qu, Z.; Yuan, D.; Liu, S.; Hu, X.; Chen, G. Synthesis, Characterization and Adsorptive Performance of MgFe2O4 Nanospheres for SO2 Removal. *J. Hazard. Mater.* **2010**, *184* (1), 704–709. https://doi.org/10.1016/j.jhazmat.2010.08.096.

[38] Glover, T. G.; Sabo, D.; Vaughan, L. A.; Rossin, J. A.; Zhang, Z. J. Adsorption of Sulfur Dioxide by CoFe2O4 Spinel Ferrite Nanoparticles and Corresponding Changes in Magnetism. *Langmuir* **2012**, *28* (13), 5695–5702. https://doi.org/10.1021/la3003417.

[39] Pham, X.-M.; Pham, D. L.; Hanh, N. T.; Dang Thi, T. A.; Thuy Giang, L. N.; Phuong, H. T.; Anh, N. T.; Nhung, H. T.; Le, G. T.; Hoang, M. H.; Nguyen, T. V. An Initial Evaluation on the Adsorption of SO2 and NO2 over Porous Fe3O4 Nanoparticles Synthesized by Facile Scalable Method. *J. Chem.* **2019**, *2019* (1), 9742826. https://doi.org/10.1155/2019/9742826.

[40] Jeyapaul, A. S.; Ganesapillai, M. A Sustainable Solution: Mitigating Sulphur Dioxide Emissions through Adsorption on Chemically Modified Iron Oxide Nanoparticles. *Clean Technol. Environ. Policy* **2024**. https://doi.org/10.1007/s10098-024-02807-0.

[41] Ye, C. Z.; Ariya, P. A. Co-Adsorption of Gaseous Benzene, Toluene, Ethylbenzene, m-Xylene (BTEX) and SO2 on Recyclable Fe3O4 Nanoparticles at 0–101% Relative Humidities. *J. Environ. Sci.* **2015**, *31*, 164–174. https://doi.org/10.1016/j.jes.2014.10.019.

[42] Fu, H.; Wang, X.; Wu, H.; Yin, Y.; Chen, J. Heterogeneous Uptake and Oxidation of SO2 on Iron Oxides. *J. Phys. Chem. C* **2007**, *111* (16), 6077–6085. https://doi.org/10.1021/jp070087b.

[43] Arcibar-Orozco, J. A.; Rangel-Mendez, J. R.; Bandosz, T. J. Reactive Adsorption of SO2 on Activated Carbons with Deposited Iron Nanoparticles. *J. Hazard. Mater.* **2013**, *246–247*, 300–309. https://doi.org/10.1016/j.jhazmat.2012.12.001.

[44] LaGrow, A. P.; Besenhard, M. O.; Hodzic, A.; Sergides, A.; Bogart, L. K.; Gavriilidis, A.; Thanh, N. T. K. Unravelling the Growth Mechanism of the Co-Precipitation of Iron Oxide Nanoparticles with the Aid of Synchrotron X-Ray Diffraction in Solution. *Nanoscale* **2019**, *11* (14), 6620–6628. https://doi.org/10.1039/C9NR00531E.

[45] Besenhard, M. O.; LaGrow, A. P.; Hodzic, A.; Kriechbaum, M.; Panariello, L.; Bais, G.; Loizou, K.; Damilos, S.; Margarida Cruz, M.; Thanh, N. T. K.; Gavriilidis, A. Co-Precipitation Synthesis of Stable Iron Oxide Nanoparticles with NaOH: New Insights and Continuous Production via Flow Chemistry. *Chem. Eng. J.* **2020**, *399*, 125740. https://doi.org/10.1016/j.cej.2020.125740.

[46] Huang, K.-C.; Ehrman, S. H. Synthesis of Iron Nanoparticles via Chemical Reduction with Palladium Ion Seeds. *Langmuir* **2007**, *23* (3), 1419–1426. https://doi.org/10.1021/la0618364.

[47] Krishna, J.; Perumal, A. S.; Khan, I.; Chelliah, R.; Wei, S.; Swamidoss, C. M. A.; Oh, D.-H.; Bharathiraja, B. Chapter 6 - Synthesis of Nanomaterials for Biofuel and Bioenergy Applications. In *Nanomaterials*; Kumar, R. P., Bharathiraja, B., Eds.; Academic Press, 2021; pp 97–165. https://doi.org/10.1016/B978-0-12-822401-4.00031-3.

[48] Duan, H.; Wang, D.; Li, Y. Green Chemistry for Nanoparticle Synthesis. *Chem. Soc. Rev.* **2015**, *44* (16), 5778–5792. https://doi.org/10.1039/C4CS00363B.

[49] Iravani, S. Green Synthesis of Metal Nanoparticles Using Plants. *Green Chem.* **2011**, *13* (10), 2638–2650. https://doi.org/10.1039/C1GC15386B.

[50] Hussain, I.; Singh, N. B.; Singh, A.; Singh, H.; Singh, S. C. Green Synthesis of Nanoparticles and Its Potential Application. *Biotechnol. Lett.* **2016**, *38* (4), 545–560. https://doi.org/10.1007/s10529-015-2026-7.

[51] Kupina, S.; Fields, C.; Roman, M. C.; Brunelle, S. L. Determination of Total Phenolic Content Using the Folin-C Assay: Single-Laboratory Validation, First Action 2017.13. *J. AOAC Int.* **2018**, *101* (5), 1466–1472. https://doi.org/10.5740/jaoacint.18-0031.

[52] Ainsworth, E. A.; Gillespie, K. M. Estimation of Total Phenolic Content and Other Oxidation Substrates in Plant Tissues Using Folin–Ciocalteu Reagent. *Nat. Protoc.* **2007**, *2* (4), 875–877. https://doi.org/10.1038/nprot.2007.102.

[53] Saif, S.; Tahir, A.; Chen, Y. Green Synthesis of Iron Nanoparticles and Their Environmental Applications and Implications. *Nanomaterials* **2016**, *6* (11), 209. https://doi.org/10.3390/nano6110209.

[54] Asghar, M. A.; Zahir, E.; Shahid, S. M.; Khan, M. N.; Asghar, M. A.; Iqbal, J.; Walker, G. Iron, Copper and Silver Nanoparticles: Green Synthesis Using Green and Black Tea

Leaves Extracts and Evaluation of Antibacterial, Antifungal and Aflatoxin B1 Adsorption Activity. *LWT* **2018**, *90*, 98–107. https://doi.org/10.1016/j.lwt.2017.12.009.

[55] Huang, L.; Weng, X.; Chen, Z.; Megharaj, M.; Naidu, R. Green Synthesis of Iron Nanoparticles by Various Tea Extracts: Comparative Study of the Reactivity. *Spectrochim. Acta. A. Mol. Biomol. Spectrosc.* **2014**, *130*, 295–301. https://doi.org/10.1016/j.saa.2014.04.037.

[56] Widatalla, H. A.; Yassin, L. F.; Alrasheid, A. A.; Ahmed, S. A. R.; Widdatallah, M. O.; Eltilib, S. H.; Mohamed, A. A. Green Synthesis of Silver Nanoparticles Using Green Tea Leaf Extract, Characterization and Evaluation of Antimicrobial Activity. *Nanoscale Adv.* **2022**, *4* (3), 911–915. https://doi.org/10.1039/D1NA00509J.

[57] Hospodarova, V.; Singovszka, E.; Stevulova, N. Characterization of Cellulosic Fibers by FTIR Spectroscopy for Their Further Implementation to Building Materials. *Am. J. Anal. Chem.* **2018**, *9* (6), 303–310. https://doi.org/10.4236/ajac.2018.96023.

[58] Larkin, P. J. Chapter 6 - IR and Raman Spectra–Structure Correlations: Characteristic Group Frequencies. In *Infrared and Raman Spectroscopy (Second Edition)*; Larkin, P. J., Ed.; Elsevier, 2018; pp 85–134. https://doi.org/10.1016/B978-0-12-804162-8.00006-9.

[59] Namduri, H.; Nasrazadani, S. Quantitative Analysis of Iron Oxides Using Fourier Transform Infrared Spectrophotometry. *Corros. Sci.* **2008**, *50* (9), 2493–2497. https://doi.org/10.1016/j.corsci.2008.06.034.

[60] Salama, W.; El Aref, M.; Gaupp, R. Spectroscopic Characterization of Iron Ores Formed in Different Geological Environments Using FTIR, XPS, Mössbauer Spectroscopy and Thermoanalyses. *Spectrochim. Acta. A. Mol. Biomol. Spectrosc.* **2015**, *136*, 1816–1826. https://doi.org/10.1016/j.saa.2014.10.090.

[61] Chubar, N.; Gerda, V.; Szlachta, M.; Yablokova, G. Effect of Fe Oxidation State (+2 versus +3) in Precursor on the Structure of Fe Oxides/Carbonates-Based Composites Examined by XPS, FTIR and EXAFS. *Solid State Sci.* **2021**, *121*, 106752. https://doi.org/10.1016/j.solidstatesciences.2021.106752.

[62] Li, Y.-S.; Church, J. S.; Woodhead, A. L. Infrared and Raman Spectroscopic Studies on Iron Oxide Magnetic Nano-Particles and Their Surface Modifications. *J. Magn. Magn. Mater.* **2012**, *324* (8), 1543–1550. https://doi.org/10.1016/j.jmmm.2011.11.065.

[63] Maiti, D.; Sujatha Devi, P. Selective Formation of Iron Oxide and Oxyhydroxide Nanoparticles at Room Temperature: Critical Role of Concentration of Ferric Nitrate. *Mater. Chem. Phys.* **2015**, *154*, 144–151. https://doi.org/10.1016/j.matchemphys.2015.01.057.

[64] Grundl, T.; Delwiche, J. Kinetics of Ferric Oxyhydroxide Precipitation. *J. Contam. Hydrol.* **1993**, *14* (1), 71–87. https://doi.org/10.1016/0169-7722(93)90042-Q.

[65] Holder, C. F.; Schaak, R. E. Tutorial on Powder X-Ray Diffraction for Characterizing Nanoscale Materials. *ACS Nano* **2019**, *13* (7), 7359–7365. https://doi.org/10.1021/acsnano.9b05157.

[66] Hoag, G. E.; Collins, J. B.; Holcomb, J. L.; Hoag, J. R.; Nadagouda, M. N.; Varma, R. S. Degradation of Bromothymol Blue by 'Greener' Nano-Scale Zero-Valent Iron Synthesized Using Tea Polyphenols. *J. Mater. Chem.* **2009**, *19* (45), 8671–8677. https://doi.org/10.1039/B909148C.

[67] Shahwan, T.; Abu Sirriah, S.; Nairat, M.; Boyacı, E.; Eroğlu, A. E.; Scott, T. B.; Hallam, K. R. Green Synthesis of Iron Nanoparticles and Their Application as a Fenton-like

Catalyst for the Degradation of Aqueous Cationic and Anionic Dyes. *Chem. Eng. J.* **2011**, *172* (1), 258–266. https://doi.org/10.1016/j.cej.2011.05.103.

# Chapter 3. Glycerol oxidation with magnetite-based catalysts: Exploring Fenton-like and photocatalytic reactions


## Abstract

With current needs for alternatives from traditional fossil fuels, the biodiesel production has been rapidly increasing. This however led to a need in valorizing the glycerol byproduct. The catalytic oxidation of glycerol to dihydroxyacetone is a promising avenue but is challenging due to selectivity. Herein we present the use of $Fe_3O_4$ nanoparticles as catalysts in a Fenton-like and a photo Fenton-like systems for this reaction. $Fe_3O_4$ catalysts were obtained by coprecipitation and by a novel steel revalorisation process. The catalysts were characterised by transmission electron microscopy (TEM), X-ray diffraction (XRD), dynamic light scattering (DLS) and UV-Vis spectroscopy. $Fe_3O_4$ catalysts were also doped with Ag nanoparticles to decrease their bandgap as confirmed by the Tauc method. A traditional Fenton oxidation, using $FeCl_3$ as catalyst, was used as benchmark to evaluate the Fenton-like oxidation. Parameters such as the hydrogen peroxide to glycerol ratio, the doping of the catalyst, the type of $Fe_3O_4$ and the mass of catalyst were investigated. The $Fe_3O_4$ catalysts all significantly increased the selectivity towards DHA compared to $FeCl_3$. The highest selectivity obtained was 94% with $Fe_3O_4$ doped with Ag using $NaBH_4$ as reducing agent. However, the conversions remained between 6% and 19% using the $Fe_3O_4$ catalysts. The Ag doped catalyst was also tested in a photo oxidation reaction in the absence of hydrogen peroxide. HPLC measurements indicated the formation of a product, but it's structure could not be elucidated. The light intensity proved to be critical in this reaction, with an optimum of 5000 lux in the system.



## Keywords

Glycerol, $Fe_3O_4$, Fenton, Oxidation, Valorization

## 3.1. Introduction

With today's environmental crisis, the need to decrease the anthropological footprint is more pressing than ever. In this context, development and implementation of alternative fuels to power our commodities has significantly raised over the last three decade, mostly because of governmental policies and incentives [1]. Biodiesel is one of the alternative fuels whose production has increased by nearly 6000% from 2004 to 2023 in USA [2]. Biodiesel is produced from a transesterification reaction of waste vegetable oils to yield crude esters which are the biodiesel and crude glycerol [3]. Indeed, about 10 wt% of the transesterification reaction products is glycerol [4]. Glycerol, or propane-1,2,3-triol, is a viscous liquid at room temperature which is odourless and colourless [5]. It has various applications in pharmaceuticals, cosmetics, food and tobacco industries, but the surplus generated from the increased biodiesel production has negatively affected both the glycerol market and become a challenge for the biodiesel producers [6]. As a result, glycerol is currently generally considered a waste byproduct and may be incinerated, used as animal food supply or simply disposed of in landfills [7,8]. There is therefore a need to implement technologies to valorise this waste stream especially considering that the production of biodiesel is expected to keep growing.

The three hydroxyl groups present in the glycerol chemical structure allow this molecule to undergo a wide range of chemical reactions such as etherification, esterification, carboxylation, hydrogenolysis or oxidation (figure 3.1). A full oxidation can be carried out to yield carbon dioxide which has a lower value than the initial glycerol molecule [9]. A more challenging partial oxidation can be desired to yield valuable chemicals like dihydroxyacetone (DHA), glyceraldehyde (GLAD) or glycolic acid (GLOA). Dihydroxyacetone is produced from the oxidation of the secondary hydroxyl. It is the oxidation product with the highest value since it is used in the cosmetic industry as a tanning agent, as well as in the pharmaceutical, fine chemicals and food industries [10]. Selective oxidation on the secondary carbon is hard to achieve and the oxidation of the primary carbon leads to the formation of glyceraldehyde. This chemical is also used in the cosmetic industry, for organic chemistry and pharmaceutical applications [11]. These oxidations may be performed by different methods for example by using mild reducing agents such as 2,2,6,6-Tetramethylpiperidinyloxy TEMPO [12,13] or hydrogen peroxide [14], by electrochemical processes [15,16], although this method is usually applied to perform a full oxidation to formic acid or $CO_2$ and in parallel produce $H_2$ as an alternative to the water splitting reaction [17].

Catalysts and photocatalysts may also be used to achieve this oxidation, and these approaches are preferred to the use of external oxidants to follow the green chemistry principles of reagent economy, safer chemical synthesis and the use of catalysis [18].

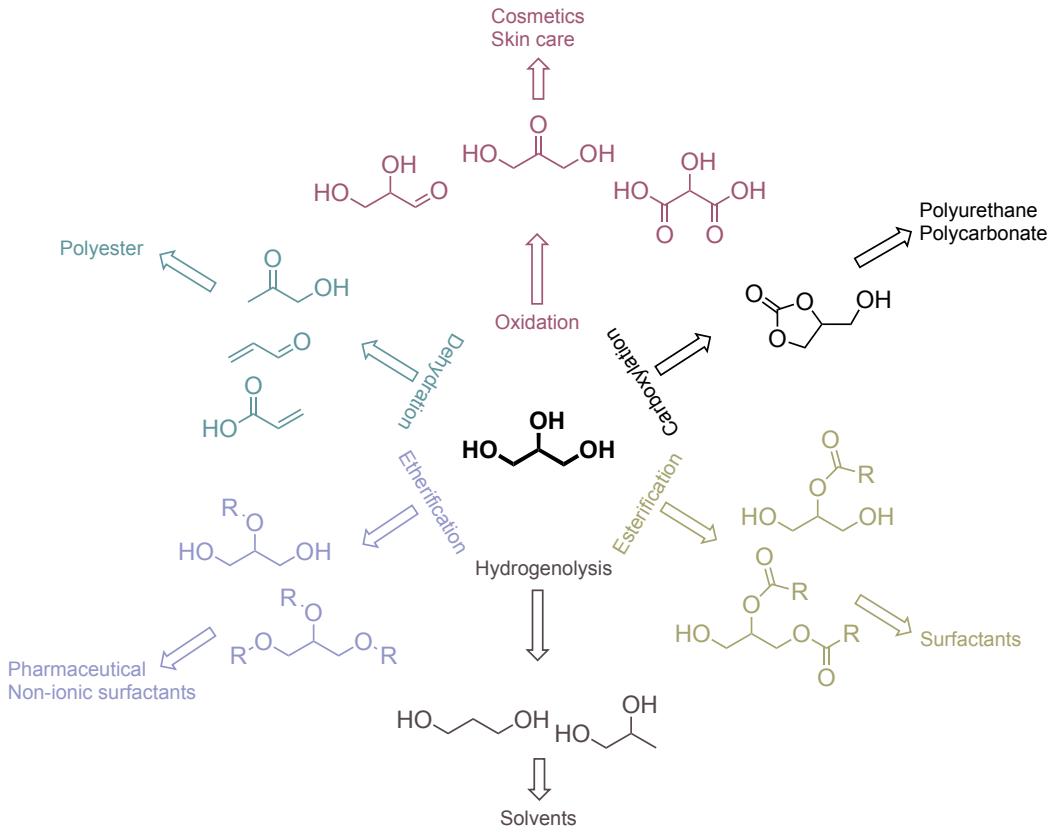


**Figure 3.1.** Examples of possible chemical reactions to valorise glycerol

The vast majority of reported catalytical oxidation of glycerol rely on noble metal-based catalysts for non-photocatalytic system. Platinum, palladium and gold are the three metals which have received the most attention [19]. Pt catalysts showed reactivity in both neutral and acidic environments whereas Au catalysts require basic environments to catalyse the reaction [20]. Pt catalysts preferentially oxidise the terminal hydroxyls on the molecule forming GLAD [21], whereas Pd may be used to selectively produce DHA [22]. However, both these metals tend to deactivate from overoxidation [23,24] Au catalysts are less sensitive to oxygen poisoning, allowing to use higher oxygen partial pressures with these catalysts [25]. When Au was alloyed with Pd or Pt, Villa et al. reported that C-C cleavage was limited thus favoring valuable $C_3$ compounds [26]. Although noble metals have been studied more extensively, their use limits the economic viability

of the technology. There is therefore a need for more accessible catalysts for the valorisation of glycerol by oxidation.

On the other hand, the most widely studied photocatalyst for environmental processes such as this oxidation reaction is by far $TiO_2$ due to its high activity, stability, affordability and non-toxicity [8,27]. The photocatalyzed reaction proceeds by the excitation of electrons from the valence band to the conduction band of the photocatalyst. These excited electrons and the corresponding holes can then react with surrounding chemical species such as water and air or directly oxidise glycerol. When reacting with water or air they generate reactive oxygen species (ROS) which can oxidise glycerol subsequently [28]. The selectivity towards specific products is hard to achieve under these conditions as sequential oxidations may occur [29], but controlled oxidation is still possible and desired to produce valuable chemicals. Indeed, by developing careful reaction condition Liu et al. reported the selective oxidation of glycerol to formic acid in the presence of oxygen via a mechanism involving superoxide radicals [30]. The phase of the $TiO_2$ (anatase to rutile ratio) as well as the type of photoreactor used also proved to have an impact on the selectivity of the yielded products, with commercial P25 (Anatase:Rutile, 85:15) showing a good selectivity towards DHA [31]. Although being popular, a major drawback of $TiO_2$ resides in its large band gap ($\sim$ 3.0-3.2eV) which requires UV light to be activated [32]. As this source of light is limited with only 5% of the sun energy being in the UV range, research has been carried out to decrease the band gap and allow for activation by visible light [33]. Recently, Rojas et al. decorated P25 ($TiO_2$) with Ag nanoparticles and produced dihydroxyacetone with high selectivity by using visible light [34].

Another approach is to use semiconducting materials with smaller band gaps as photocatalysts. $Fe_3O_4$, or magnetite, is an increasingly popular catalyst due to its low cost, high stability, non-noble metal composition, non-toxicity and strong magnetic properties which facilitates its recovery. It is also showing potential as a good photocatalyst due to its low band gap of 2 eV [35] which allows for its excitation from visible light [36]. Moreover, iron has been used since the 1990s for waste treatment through Fenton reactions [37] and multiple heterogenous Fenton-like systems using $Fe_3O_4$ as the source of iron have been reported for oxidising organic compounds [38]. The Fenton reaction consists in a strong oxidation of organic compounds mediated by hydroxyl radicals which are generated from hydrogen peroxide [39]. Hydroxyl radicals can also be generated from holes formed during the excitation of electrons in a

photocatalyst such as $Fe_3O_4$,[40], which could allow to perform similar oxidation reactions without the use of hydrogen peroxide.

Magnetite-based catalysts can be upgraded with noble metal nanoparticles to enhance their photocatalytic activity. Indeed, some noble metal nanoparticles exhibit surface plasmonic resonance (SPR) [41]. This phenomenon is observed when frequencies of the incident photons match that of the electrons of the noble metal nanoparticles. The electrons and the photons can then oscillate in resonance thus concentrating the energy of the photons in specific volumes. From this effect, more excited electrons are generated which increases the photocatalytic reactions [42]. Nanoparticles may be deposited on the magnetite support from chemical reduction using traditional reducing agents like $NaBH_4$ [43,44] or from a greener approach through the reduction from plant extracts which contain phytochemicals able to generate and stabilise the nanoparticles [45]. Ag nanoparticles are generally preferred for this application due to their good stability, high sensibility and light absorption in the visible range [46]. Indeed, introducing Ag nanoparticles on the surface can provide additional energy levels for excited electrons to transit into. From the localised surface plasmon resonance effect, Ag nanoparticles can also be excited by a wavelength of light found in the visible light range (around 400nm) which can excite more electrons in the conduction band of magnetite [47].

In this work, various magnetite-based catalysts are proposed and studied for the oxidation of glycerol aiming for a sustainable and green active catalyst. The coprecipitation method is compared with magnetite produced from a revalorisation process of waste steel shavings, and both benchmarked using $FeCl_3$. Coprecipitation is a very widely used approach which consists in combining $Fe^{2+}$ and $Fe^{3+}$ salt solutions in the presence of a strong base which induces simultaneous precipitation to form $Fe_3O_4$ particles [48].On the contrary, in the revalorisation approach waste steel shavings are oxidised using different conditions of pH (3 to 5) and temperature (50-90°C) to form $Fe_3O_4$ nanoparticles [49]. Magnetite nanoparticles show high magnetic susceptibility which allows their easy recovery during their synthesis and after their use as catalysts. Both types of magnetite are upgraded with Ag nanoparticles using a chemical and a natural reducing agent. The synthesized catalysts were used for the catalytic valorisation of glycerol in a heterogeneous Fenton-like system and in a photocatalytic system.

## 3.2. Experimental

### 3.2.1. Materials

Iron sulfate hepta hydrate ($Fe(SO_4)\bullet 7\ H_2O$, 99.5%) and iron chloride hexa hydrate ($FeCl_3\bullet 6\ H_2O$, 99+%) were purchased from Acros Chemicals, silver nitrate ($AgNO_3$, ≥99.7%), hydrogen peroxide 30% v/v ($H_2O_2$), acetonitrile (MeCN, HPLC grade) and concentrated nitric acid ($HNO_3$, 68-70%) were purchased from Fisher scientific, deuterium oxide ($D_2O$, 99.9% atom D) and sodium hydroxide (NaOH, ≥98%) were purchased from Millipore sigma. 1018 steel shavings were obtained from the machine shop of the University of Ottawa. Green tea was purchased from a local supermarket. All reagents were used as received without further purification.

### 3.2.2. Catalyst preparation

#### 3.2.2.1. Coprecipitation

Iron sulfate hepta hydrate ($Fe(SO_4)\bullet 7\ H_2O$) and iron chloride hexa hydrate ($FeCl_3\bullet 6\ H_2O$) were dissolved in deionized water to achieve a $Fe^{2+}$ and $Fe^{3+}$ ratio of 1:2. The obtained solution was heated to 70°C, then the pH was adjusted to 8 using a 5 M NaOH solution. A pH of 8 was selected based on prior optimization conducted in the laboratory. The mixture immediately turned black showing the formation of magnetite. The suspension was stirred for 1 hour with a mechanical stirrer. Magnetite was recovered from the liquid using a magnet and washed with deionized water. It was left to dry overnight in an oven at 40°C.

#### 3.2.2.2. Steel revalorisation

For the novel steel revalorisation process, various temperatures and pH were investigated by our collaborators in Tecnológico de Monterrey to determine optimal conditions to oxidise the steel shavings used and produce a useful material in the form of magnetite [49]. Two different conditions generated reasonable amounts of magnetite with reported yields of 11.25% and 12.56%. These were respectively a combination of a pH = 3 with T = 60°C and a pH = 5 with T = 90°C. Both materials showed magnetic susceptibilities values similar to that of the coprecipitation magnetite with respective values of $\chi_m = 468 \times 10^{-6}\ m^3/kg$ and $\chi_m = 387 \times 10^{-6}\ m^3/kg$. The second method was used for this work due to its shorter reaction time and higher yield.

The obtained steel shavings were washed with an alkaline laboratory soap the remove the oil residues left from the machining process. Once clean, the shavings were rinsed with water to remove leftover soap. They were then placed in a round bottom flask and tap water was added to the flask. The pH was adjusted to 5 using a 10 M solution of $HNO_3$. An overhead mechanical stirrer was introduced in the flask and the neck was sealed with aluminium foil. The mixture was stirred vigorously with the mechanical stirrer while being heated to 90°C for at least 24 hours. Water was added to the flask if needed as some evaporated and the pH was adjusted accordingly. The black powder (magnetite) formed from the reaction was recovered and separated from unreacted steel by using a magnet. It was washed with deionized water and left to dry overnight in an oven at 40°C.

#### 3.2.2.3. Magnetite doping

100 mg of magnetite was suspended in 20 mL of water in a centrifuge tube. The mixture was sonicated using an ultrasound probe for 15 minutes with an amplitude of 40% using 40 seconds on, 20 seconds off cycles. A silver nitrate solution (the concentration depended on the aimed weight percentage deposition) was added to the centrifuge tube. The mixture was mixed using a vortex mixer for 10 minutes to ensure optimal dispersion. A solution of $NaBH_4$ was added to the centrifuge tube. The concentration was determined so 12 hydrides equivalents would be added as this was the optimum measured from UV-Vis experiments described in the results section. It was assumed that each mole of $NaBH_4$ produced 4 hydrides equivalents which could donate one electron for the reduction of $Ag^+$. The resulting mixture was vortex mixed for 20 minutes. The resulting doped catalyst was recovered from the liquid using a magnet and washed with deionized water. It was left to dry overnight in an oven at 40°C. The same methodology was used when green tea was used as the reducing agent. In the case of green tea, 28 hydride equivalents were used.

### 3.2.3. Glycerol oxidation

#### 3.2.3.1. Fenton-like oxidation

The Fenton-like oxidation was performed in the presence of hydrogen peroxide. In a 5 mL centrifuge tube, glycerol was dissolved in deionized water to achieve a 0.1M concentration. When using a magnetite-based catalyst, the catalyst was first suspended in a 1 mL of water and sonicated

for 5 minutes with an amplitude of 40% using 50 seconds on, 10 seconds off cycles. The suspension was then added to the glycerol solution. When $FeCl_3$ was used, it was simply dissolved in the glycerol solution. The desired volume of hydrogen peroxide was then added to the suspension. It was stirred for the desired time using a tube rotator. Aliquots were taken and filtered through 0.2 μm filters, then prepared for nuclear magnetic resonance (NMR) analysis. Conversion and selectivity were determined using NMR with acetonitrile as an internal standard.

#### 3.2.3.2. Photo Fenton-like oxidation

The photo Fenton-like oxidation was performed without hydrogen peroxide. A glycerol solution of 0.1M was placed in a beaker. The magnetite-based catalyst was suspended in 1 mL of water and sonicated for 5 minutes with an amplitude of 40% using 50 seconds on, 10 seconds off cycles. The suspension was added to the glycerol solution and the mixture was stirred using a centrifugal pump. The transparent reaction vessel was placed in a light box to carry out the reaction. Aliquots were taken and filtered through 0.2 μm filters, then analysed using HPLC.

### 3.2.4. Material characterization

#### 3.2.4.1. Catalyst characterization

X-ray diffraction XRD was used to confirm the formation of magnetite by both coprecipitation and revalorisation processes. It was also used to confirm the deposition of silver nanoparticles on the catalyst. It was performed using a Bruker D8 Endeavor Polycrystalline X-rays diffractometer with a Cu Kα sealed-tube source (λ=1.54184 Å) and a LynxEye XE-T 1-D silicon strip detector. UV-Vis spectroscopy was used to determine the optimal ratio of reducing agent necessary to full reduce the silver nitrate precursor into nanoparticles. An Agilent Cary 60 was used in the absorbance mode to perform this analysis. Dynamic light scattering (DLS) was used to measure the particle size distribution of the magnetite catalysts. Water was used as the solvents and the magnetite suspension had a concentration of 7g/L It was performed using a Malvern zetasizer nano ZS. Transmission electron microscopy (TEM) was performed with a JEOL 2010 TEM to measure the particle size of different catalysts and evaluate their morphology.

3.2.4.2. Band gap determination

An Agilent Cary 100 was used in the diffuse reflectance spectroscopy (DRS) mode to perform the measurement necessary to determine the band gaps of the synthesized catalysts. The bandgaps were calculated using the Tauc method for a direct transition. The reflectance values obtained from the instrument are presented in Kubelka-Munk units (F(R)) vs wavelength (nm). By plotting the reflectance as a function of the photon energy ($hv$,eV) according to Tauc's equation, the bandgap energy can be determined from the extrapolated x-intercept of the linear portion of the plot [50].

$$[F(R)hv]^2 = B\left(hv - E_g\right) \quad (1)$$

Where F(R) is the reflectance in Kubelka-Munk units, $h$ is the Plack's constant, $v$ is the photon's frequency, B is a constant and $E_g$ is the bandgap

3.2.4.3. NMR analysis

NMR measurements were performed with a Bruker Avance III HD 500MHz. The samples (pure species used as standards or reaction aliquots) were dissolved in 90% $H_2O$ and 10% $D_2O$ mixture. $^1$H NMR spectra were recorded using two water suppression techniques: an excitation sculpting technique and a presaturation technique. Acetonitrile was used as an internal standard to perform quantitative analysis. Each component's concentration in the solution was evaluated using the following equation:

$$C_{analyte} = \frac{I_{analyte}}{I_{IS}} \frac{N_{IS}}{N_{analyte}} C_{IS} \quad (2)$$

Where $C$ is the concentration, $I$ is the integral area of the peak of interest and $N$ is the number of nuclei. $IS$ represents the internal standard (here acetonitrile).

A $^1$H NMR spectra of each experiment was recorded prior to adding the hydrogen peroxide (i.e. at time zero). All glycerol conversions were calculated based on their respective initial spectra. The conversion was calculated using the following equation:

$$Conversion\ (\%) = \frac{I_{glycerol,0} - I_{glycerol,t}}{I_{glycerol,0}} \times 100 \quad (3)$$

The selectivity of the reaction towards a specific compound was calculated only from the spectra obtained by the presaturation technique. This was because the excitation sculpting method led to a partial suppression of the dihydroxyacetone peak (the main product) resulting in an artificially lower integral area.

$$Selectivity\ (\%) = \frac{n_{product\ of\ interest}}{\sum n_{product}} \quad (4)$$

3.2.4.4. HPLC analysis

HPLC measurements were performed using a Shimadzu Prominence equipped with a UV detector A Nucleogel sugar 810H, 8-10µm 300x7.8mm column as used. The mobile phase was composed of 85% water and 15% acetonitrile with a flowrate of 0.5 mL/min. The column temperature was of 70°C and the injection volume was 20µL.

## 3.3. Results and discussion

### 3.3.1. Magnetite characterisation

Two different types of magnetite were compared for this application: a well-established synthesis method by coprecipitation and a novel synthesis from revalorisation of industrial steel shavings (cold rolled 1018 steel), as described in the catalyst preparation section. XRD was performed on both coprecipitation and revalorisation magnetite to confirm the oxidation state of the iron and compare both syntheses. As seen on figure 3.2, the coprecipitation method resulted in pure magnetite with no impurities present as expected from this well-established procedure. XRD spectra of the material yielded from the revalorisation condition also corresponded to magnetite with both powders showing a great fit with PDF card no: 01-075-0449. Surprisingly, when using the revalorisation approach no impurities were identified. Some other elements were expected as 1018 steel is an alloy containing mostly iron, but also some carbon, manganese, phosphorous and sulfur[51,52]. It appears that these other elements did not react in the revalorisation process or

were completely removed during the washing process as none were observed by XRD. The only complementary signal which did not correspond with the $Fe_3O_4$ diffraction pattern was identified as Fe and its peaks are labeled by blue circles on Figure 3.2b. This iron could come from partially unreacted steel which led to non-oxidised iron.

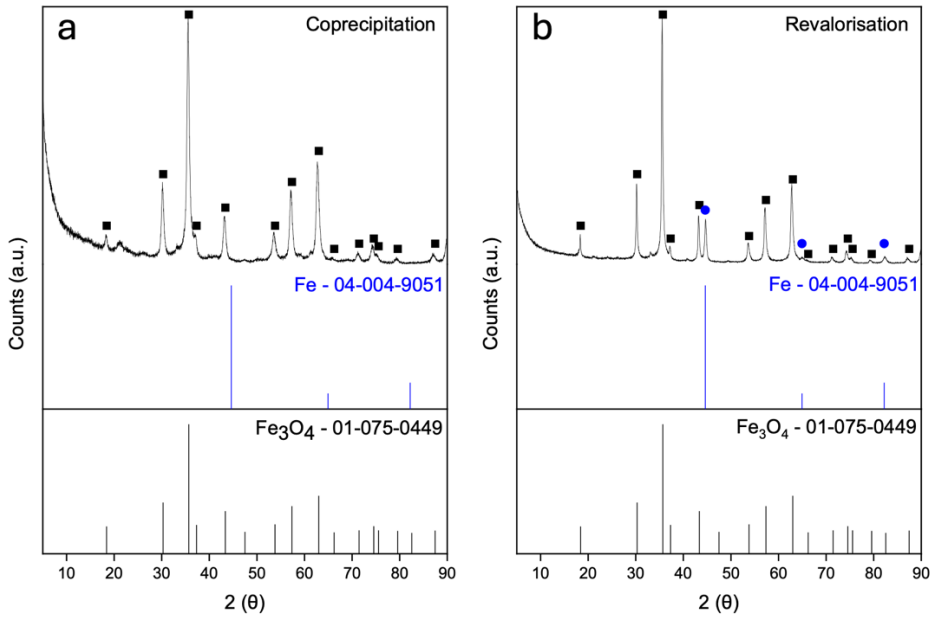


**Figure 3.2.** XRD diffraction patterns of $Fe_3O_4$ obtained by (a) coprecipitation and (b) steel revalorisation

DLS measurements were performed on the two different types of magnetite to compare the average size of the particles and determine if a single or multiple size distributions were obtained. From figure 3.3a, it can be seen that both methods resulted in uniform sizes with only one size distribution being observed in both cases. Both methods yielded particles of similar sizes with the average diameter for the coprecipitation sample being 205 nm and the average diameter for the revalorised sample being 210 nm. Surprisingly, the revalorised magnetite also showed a slightly narrower size distribution. This similarity in size between both methods was also observed by TEM imaging (figure 3.3b, 3.3c).

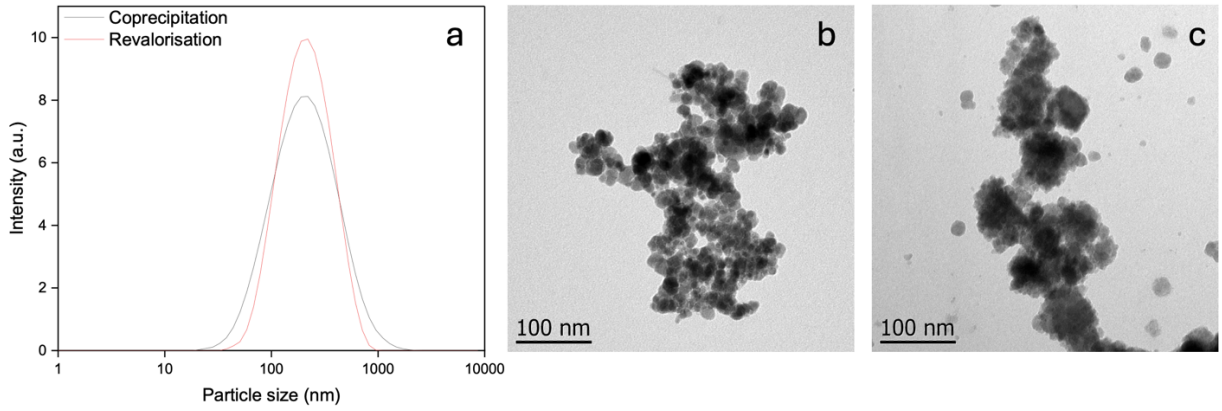


**Figure 3.3.** Size distribution of the magnetite nanoparticles measured by (a) DLS. TEM images of (b) coprecipitated magnetite and (c) revalorised magnetite

On the other hand, smaller particles are observed from the TEM images (figure 3.3b, 3.3c). Indeed, the coprecipitation method yielded circular particles of about 25nm. The particles do however form agglomerates and this type of behaviour is expected from magnetic materials [53]. Individual particles can however be identified from the TEM images. The nanoparticles yielded from the revalorisation protocol are also circular with an average diameter of about 50nm and agglomerates of similar size are observed. When starting with large steel residues, a complete degradation to atoms is improbable contrary to the case with the coprecipitation method. Hence, larger clusters are generated though the revalorisation process rather than the perfect nucleation observed in the coprecipitation method. The difference in size between the DLS and TEM measurements can be explained by the agglomeration observed on the TEM images. Indeed, when performing DLS it is perhaps the size of the agglomerates which is measured. This could also explain the broader size distribution observed by DLS for the coprecipitation magnetite as less particles are agglomerated causing the distribution to be less uniform.

### 3.3.2. Magnetite doping with silver nanoparticles

Both types of magnetite were doped with Ag nanoparticles to increase their photocatalytic activity. An initial assessment was performed to determine optimal ratios of reducing agent required to generate the Ag nanoparticles. Two different reducing agents were compared: a traditional chemical being $NaBH_4$ and a greener alternative being green tea extract. The formation of nanoparticles was monitored by UV-Vis as Ag nanoparticles absorb light in the range of 400 to

500 nm [54], and was also confirmed by the light-yellow appearance of the yielded nanoparticle suspension.

The first step was to determine the right reducing agent to $AgNO_3$ ratio. Figure 3.4a depicts the variation in the intensity of the absorption peak corresponding the Ag nanoparticles as the $NaBH_4$ to $AgNO_3$ ratio is modified. A ratio of 12 equivalents proved to be the ideal as past this value the too large excess of reducing agent led to agglomeration of the nanoparticles and a decrease in the light absorption This was also confirmed by a visual change in the suspension with the appearance of grey particles suspended in the liquid. As the amount of reducing agent was increased further, large clusters were formed and settled out of the solution with the solution's colour transitioning from the yellow (indicative of Ag nanoparticles) back to being transparent.

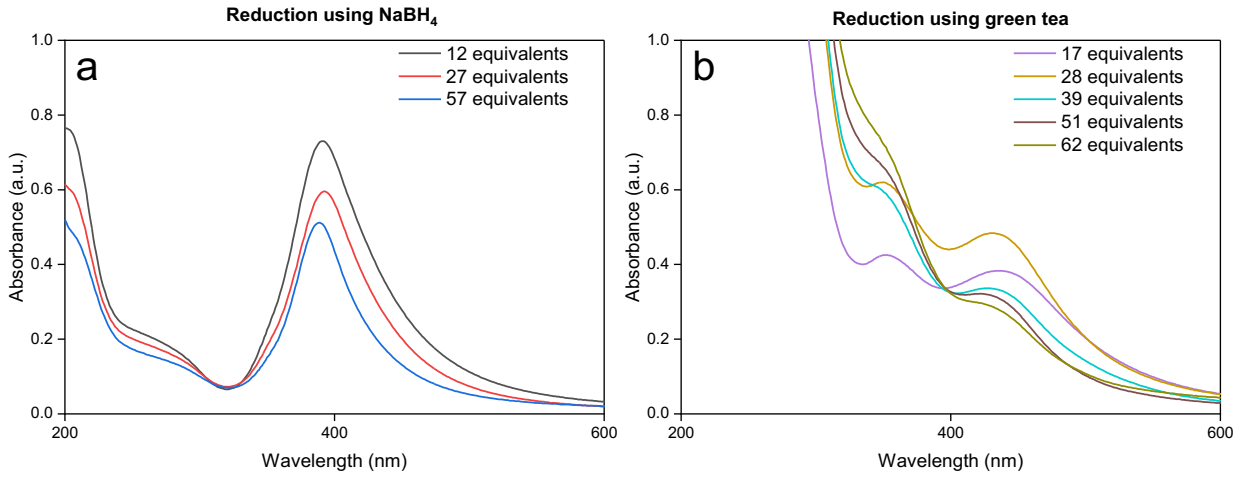


**Figure 3.4.** Silver nanoparticles absorbance when different equivalents of (a) $NaBH_4$ and (b) green tea are used as reducing agent

Upon addition of $NaBH_4$, the colour change was observed immediately. In the case of the addition of green tea (figure 3.4b), the colour change was not as evident because of the light brown colour of the extract itself. However, a colour change was still observed. UV-Vis measurements were also used to determine the optimal ratio of green tea extract to $AgNO_3$ precursor. Contrary to the case when using $NaBH_4$, the appearance of the absorption peak at 430nm was not immediately observed upon addition of green tea. In fact, about 30 minutes were necessary to allow for the full development of the peak which indicates that the reduction process takes place at a slower rate

under these conditions. This is not surprising as the green tea extract reduction relies on polyphenols present in the solution to achieve the reduction. Polyphenols are not as strong reducing agents as $NaBH_4$ which could explain slower reaction kinetics as per the Marcus electron transfer theory [55,56]. An increase in the intensity of the peak associated to Ag nanoparticles was still observed and an optimal ratio of 28 equivalents was established for the green tea reduction. A very high absorbance was also measured at lower wavelengths from the absorption of light by the aromatic phytochemicals present in the tea extract.

Both coprecipitation and revalorised magnetite were doped with Ag nanoparticles using the two different reducing agents with their respective optimal ratios established above. The resulting catalysts were characterised by XRD (figure 3.5) to confirm the successful doping with Ag. In both cases when $NaBH_4$ was used, the diffraction peaks associated to Ag (identified by red triangles) were sharper and taller than when using green tea. The coprecipitation magnetite doped using $NaBH_4$ was the best example. However, Ag peaks were observed nonetheless when using the green reduction method (figure 3.5b). The diffraction pattern of silver matched that of $Ag^0$ (PDF card no. 04-002-1171) showing that the silver precursor was effectively reduced by both $NaBH_4$ and green tea. Magnetite also proved to be a suitable support to prevent the oxidation of the generated nanoparticles as no form of silver oxides were observed.

UV-Vis measurements of the photocatalysts (see supplementary information) were performed using diffuse reflectance spectroscopy (DRS) to establish the direct band gap of each material using the Tauc method. As desired, all the photocatalysts absorbed light in the visible range from the DRS measurements. This is further confirmed by the band gap values established in figure 3.5c and 3.5d. The coprecipitation and revalorisation magnetite had very similar values with respective $E_g$ values of 2.02 and 2.08 eV. Doping the supports with Ag nanoparticles decreased these values as desired. A smaller band gap value was desired to allow the photocatalyst to be activated by a broader range of visible light. For both supports, doping using green tea resulted in smaller band gap values of 1.88eV and 1.95eV for the coprecipitation and the revalorisation supports respectively, compared to 2.00eV and 1.99eV when using $NaBH_4$. This reduction in the band gap when using green tea can be explained by the presence of leftover aromatic compounds in the photocatalyst which act as p- or n- dopants depending on the molecule [57] or by less crystalline Ag nanoparticles being produced from this method than from the $NaBH_4$ reduction [58].

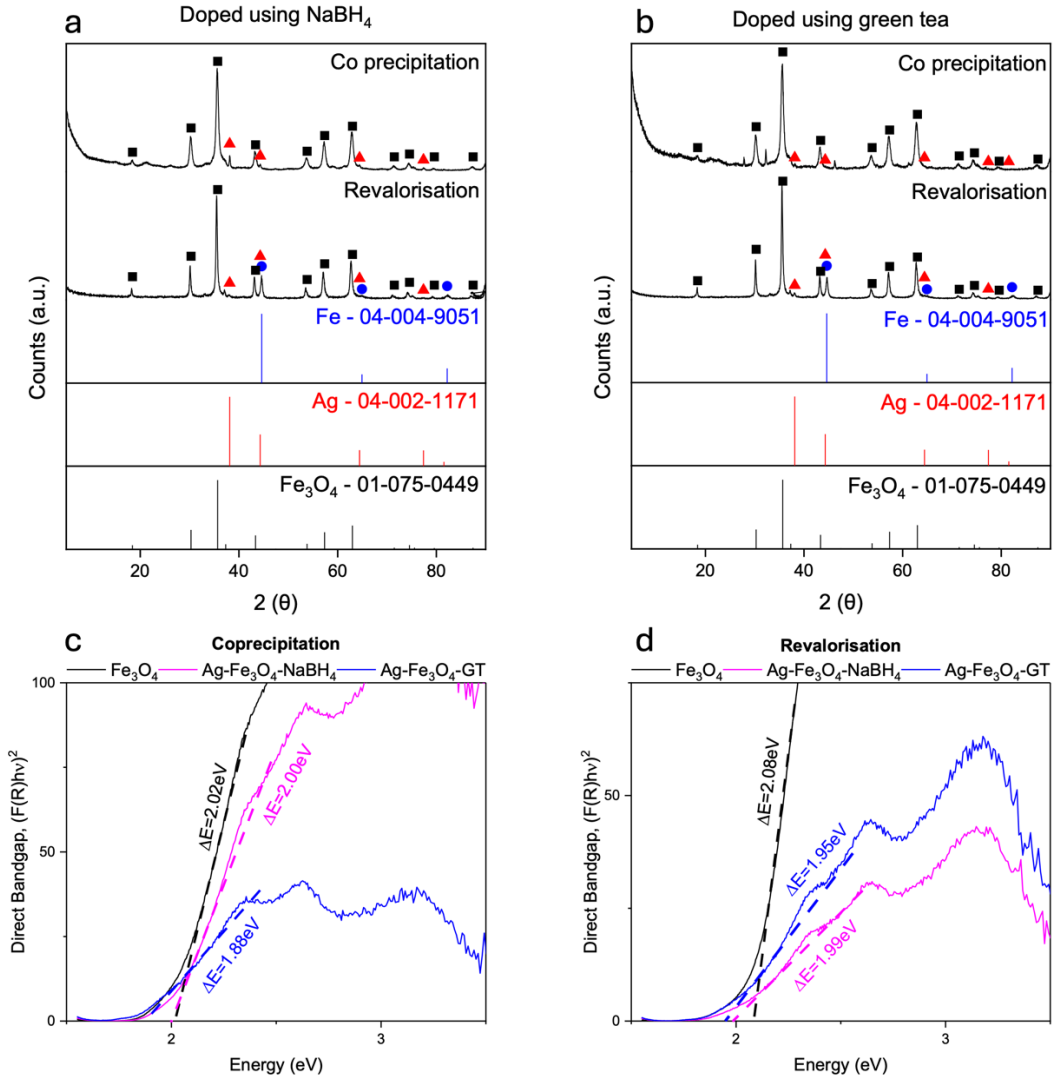


**Figure 3.5.** XRD diffraction patterns of silver doped magnetite using (a) NaBH4 and (b) green tea as reducing. Band gaps of the catalysts determined from the Tauc method using (c) coprecipitation magnetite and (d) revalorisation magnetite

### 3.3.3. Glycerol oxidation in the presence of $H_2O_2$

The synthesized catalysts were then used to perform the catalytic oxidation of glycerol in the presence of hydrogen peroxide. Table 3.1 summarizes the different reaction conditions with their respective conversion and selectivity towards formic acid (FA) and dihydroxyacetone (DHA).

**Table 3.1.** Reaction conditions when the glycerol oxidation is carried out in the presence of $H_2O_2$ in Fenton and Fenton-like systems

| Entry | Catalyst | Catalyst mass (mg) | $H_2O_2$/Glycerol | Conversion (%) | Selectivity (%) | |
|---|---|---|---|---|---|---|
| | | | | | FA | DHA |
| 1 | $FeCl_3$ | 8.1 | 4.2 | 66 | 59 | 23 |
| 2 | | | 2.8 | 66 | 68 | 25 |
| 3 | | | 1.4 | 29 | 53 | 39 |
| 4 | | | 1 | 33 | 57 | 37 |
| 5 | $Fe_3O_4$ | 6.9 | 2.8 | 10 | 32 | 68 |
| 6 | | | 1.4 | 6 | 40 | 57 |
| 7 | | | 1 | 9 | 35 | 51 |
| 8 | 1%Ag-$Fe_3O_4$-$NaBH_4$ | 6.9 | 2.8 | 7 | 7 | 93 |
| 9 | 1%Ag-$Fe_3O_4$-GT | | 2.8 | 13 | 13 | 88 |
| 10 | $Fe_3O_4$ | 69 | 2.8 | 10 | 75 | 25 |
| 11 | | 0.69 | 2.8 | 11 | 12 | 88 |
| 12 | Revalorisation $Fe_3O_4$ | 6.9 | 2.8 | 19 | 25 | 73 |

The developed catalysts were used and compared to a traditional Fenton system based on experimental conditions reported by Farnetti & Crotti [59]. The oxidation reactions were performed at room temperature in water and under a standard atmosphere to favor the oxidation process. The hydrogen peroxide to glycerol ratio was initially decreased to limit the oxidation potential and prevent over oxidation of glycerol. Indeed, the most valuable product generated from this oxidation process is DHA which is produced from one single oxidation on the secondary hydroxyl. The selectivity towards this desired product and the glycerol conversion were measured by NMR amongst the observed products. It is to be noted that some glycerol was converted to products which did not appear on NMR spectra. DHA selectivity was compared to that of FA which was the main compound observed by Farnetti & Crotti [59] when using $FeCl_3$ under these conditions. FA is produced from a stronger oxidation of glycerol involving C-C bond cleavages and is generally associated to a mechanism involving glyceraldehyde as the product of the initial oxidation rather than DHA [60]. As such, monitoring the selectivity towards FA also indirectly

allows to assess the selectivity of the first oxidation towards the primary or the secondary hydroxyl. Figure 3.6 compares the glycerol yields, and the DHA selectivity obtained from the various reaction conditions.

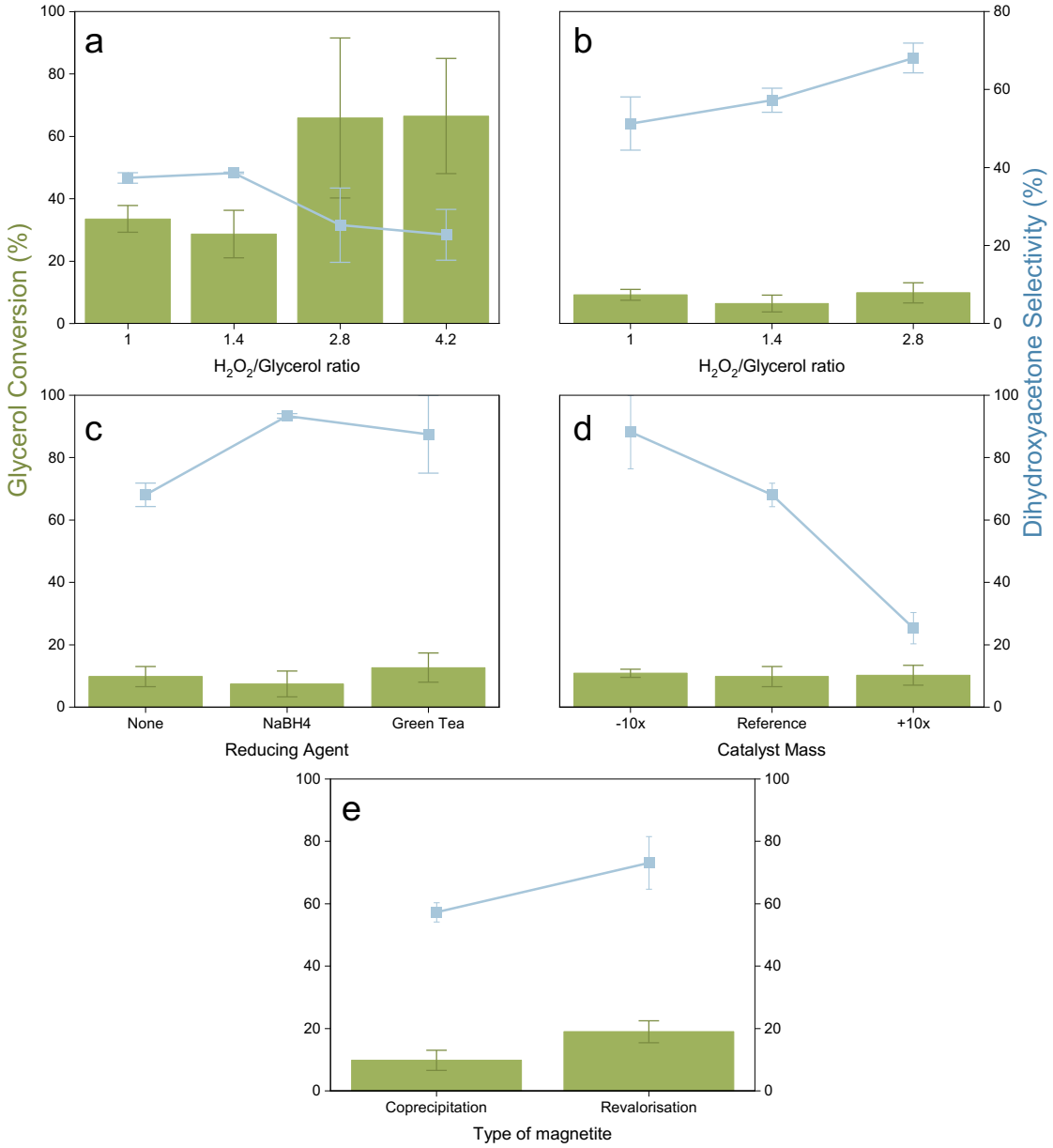


**Figure 3.6.** Glycerol conversion and DHA selectivity in the Fenton and Fenton-like systems after a reaction time of 2 hours at ambient temperature. Effect of the $H_2O_2$ to glycerol ratio in the (a) Fenton system catalyzed with $FeCl_3$ and the (b) Fenton-like system catalysed with coprecipitation $Fe_3O_4$. Using a $H_2O_2$ to glycerol ratio of 2.8 effect of the (c) nature of the reducing agent used for Ag doping coprecipitation $Fe_3O_4$, the (d) mass of catalyst (-10x = 0.69mg, reference = 6.9mg, +10x = 69mg) and the (e) type of magnetite in the Fenton-like system. For all conditions, n=2.

Figure 3.6a, (entries 1 to 4 of table 3.1) were realised using $FeCl_3$ as a catalyst in a traditional Fenton system. In this very strongly oxidising system, a complete oxidation to FA was expected. This is confirmed by the high conversions observed for $H_2O_2$/glycerol ratios of 4.2 and 2.8 which reached 66%. In both these cases, the major product observed was FA and the DHA selectivity was only 23% and 25% respectively. As the $H_2O_2$/glycerol ratio was decreased to 1.4 and 1, the DHA selectivity increased to 39% and 38%, as expected. Decreasing the ratio would decreases the oxidising potential, leading to an increase in the DHA selectivity as less of the reacting glycerol would undergo multiple oxidation reactions. This increase in selectivity did come at the expense of the overall glycerol conversion which decreased to 29% and 34% respectively. This initial investigation using a Fenton system confirmed that weaker oxidising conditions could enhance the selectivity towards DHA, which is the desired compound from this reaction. However, this increase remained limited as all ratios still lead to the formation of FA in majority.

It was expected for the magnetite to have a weaker catalytic activity than the $FeCl_3$ as the former is not soluble in water. This insolubility results in mass transfer limitations and a limitation in available catalytic sites which should lead to lower conversions. As expected, figure 3.6b (entries 5 to 7 from table 3.1) shows the results obtained using the same operating parameters, but with the coprecipitation $Fe_3O_4$ catalyst, and the conversion is significantly lower. Glycerol conversions of 10%, 6% and 9% were observed when ratios of $H_2O_2$/glycerol of 2.8, 1.4 and 1 were used. It is important to note that $Fe_3O_4$ catalyses the degradation of hydrogen peroxide, thus preventing it from fully reacting in the oxidation reaction [61] and decreasing the conversion even further. This was confirmed by pressure buildups in reaction tubes when using $Fe_3O_4$ which increased with increasing ratios. This prevented performing the conditions of a $H_2O_2$/glycerol ratio of 4.2 as the increase in pressure was too high. Although the conversion was lower for all ratios it was not impacted as much from the difference in $H_2O_2$/glycerol ratio in this Fenton-like system. However, DHA selectivity was higher in all cases when $Fe_3O_4$ was used. DHA selectivity values of 69%, 57% and 51% were measured for ratios of 2.8, 1.4 and 1, and increased with increasing $H_2O_2$/glycerol ratio. This showed that the catalyst itself was a major determinant in the outcome of the reaction and that magnetite could positively favor the production of DHA.

1% Ag doped magnetite was used for the glycerol oxidation using a $H_2O_2$/glycerol ratio of 2.8 (figure 3.6c entries 8,9 of table 3.1) to investigate the impact of adding silver to the magnetite.

Two catalyst types were used: one doped using $NaBH_4$ as the reducing agent and the second doped using green tea as the reducing agent. For both catalysts, the silver nanoparticles did not significantly enhance the reactivity of the catalyst to increase the glycerol conversion. Measured conversion were respectively of 7% and 13% compared to the 10% obtained for non-doped magnetite using the same operating conditions. Although both conversions are slightly different, this difference is within the error. However, the presence of silver did favor the selectivity towards DHA as both these catalysts showed the highest selectivity amongst all the tested conditions. DHA selectivity as high as 94% was achieved with the catalyst doped using $NaBH_4$ and the catalyst doped using green tea resulted in a DHA selectivity of 88%.

The catalyst loading was investigated next using a $H_2O_2$/glycerol ratio of 2.8 (entries 10,11 of table 3.1) to see its impact and evaluate if it could increase the overall glycerol conversion of the process. The mass of catalyst used for the process was increased and decreased by a factor of 10 thus 0.69 mg (0.23 g/L) and 69.0 mg (23 g/L) of catalyst were compared to the 6.9 mg (2.3 g/L) used in the other conditions. As seen in figure 3.6d, the overall conversion was not affected by the catalyst loading as the conversion was measured to be 11% when less catalyst was used and 10% when more catalyst was used compared to 10% when the standard concentration of catalyst was used. The selectivity, on the contrary, was significantly affected by the catalyst loading. Indeed, when a larger loading was used the selectivity completely shifted to favor the production of FA. The DHA selectivity for a 10x higher loading decreased to 25% whereas it increased to 88% when using a 10x lower loading. The absence of decrease in conversion is likely because when less catalyst was used, the reaction mixture was closer to being homogeneous which should favor the full reactivity of the catalyst. In the cases when the normal amount and a higher amount of catalyst were used, some particles did not remain in suspension which could limit their reactivity. Therefore, an excess of catalyst was used under normal conditions and most of it did not contribute to the reaction. Having the ability to use less catalyst contributes to minimising the environmental footprint of the process.

The final catalyst tested was the magnetite obtained from the revalorisation process using a $H_2O_2$/glycerol ratio of 2.8 (entry 12 of table 3.1). It was compared to the coprecipitation magnetite and as seen in figure 3.6e the revalorisation magnetite led to both an increase in conversion and selectivity. It indicates that the revalorisation method yields magnetite with slightly different

features which enhance its reactivity, even if these features were not identified by XRD and TEM analysis.

### 3.3.4. Photocatalytic glycerol oxidation in the absence of $H_2O_2$

The photocatalytic activity of the Ag doped magnetite on its own was briefly evaluated under different reaction conditions and monitored by HPLC, to evaluate the possible activity of the catalyst. For this set of experiments, the reaction vessel was kept in a light box to ensure a constant degree of illumination during the reaction. Table 3.2 summarizes the reaction conditions investigated. The most standardized catalyst, coprecipitation magnetite doped using $NaBH_4$, was used for this study to minimise the variability between experiments and optimise reaction conditions. The reactions were carried out for up to 20 hours at room temperature or otherwise stated in the absence of $H_2O_2$.

**Table 3.2.** Reaction conditions in the photocatalytic glycerol oxidation

| Entry | Catalyst | pH | Light intensity (Lux) | Temperature (°C) |
|---|---|---|---|---|
| 1 | 1%Ag-$Fe_3O_4$-$NaBH_4$ | 6 | 500 | 30 |
| 2 | 1%Ag-$Fe_3O_4$-$NaBH_4$ | 6 | 5000 | 30 |
| 3 | 1%Ag-$Fe_3O_4$-$NaBH_4$ | 6 | 15 000 | 30 |
| 4 | 1%Ag-$Fe_3O_4$-$NaBH_4$ | 2 | 5000 | 30 |
| 5 | 1%Ag-$Fe_3O_4$-$NaBH_4$ | 10 | 5000 | 30 |
| 6 | 1%Ag-$Fe_3O_4$-$NaBH_4$ | 6 | 5000 | 80 |

The first parameter investigated was the impact of the light intensity. Entries 1-3 of table 3.2 compared three different degrees of illumination: 500 lux, 5000 lux and 15 000 lux. From the HPLC chromatograms (see supplementary information), it was seen that a minimal light intensity of 5000 lux was required for the photocatalytic process to take place at a sufficient rate. Indeed, when 500 lux were used a peak indicative of a species produced appeared at a retention time of 26.8 minutes after 3 hours of reaction. In the cases of 5000 lux and 15000 lux, the same compound was formed after a reaction time of only 2 hours and the intensity of the peak representing this product were similar and both significantly larger than entry 1. Although these conditions showed

that a 5000-lux illumination was proper for this reaction, further increase in the light intensity did not provide any additional benefit.

The pH of the reaction mixture was then modified to compare an acidic environment with a pH of 2 (entry 4) and a basic environment with a pH of 10 (entry 5). In the acidic environment, no significant improvement was observed compared to the reference case (pH = 6) as the produced compound was observed with the same retention time of 26.8 minutes after 2 hours of reaction. There was however a substantial increase in the intensity of the peak associated with glycerol. The associated retention time of glycerol was also slightly longer than when no pH modification was performed at 7.4 minutes instead of the 6.8 minutes observed in other cases indicating a slight decrease in polarity. When the pH was adjusted to 10, glycerol eluded as a combination of three smaller peaks with the same retention time of 6.8 minutes. This could be from partial deprotonation of the glycerol as the pH of the reaction approached its theoretical pKa value of 14.4 [62]. The compound produced however still eluded with the same retention time of 26.8 minutes. In this case, it was observed after only one hour, which indicated that in a more basic environment the reaction kinetics were improved. The yield however did not increase as the area of the peak remained the same as when no modification of pH was performed. Finally, the last parameter investigated was the reaction temperature. An experiment was conducted with a temperature of 80°C and no modification to the pH (entry 6). Increasing the temperature did not result in any increase in yield or significantly enhanced reaction rate as the product was observed after 2 hours and its area was not larger than that of the reference conditions.

## 3.4. Conclusion

Magnetite nano-catalysts were synthesized by two different methods: coprecipitation and a novel steel revalorisation process. Both methods yielded pure $Fe_3O_4$ with a nearly identical particle size distribution. TEM imaging showed that the revalorisation magnetite was made of larger nanoparticles of about 50 nm instead of the 25 nm particles observed in the co precipitation magnetite. Both supports were successfully doped to introduce silver nanoparticles using $NaBH_4$ and green tea as reducing agents. Ag nanoparticles were introduced to decrease the band gap of the catalyst to enhance their photocatalytic reactivity for the glycerol oxidation reaction under visible light. All Ag doped samples proved to have decreased band gaps from the Tauc

determination. Both catalysts doped using green tea had the smallest band gap likely from the presence of leftover aromatic compounds acting as dopants. Magnetite and Ag doped magnetite showed promising results in the non-photocatalytic Fenton-like oxidation of glycerol. Indeed, using this type of catalyst allowed to tune the selectivity of the reaction to favor the production of dihydroxyacetone which is the oxidation compound with the highest economical value. This could not be achieved with a traditional Fenton system. Ag doped magnetite using $NaBH_4$ showed a selectivity as high as 94% in favor of DHA which is very promising as this partial oxidation is very challenging. However, the glycerol conversion remained low, in the range of 10% for all catalysts. Ongoing work is being conducted to address this limitation by investigating other metal nanoparticles and reaction conditions. An increase in conversion will likely lead to a decrease in selectivity due to formation on byproducts, therefore an optimum will need to be achieved. The Ag doped catalyst was also tested in a photocatalytic oxidation process. This preliminary study showed that the catalyst was active in this process, but a minimum light source of 5000 lux was necessary to activate the catalyst. The reaction kinetics also seemed to be favored by basic pH whereas an increase in temperature did not lead to any improvement in conversion.

# References


[1] *Biofuels explained - data and statistics - U.S. Energy Information Administration (EIA)*. https://www.eia.gov/energyexplained/biofuels/data-and-statistics.php (accessed 2024-12-19).

[2] *Alternative Fuels Data Center: Maps and Data - U.S. Biodiesel Production, Exports, and Consumption*. https://afdc.energy.gov/data/10325 (accessed 2024-12-19).

[3] Marchetti, J. M.; Miguel, V. U.; Errazu, A. F. Possible Methods for Biodiesel Production. *Renew. Sustain. Energy Rev.* **2007**, *11* (6), 1300–1311. https://doi.org/10.1016/j.rser.2005.08.006.

[4] Bagnato, G.; Iulianelli, A.; Sanna, A.; Basile, A. Glycerol Production and Transformation: A Critical Review with Particular Emphasis on Glycerol Reforming Reaction for Producing Hydrogen in Conventional and Membrane Reactors. *Membranes* **2017**, *7* (2), 17. https://doi.org/10.3390/membranes7020017.

[5] Quispe, C. A. G.; Coronado, C. J. R.; Carvalho Jr., J. A. Glycerol: Production, Consumption, Prices, Characterization and New Trends in Combustion. *Renew. Sustain. Energy Rev.* **2013**, *27*, 475–493. https://doi.org/10.1016/j.rser.2013.06.017.

[6] Konwar, L. J.; Mikkola, J.-P.; Bordoloi, N.; Saikia, R.; Chutia, R. S.; Kataki, R. Chapter 3 - Sidestreams From Bioenergy and Biorefinery Complexes as a Resource for Circular Bioeconomy. In *Waste Biorefinery*; Bhaskar, T., Pandey, A., Mohan, S. V., Lee, D.-J., Khanal, S. K., Eds.; Elsevier, 2018; pp 85–125. https://doi.org/10.1016/B978-0-444-63992-9.00003-3.

[7] Attarbachi, T.; Kingsley, M. D.; Spallina, V. New Trends on Crude Glycerol Purification: A Review. *Fuel* **2023**, *340*, 127485. https://doi.org/10.1016/j.fuel.2023.127485.

[8] Hu, X.; Lu, J.; Liu, Y.; Chen, L.; Zhang, X.; Wang, H. Sustainable Catalytic Oxidation of Glycerol: A Review. *Environ. Chem. Lett.* **2023**, *21* (5), 2825–2861. https://doi.org/10.1007/s10311-023-01608-z.

[9] Fan, L.; Liu, B.; Liu, X.; Senthilkumar, N.; Wang, G.; Wen, Z. Recent Progress in Electrocatalytic Glycerol Oxidation. *Energy Technol.* **2021**, *9* (2), 2000804. https://doi.org/10.1002/ente.202000804.

[10] Liu, D.; Liu, J.-C.; Cai, W.; Ma, J.; Yang, H. B.; Xiao, H.; Li, J.; Xiong, Y.; Huang, Y.; Liu, B. Selective Photoelectrochemical Oxidation of Glycerol to High Value-Added Dihydroxyacetone. *Nat. Commun.* **2019**, *10* (1), 1779. https://doi.org/10.1038/s41467-019-09788-5.

[11] El Roz, A.; Fongarland, P.; Dumeignil, F.; Capron, M. Glycerol to Glyceraldehyde Oxidation Reaction Over Pt-Based Catalysts Under Base-Free Conditions. *Front. Chem.* **2019**, *7*. https://doi.org/10.3389/fchem.2019.00156.

[12] Liebminger, S.; Siebenhofer, M.; Guebitz, G. Oxidation of Glycerol by 2,2,6,6-Tetramethylpiperidine-N-Oxyl (TEMPO) in the Presence of Laccase. *Bioresour. Technol.* **2009**, *100* (20), 4541–4545. https://doi.org/10.1016/j.biortech.2009.04.051.

[13] Ciriminna, R.; Pagliaro, M. One-Pot Homogeneous and Heterogeneous Oxidation of Glycerol to Ketomalonic Acid Mediated by TEMPO. *Adv. Synth. Catal.* **2003**, *345* (3), 383–388. https://doi.org/10.1002/adsc.200390043.

[14] Wang, X.; Wu, G.; Wang, F.; Ding, K.; Zhang, F.; Liu, X.; Xue, Y. Base-Free Selective Oxidation of Glycerol with 3% H2O2 Catalyzed by Sulphonato-Salen-Chromium(III)

Intercalated LDH. *Catal. Commun.* **2012**, *28*, 73–76. https://doi.org/10.1016/j.catcom.2012.08.014.

[15] Coutanceau, C.; Baranton, S.; Kouamé, R. S. B. Selective Electrooxidation of Glycerol Into Value-Added Chemicals: A Short Overview. *Front. Chem.* **2019**, *7*. https://doi.org/10.3389/fchem.2019.00100.

[16] Liu, C.; Hirohara, M.; Maekawa, T.; Chang, R.; Hayashi, T.; Chiang, C.-Y. Selective Electro-Oxidation of Glycerol to Dihydroxyacetone by a Non-Precious Electrocatalyst – CuO. *Appl. Catal. B Environ.* **2020**, *265*, 118543. https://doi.org/10.1016/j.apcatb.2019.118543.

[17] Ebeling, K. M.; Bongartz, D.; Mürtz, S.; Palkovits, R.; Mitsos, A. Thermodynamic and Economic Potential of Glycerol Oxidation to Replace Oxygen Evolution in Water Electrolysis. *Ind. Eng. Chem. Res.* **2024**, *63* (18), 8250–8260. https://doi.org/10.1021/acs.iecr.3c03615.

[18] Anastas, P.; Eghbali, N. Green Chemistry: Principles and Practice. *Chem. Soc. Rev.* **2009**, *39* (1), 301–312. https://doi.org/10.1039/B918763B.

[19] He, Z.; Ning, X.; Yang, G.; Wang, H.; Cao, Y.; Peng, F.; Yu, H. Selective Oxidation of Glycerol over Supported Noble Metal Catalysts. *Catal. Today* **2021**, *365*, 162–171. https://doi.org/10.1016/j.cattod.2020.04.019.

[20] Demirel-Gülen, S.; Lucas, M.; Claus, P. Liquid Phase Oxidation of Glycerol over Carbon Supported Gold Catalysts. *Catal. Today* **2005**, *102–103*, 166–172. https://doi.org/10.1016/j.cattod.2005.02.033.

[21] Lin, Z.; Chu, H.; Shen, Y.; Wei, L.; Liu, H.; Li, Y. Rational Preparation of Faceted Platinum Nanocrystals Supported on Carbon Nanotubes with Remarkably Enhanced Catalytic Performance. *Chem. Commun.* **2009**, No. 46, 7167–7169. https://doi.org/10.1039/B917235A.

[22] Painter, R. M.; Pearson, D. M.; Waymouth, R. M. Selective Catalytic Oxidation of Glycerol to Dihydroxyacetone. *Angew. Chem.* **2010**, *122* (49), 9646–9649. https://doi.org/10.1002/ange.201004063.

[23] Ide, M. S.; Falcone, D. D.; Davis, R. J. On the Deactivation of Supported Platinum Catalysts for Selective Oxidation of Alcohols. *J. Catal.* **2014**, *311*, 295–305. https://doi.org/10.1016/j.jcat.2013.12.002.

[24] Besson, M.; Gallezot, P. Selective Oxidation of Alcohols and Aldehydes on Metal Catalysts. *Catal. Today* **2000**, *57* (1), 127–141. https://doi.org/10.1016/S0920-5861(99)00315-6.

[25] Prati, L.; Rossi, M. Gold on Carbon as a New Catalyst for Selective Liquid Phase Oxidation of Diols. *J. Catal.* **1998**, *176* (2), 552–560. https://doi.org/10.1006/jcat.1998.2078.

[26] Villa, A.; Dimitratos, N.; Chan-Thaw, C. E.; Hammond, C.; Prati, L.; Hutchings, G. J. Glycerol Oxidation Using Gold-Containing Catalysts. *Acc. Chem. Res.* **2015**, *48* (5), 1403–1412. https://doi.org/10.1021/ar500426g.

[27] Malankowska, A.; Borowska, E.; Martins, R. C.; Gmurek, M. Editorial Catalysts: Special Issue on Recent Advances in TiO2 Photocatalysts. *Catalysts* **2021**, *11* (7), 790. https://doi.org/10.3390/catal11070790.

[28] Sanzone, G.; Zimbone, M.; Cacciato, G.; Ruffino, F.; Carles, R.; Privitera, V.; Grimaldi, M. G. Ag/TiO2 Nanocomposite for Visible Light-Driven Photocatalysis. *Superlattices Microstruct.* **2018**, *123*, 394–402. https://doi.org/10.1016/j.spmi.2018.09.028.

[29] Liu, Y.; Zhang, B.; Yan, D.; Xiang, X. Recent Advances in the Selective Oxidation of Glycerol to Value-Added Chemicals via Photocatalysis/Photoelectrocatalysis. *Green Chem.* **2024**, *26* (5), 2505–2524. https://doi.org/10.1039/D3GC03554A.

[30] Liu, M.; Liu, H.; Li, N.; Zhang, C.; Zhang, J.; Wang, F. Selective Oxidation of Glycerol into Formic Acid by Photogenerated Holes and Superoxide Radicals. *ChemSusChem* **2022**, *15* (19), e202201068. https://doi.org/10.1002/cssc.202201068.

[31] Augugliaro, V.; El Nazer, H. A. H.; Loddo, V.; Mele, A.; Palmisano, G.; Palmisano, L.; Yurdakal, S. Partial Photocatalytic Oxidation of Glycerol in TiO2 Water Suspensions. *Catal. Today* **2010**, *151* (1), 21–28. https://doi.org/10.1016/j.cattod.2010.01.022.

[32] Dong, H.; Zeng, G.; Tang, L.; Fan, C.; Zhang, C.; He, X.; He, Y. An Overview on Limitations of TiO2-Based Particles for Photocatalytic Degradation of Organic Pollutants and the Corresponding Countermeasures. *Water Res.* **2015**, *79*, 128–146. https://doi.org/10.1016/j.watres.2015.04.038.

[33] Daghrir, R.; Drogui, P.; Robert, D. Modified TiO2 For Environmental Photocatalytic Applications: A Review. *Ind. Eng. Chem. Res.* **2013**, *52* (10), 3581–3599. https://doi.org/10.1021/ie303468t.

[34] Rojas, N.; Hincapié-Triviño, G.; Velasquez, M. Photocatalytic Oxidation of Glycerol Using x/TiO2 (with X= Cu, Ag, and Cu-Ag) to Dihydroxyacetone and Other Value-Added Products. *Mol. Catal.* **2024**, *566*, 114390. https://doi.org/10.1016/j.mcat.2024.114390.

[35] Rajamohan, S.; Kumaravel, V.; Muthuramalingam, R.; Ayyadurai, S.; Abdel-Wahab, A.; Kwak, B. S.; Kang, M.; Sreekantan, S. Fe3O4–Ag2WO4: Facile Synthesis, Characterization and Visible Light Assisted Photocatalytic Activity. *New J. Chem.* **2017**, *41* (20), 11722–11730. https://doi.org/10.1039/C7NJ03004E.

[36] Ismael, M. Ferrites as Solar Photocatalytic Materials and Their Activities in Solar Energy Conversion and Environmental Protection: A Review. *Sol. Energy Mater. Sol. Cells* **2021**, *219*, 110786. https://doi.org/10.1016/j.solmat.2020.110786.

[37] Pignatello, J. J.; Oliveros, E.; MacKay, A. Advanced Oxidation Processes for Organic Contaminant Destruction Based on the Fenton Reaction and Related Chemistry. *Crit. Rev. Environ. Sci. Technol.* **2006**, *36* (1), 1–84. https://doi.org/10.1080/10643380500326564.

[38] Munoz, M.; de Pedro, Z. M.; Casas, J. A.; Rodriguez, J. J. Preparation of Magnetite-Based Catalysts and Their Application in Heterogeneous Fenton Oxidation – A Review. *Appl. Catal. B Environ.* **2015**, *176–177*, 249–265. https://doi.org/10.1016/j.apcatb.2015.04.003.

[39] Wardman, P.; Candeias, L. P. Fenton Chemistry: An Introduction. *Radiat. Res.* **1996**, *145* (5), 523–531. https://doi.org/10.2307/3579270.

[40] Alfredo Reyes Villegas, V.; Isaías De León Ramírez, J.; Hernandez Guevara, E.; Perez Sicairos, S.; Angelica Hurtado Ayala, L.; Landeros Sanchez, B. Synthesis and Characterization of Magnetite Nanoparticles for Photocatalysis of Nitrobenzene. *J. Saudi Chem. Soc.* **2020**, *24* (2), 223–235. https://doi.org/10.1016/j.jscs.2019.12.004.

[41] Zhou, X.; Liu, G.; Yu, J.; Fan, W. Surface Plasmon Resonance-Mediated Photocatalysis by Noble Metal-Based Composites under Visible Light. *J. Mater. Chem.* **2012**, *22* (40), 21337–21354. https://doi.org/10.1039/C2JM31902K.

[42] Mishra, P.; Patnaik, S.; Parida, K. An Overview of Recent Progress on Noble Metal Modified Magnetic Fe3O4 for Photocatalytic Pollutant Degradation and H2 Evolution. *Catal. Sci. Technol.* **2019**, *9* (4), 916–941. https://doi.org/10.1039/C8CY02462F.

[43] Tahmasebi, E.; Yamini, Y. Facile Synthesis of New Nano Sorbent for Magnetic Solid-Phase Extraction by Self Assembling of Bis-(2,4,4-Trimethyl Pentyl)-Dithiophosphinic Acid on

Fe3O4@Ag Core@shell Nanoparticles: Characterization and Application. *Anal. Chim. Acta* **2012**, *756*, 13–22. https://doi.org/10.1016/j.aca.2012.10.040.

[44] Rahnama, S.; Shariati, S.; Divsar, F. Selective Aptamer Conjugation to Silver-Coated Magnetite Nanoparticles for Magnetic Solid-Phase Extraction of Trace Amounts of Pb 2+ Ions. *RSC Adv.* **2021**, *11* (9), 4971–4982. https://doi.org/10.1039/D1RA00006C.

[45] Norouz Dizaji, A.; Yilmaz, M.; Piskin, E. Silver or Gold Deposition onto Magnetite Nanoparticles by Using Plant Extracts as Reducing and Stabilizing Agents. *Artif. Cells Nanomedicine Biotechnol.* **2016**, *44* (4), 1109–1115. https://doi.org/10.3109/21691401.2015.1019672.

[46] Varghese Alex, K.; Tamil Pavai, P.; Rugmini, R.; Shiva Prasad, M.; Kamakshi, K.; Sekhar, K. C. Green Synthesized Ag Nanoparticles for Bio-Sensing and Photocatalytic Applications. *ACS Omega* **2020**, *5* (22), 13123–13129. https://doi.org/10.1021/acsomega.0c01136.

[47] Mavaei, M.; Chahardoli, A.; Shokoohinia, Y.; Khoshroo, A.; Fattahi, A. One-Step Synthesized Silver Nanoparticles Using Isoimperatorin: Evaluation of Photocatalytic, and Electrochemical Activities. *Sci. Rep.* **2020**, *10* (1), 1762. https://doi.org/10.1038/s41598-020-58697-x.

[48] Liu, S.; Yu, B.; Wang, S.; Shen, Y.; Cong, H. Preparation, Surface Functionalization and Application of Fe3O4 Magnetic Nanoparticles. *Adv. Colloid Interface Sci.* **2020**, *281*, 102165. https://doi.org/10.1016/j.cis.2020.102165.

[49] Flores-López, Z. D.; Solís-Díaz, A. B.; Cervantes-Aviles, P. A.; Thangarasu, P.; Kumar, D.; Kaur, H.; Singh, J.; Lokande, P.; Huerta-Aguilar, C. A.; Mubarak, N. M. Insight Mechanism of Magnetic Activated Catalyst Derived from Recycled Steel Residue for Black Liquor Degradation. *Sci. Rep.* **2024**, *14* (1), 19057. https://doi.org/10.1038/s41598-024-70072-8.

[50] Makuła, P.; Pacia, M.; Macyk, W. How To Correctly Determine the Band Gap Energy of Modified Semiconductor Photocatalysts Based on UV–Vis Spectra. *J. Phys. Chem. Lett.* **2018**, *9* (23), 6814–6817. https://doi.org/10.1021/acs.jpclett.8b02892.

[51] *SAE 1018 Steel – Chemical Composition, Equivalent Material, Properties and Uses*. https://www.amardeepsteel.com/blog/sae-1018-steel-composition-properties.html (accessed 2024-12-19).

[52] *AISI 1018 Carbon Steel (UNS G10180)*. AZoM. https://www.azom.com/article.aspx?ArticleID=9138 (accessed 2024-12-19).

[53] Yeap, S. P.; Lim, J.; Ooi, B. S.; Ahmad, A. L. Agglomeration, Colloidal Stability, and Magnetic Separation of Magnetic Nanoparticles: Collective Influences on Environmental Engineering Applications. *J. Nanoparticle Res.* **2017**, *19* (11), 368. https://doi.org/10.1007/s11051-017-4065-6.

[54] Sastry, M.; Mayya, K. S.; Bandyopadhyay, K. pH Dependent Changes in the Optical Properties of Carboxylic Acid Derivatized Silver Colloidal Particles. *Colloids Surf. Physicochem. Eng. Asp.* **1997**, *127* (1), 221–228. https://doi.org/10.1016/S0927-7757(97)00087-3.

[55] Marcus, R. A. Electron Transfer Reactions in Chemistry: Theory and Experiment (Nobel Lecture). *Angew. Chem. Int. Ed. Engl.* **1993**, *32* (8), 1111–1121. https://doi.org/10.1002/anie.199311113.

[56] Rodrigues, T. S.; Zhao, M.; Yang, T.-H.; Gilroy, K. D.; da Silva, A. G. M.; Camargo, P. H. C.; Xia, Y. Synthesis of Colloidal Metal Nanocrystals: A Comprehensive Review on the

Reductants. *Chem. – Eur. J.* **2018**, *24* (64), 16944–16963. https://doi.org/10.1002/chem.201802194.

[57] Kozlov, S. M.; Viñes, F.; Görling, A. On the Interaction of Polycyclic Aromatic Compounds with Graphene. *Carbon* **2012**, *50* (7), 2482–2492. https://doi.org/10.1016/j.carbon.2012.01.070.

[58] Radoń, A.; Drygała, A.; Hawełek, Ł.; Łukowiec, D. Structure and Optical Properties of Fe3O4 Nanoparticles Synthesized by Co-Precipitation Method with Different Organic Modifiers. *Mater. Charact.* **2017**, *131*, 148–156. https://doi.org/10.1016/j.matchar.2017.06.034.

[59] Farnetti, E.; Crotti, C. Selective Oxidation of Glycerol to Formic Acid Catalyzed by Iron Salts. *Catal. Commun.* **2016**, *84*, 1–4. https://doi.org/10.1016/j.catcom.2016.05.014.

[60] Han, X.; Sheng, H.; Yu, C.; Walker, T. W.; Huber, G. W.; Qiu, J.; Jin, S. Electrocatalytic Oxidation of Glycerol to Formic Acid by CuCo2O4 Spinel Oxide Nanostructure Catalysts. *ACS Catal.* **2020**, *10* (12), 6741–6752. https://doi.org/10.1021/acscatal.0c01498.

[61] Zhang, J.; Xiao, S.; Chen, R.; Chen, F. Promotional Effect of Short-Chain Saturated Alcohols on Fe3O4-Catalyzed Decomposition of H2O2 and Its Application in Selective Oxidation of Benzyl Alcohol. *J. Chem. Technol. Biotechnol.* **2019**, *94* (5), 1613–1621. https://doi.org/10.1002/jctb.5929.

[62] Ballinger, P.; Long, F. A. Acid Ionization Constants of Alcohols. II. Acidities of Some Substituted Methanols and Related Compounds1,2. *J. Am. Chem. Soc.* **1960**, *82* (4), 795–798. https://doi.org/10.1021/ja01489a008.

# Chapter 4. Conclusions

## 4.1. Trace $SO_2$ capture

Sulfur dioxide emissions remain a challenge despite the successful implementation of flue gas desulfurizers. Adsorption is proposed to capture the leftover $SO_2$ as even low concentrations in a gaseous stream can prevent its valorisation. This was achieved by depositing $Fe_3O_4$ nanoparticles on two types of cellulose support: nanocrystalline and microcrystalline cellulose. The $Fe_3O_4$ nanoparticles were synthesized using green tea as a reducing agent. TGA was used to quantify the iron deposition on the cellulose support. SEM-EDS showed the presence of iron clusters when an excess of green tea was used or when no reducing agent was used. It was determined by XRD that when no reducing agent was used the chemical speciation of the iron was FeO(OH), whereas SAED showed that when green tea was used $Fe_3O_4$ nanoparticles were obtained. STEM imaging with EDS mapping showed that the deposition process was more efficient on the MCC than the NCC.

The adsorbents were tested in breakthrough experiments at room temperature with a flowrate of 10 mL/min of 25 ppm $SO_2$ in argon. Although this represents an ideal system, it was selected to fully control and thoroughly understand the impact of the adsorbents' synthesis conditions on their affinity for $SO_2$. Pristine NCC and MCC showed minimal adsorption, and no significant increase was observed when $Fe_3O_4$ nanoparticles were deposited on NCC. On the contrary, a drastic increase in adsorption capacity was observed when $Fe_3O_4$ nanoparticles were deposited on MCC by using a sub stoichiometric amount of green tea. Indeed, the adsorption capacity increased from $3.8\times10^{-4}$ $mg_{SO_2}/g_{adsorbent}$ for pristine MCC to 0.087 $mg_{SO_2}/g_{adsorbent}$ for the adsorbent containing 0.32 wt% of iron. The deposition process in synthesizing the adsorbents proved to be long as a deposition time of 24 hours was insufficient to improve the adsorption and 72 hours was the optimum. The iron content in the adsorbent was directly related to the adsorbent's affinity for $SO_2$. As such, the adsorption capacities increased from 0.0174 $mg_{SO_2}/g_{adsorbent}$ to 0.3822 $mg_{SO_2}/g_{adsorbent}$ when the iron content increased from 0.16 wt% to 2.98 wt%. The amount of reducing agent used was also investigated as it dictated the chemical speciation of the iron. Indeed, when no reducing agent was used FeO(OH) was recovered in the adsorbent, when 0.04 equivalents were used $Fe_3O_4$ nanoparticles were deposited and when 1 or 2 equivalents were used agglomerated $Fe_3O_4$ was deposited. This directly impacted the adsorption capacities with the $Fe_3O_4$ nanoparticles showing

the highest adsorption at 24.6 $mg_{SO_2}/g_{Fe}$ compared to 12.0 $mg_{SO_2}/g_{Fe}$ for FeO(OH) and 2.7 $mg_{SO_2}/g_{Fe}$ for agglomerated $Fe_3O_4$.

## 4.2. Glycerol revalorisation

The increase in biodiesel production as an alternative to traditional fossil fuels has resulted in an overproduction of glycerol. This byproduct can be revalorised into valuable chemicals, such as dihydroxyacetone, from a partial oxidation. $Fe_3O_4$ nanoparticles were tested as a catalyst for this application due to their affordability, non-toxicity and potential to be used as a photocatalyst. $Fe_3O_4$ nanoparticles were produced from a coprecipitation reaction and by a steel revalorisation technique. Both methods yielded $Fe_3O_4$ as confirmed by XRD, while TEM imaging did show more agglomeration in the $Fe_3O_4$ obtained from the revalorisation method. Both supports could be doped with Ag nanoparticles using $NaBH_4$ and green tea as reducing agent. Band gap measurements using UV-Vis spectroscopy and the Tauc method confirmed a decrease in band gaps for the doped catalysts. The glycerol oxidation reaction was performed using a traditional Fenton system and a Fenton-like system in which the catalyst was $Fe_3O_4$ and its derivatives. By using $Fe_3O_4$ based catalysts, the selectivity of the reaction completely changed, and DHA was formed preferentially over FA contrary to the Fenton system. The ratio of $H_2O_2$/glycerol of 2.8 led to the highest conversion of glycerol using $Fe_3O_4$. When revalorisation $Fe_3O_4$ was used, the glycerol conversion was 19% which was the highest conversion when using a $Fe_3O_4$ based catalyst. A DHA selectivity as high as 93% was observed for the reaction catalysed by the Ag doped $Fe_3O_4$ using $NaBH_4$ as the reducing agent. A high DHA selectivity is desired as this compound has the highest economical value. Preliminary experiments in a photocatalytic system also showed that the Ag doped catalyst was active when exposed to sufficient light even without $H_2O_2$ in the reaction media.

## 4.3. Future work

$Fe_3O_4$ nanoparticles deposited on MCC have shown some good adsorption capacity for trace $SO_2$ capture in the model gaseous stream containing 25 ppm $SO_2$ in argon. Future work for this application should focus on performing other chemical modifications such as an oxidation of the cellulose support to evaluate if this increases it adsorption capacity. A more representative simulation of flue gas should also be tested for the adsorption as the adsorbents synthesized herein

show good affinity for $SO_2$ in the model system. Indeed, $SO_2$ with argon was used in this research, but this would not be the case in an end application where the adsorbent would be placed after flue gas desulfurizers. The adsorbent should be tested with a gaseous stream also containing $CO_2$, $O_2$ and some degree of $H_2O$ to better represent its final application and determine whether $SO_2$ adsorption decreases, is maintained or improves under these conditions, Performing XPS analysis would also provide valuable information on the oxidation state of the Fe and the S before and after the adsorption. This could help understand the adsorption mechanism and determine the degree of chemisorption.

As for the glycerol oxidation reaction, the initial future work should focus on increasing the glycerol conversion. This could be achieved by modifying other conditions in the Fenton-like system such as the temperature, the pH or decreasing even further the mass of catalyst used. A complementary analysis by HPLC of the Fenton-like reaction products would also support the conversion and selectivity measured by NMR. Of course, repeating the improved conditions by using revalorisation magnetite-based catalyst will need to be done. Finally, the transition towards a $H_2O_2$ free, photocatalytic system will need to be further investigated as this represents the optimal system to carry this reaction with the lowest environmental impact.

# Appendices

## Supplementary information for chapter 2

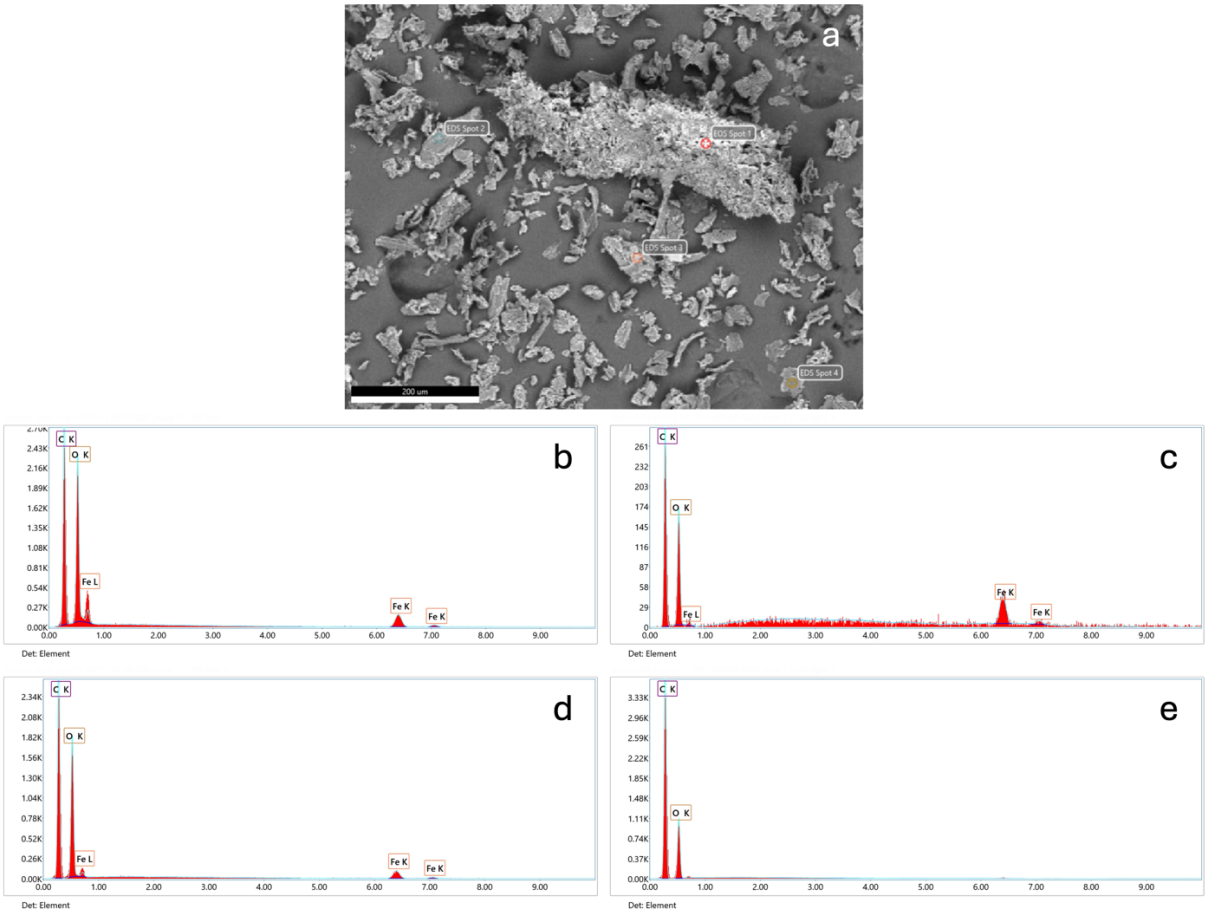


**Figure 4.1.** (a) SEM image of MCC modified with iron using no reducing agent, but with the same total volume as when using 2 equivalents and EDS spectra of (b) spot 1, (c) spot 2, (d) spot 3 and (e) spot 4 identified on the image.

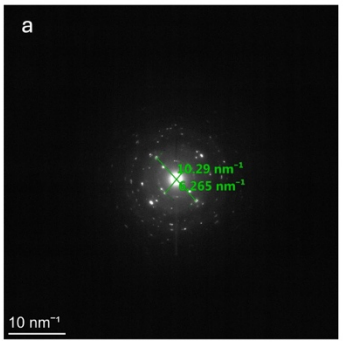


| Ring No. | Ring diameter ($nm^{-1}$) | Ring radius ($nm^{-1}$) | Calculate d-spacing (Å) | Theoretical d-spacing | hkl |
|---|---|---|---|---|---|
| 1 | 6.265 | 3.1325 | 3.192 | 2.97 | 220 |
| 2 | 10.29 | 5.145 | 1.944 | 2.10 | 400 |
| 3 | 12.05 | 6.025 | 1.66 | 1.62 | 511 |
| 4 | 15.86 | 7.93 | 1.261 | 1.27 | 622 |
| 5 | 18.92 | 9.46 | 1.057 | 1.05 | 800 |

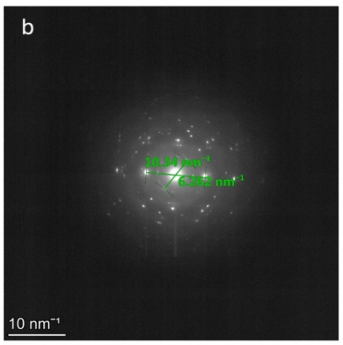


| Ring No. | Ring diameter ($nm^{-1}$) | Ring radius ($nm^{-1}$) | Calculate d-spacing (Å) | Theoretical d-spacing | hkl |
|---|---|---|---|---|---|
| 1 | 6.262 | 3.131 | 3.194 | 2.97 | 220 |
| 2 | 10.34 | 5.17 | 1.934 | 2.10 | 400 |
| 3 | 12.12 | 6.06 | 1.65 | 1.62 | 511 |
| 4 | 15.92 | 7.96 | 1.256 | 1,266 | 622 |
| 5 | 17.86 | 8.93 | 1.12 | 1.21 | 444 |
| 6 | 18.94 | 9.47 | 1.056 | 1.05 | 800 |
| 7 | 20.61 | 10.305 | 0.97 | 0.97 | 751 |

**Figure 4.2.**SAED images of $Fe_3O_4$ nanoparticles synthesized using green tea and their corresponding ring diameters compared to theoretical spacing of $Fe_3O_4$. Not all ring diameter measurements are presents on the images.

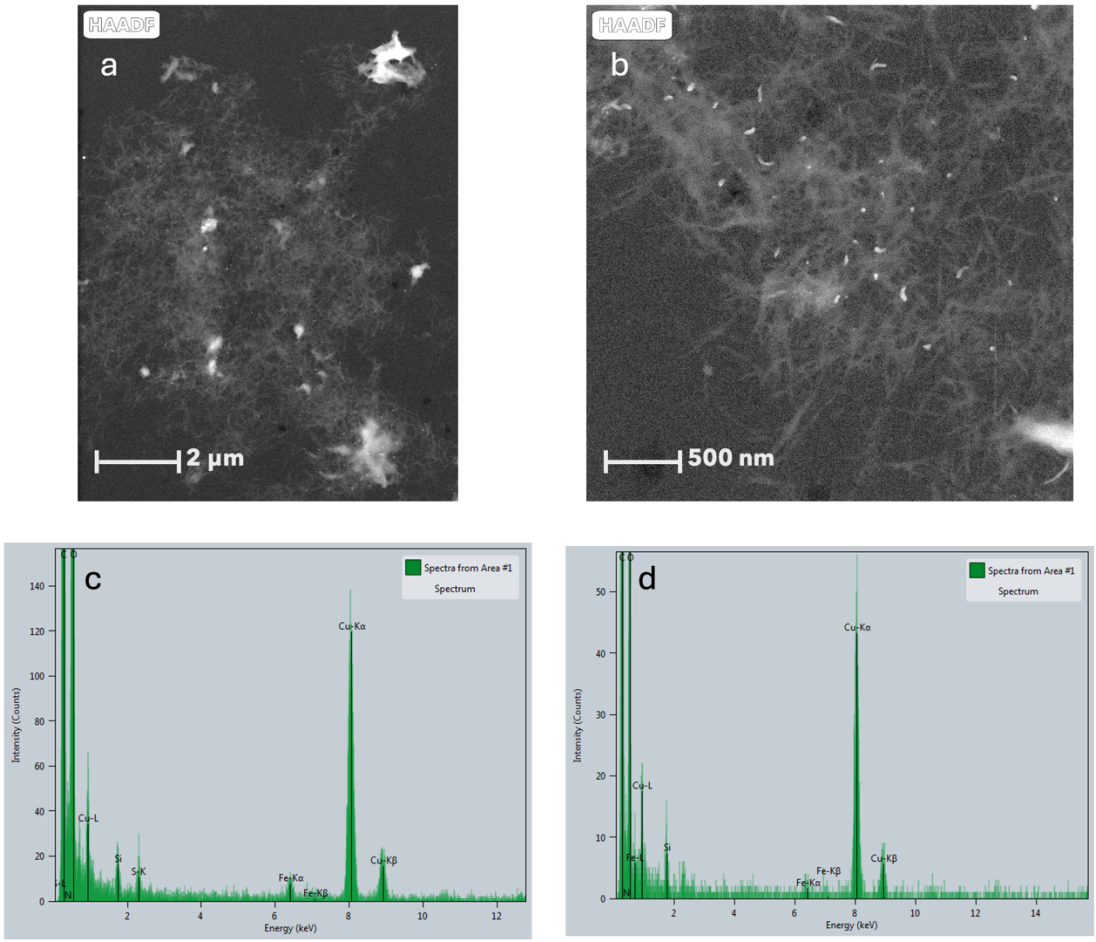


**Figure 4.3.** (a,b) HAADF images of NCC modified with iron-based nanoparticles and (c,d) localised EDS spectra performed on the particles appearing white on the images

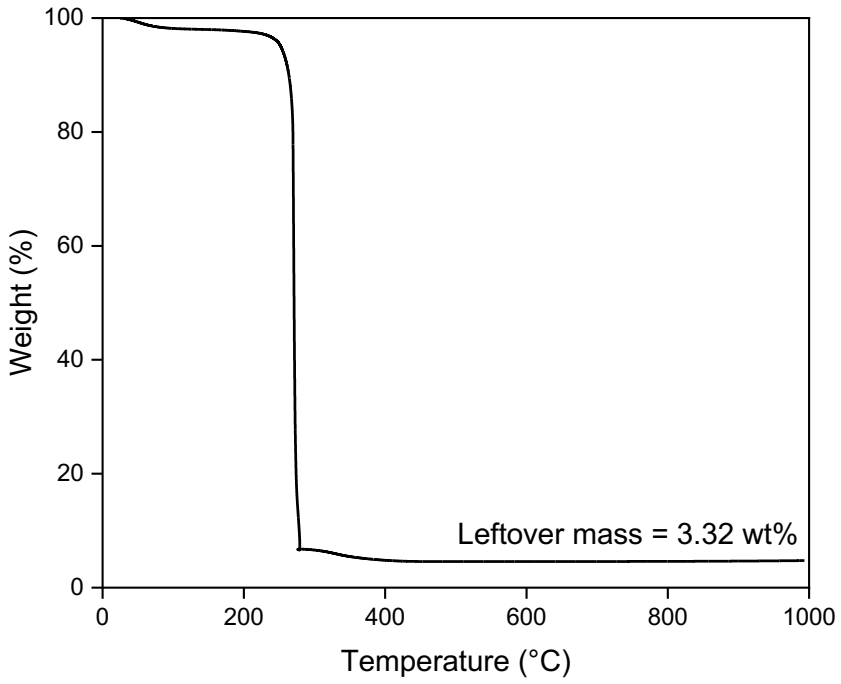


**Figure 4.4.** TGA degradation curve of MCC modified with iron using no reducing agent, but with the same total volume as when using 2 equivalents

# Supplementary information for chapter 3

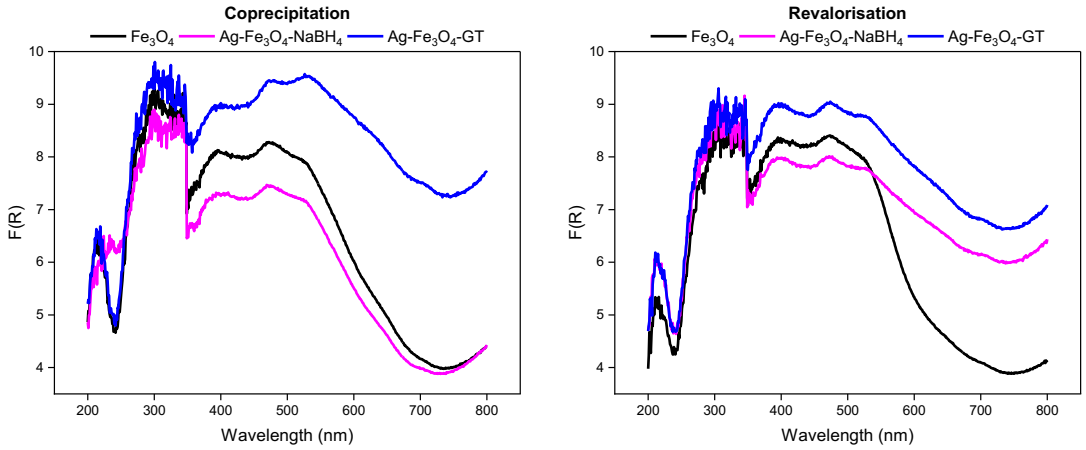


**Figure 4.5.** Diffuse reflectance spectroscopy of (a) coprecipitation $Fe_3O_4$ catalysts and (b) revalorisation catalysts

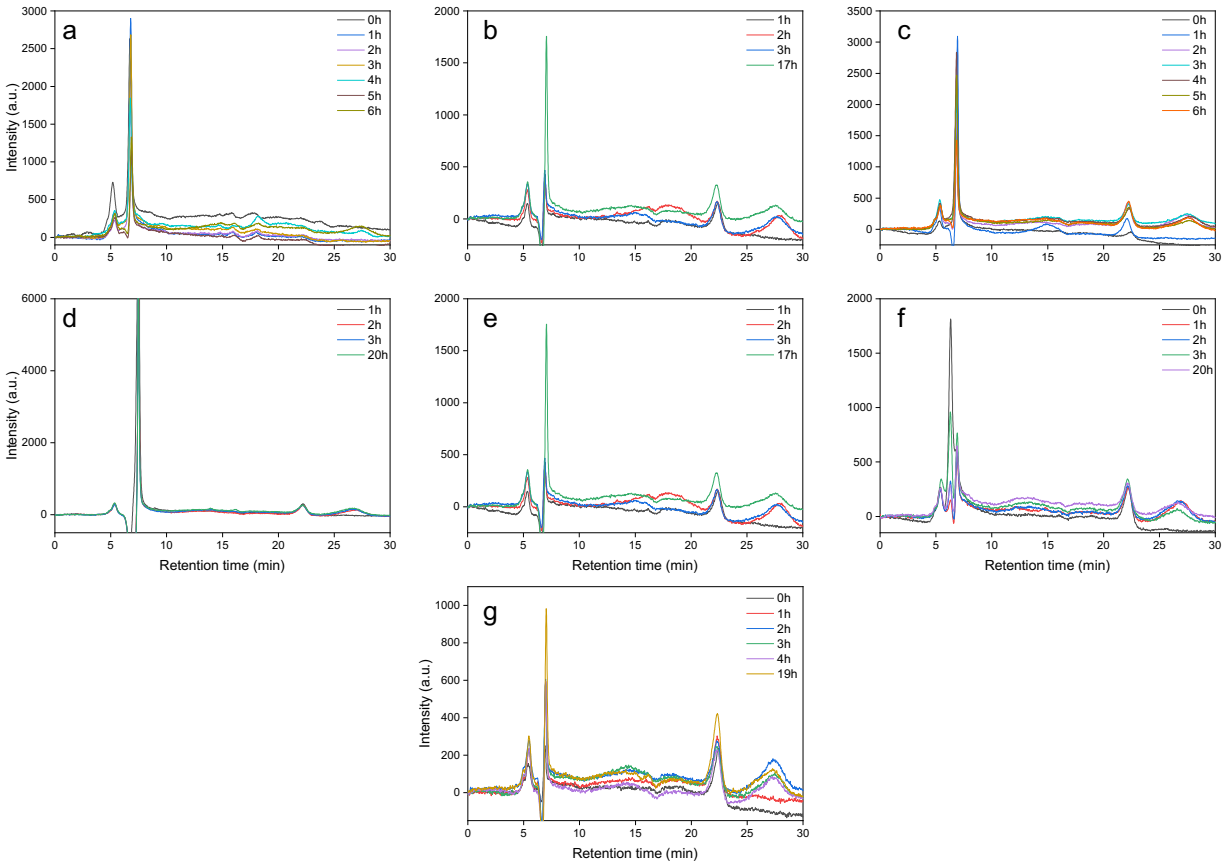


**Figure 4.6.** HPLC chromatograms of the photocatalytic oxidation of glycerol. Impact of the light intensity when (a) 500 lux, (b) 5000 lux and (c) 15 000 lux light sources are used. Effect of the pH when the reaction is carried with (d) pH = 2, (e) pH=6 and (f) pH=10. Effect of the temperature (g) when the reaction is carried out at 80°C